

Dipartimento di / Department of
Materials Science

Dottorato di Ricerca in / PhD program Materials Science and nanotechnology Ciclo /Cycle XXXVI

Scintillating nano-porous Metal-Organic Frameworks for radioactive gas detection

Cognome / Surname Orfano Nome / Name Matteo

Matricola / Registration number 782739

Tutore / Tutor: Prof. Angelo Monguzzi

Coordinatore / Coordinator: Prof. Francesco Cimbri Mattia Montalenti

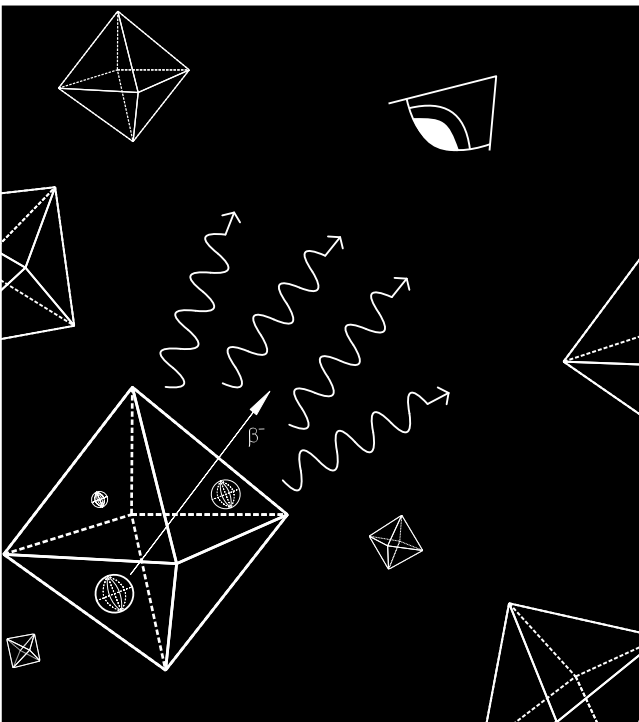
ANNO ACCADEMICO/ACADEMIC YEAR 2022/2023

SCINTILLATING NANO-POROUS METAL-ORGANIC FRAMEWORKS F O R RADIOACTIVE GAS DETECTION

PH.D. THESIS IN
MATERIALS SCIENCE AND NANOTECHNOLOGY



MATTEO ORFANO



This page was intentionally left blank.

This page was intentionally left blank.

— — P R E F A C E — —

This manuscript originates from my 3 years long Ph.D. research period at the Università degli Studi di Milano-Bicocca, in the Department of Materials Science, under the supervision of Prof. Angelo Monguzzi. The main project I was (and still am) involved in is called SPARTE (Scintillating Porous Architecture for RadioacTivE gas detection). SPARTE is a project funded by European Union's Horizon 2020 research and innovation programme. Its main goal is the implementation of radically new technology in the radioactive gas detection panorama introducing porous scintillators (such as Metal-Organic Frameworks or aerogels) to dramatically extend the gas-matter interaction for effective detection through scintillation. SPARTE also intends to introduce a new type of detector in this field, called micro-TDCR, which subsists in a triple coincidence detector that is extremely accurate when dealing with ultra-dilute gas concentrations. Efforts in these studies are devoted to replacing the current technology based on liquid scintillators. In fact, this kind of typically organic scintillators, while having a good response in detecting ionising radiation, present poor compatibility with different gas mixtures, making each sample single-use, generating enormous costs in waste management (organic and radioactive, after use) and with a high impact in terms of sustainability. Furthermore, current systems do not allow for the detection of radioactive gases on-site but only in the so-called post-sampling phase, unlike the aforementioned micro-TDCR. In particular, my research work is based on the study of the photoluminescence and scintillation properties of hafium- and zirconium-based Metal-Organic Frameworks (MOFs) as well as the conceiving of the materials. The following manuscript is divided in six chapters. The first one is an introduction to radioactivity, to ionizing radiation-matter interaction, to the basis of the scintillation phenomenon and a overview of different anthropogenic radioactive gases. The second chapter is a description of the SPARTE project in detail. Chapter 3 illustrates the actual state of the art in the field of radioactive gas detection systems and the analysis of the three most advanced system in Europe: the Swedish SAUNA, the SPALAX™ and the micro-TDCR. Chapter 4 and 5 represent my work during my research period. In particular, the first one is mainly dedicated to the optical and

scintillation properties of hafnium-based MOFs exploiting diphenyl anthracene (DPA) as fluorescent ligand and their capability of detecting various gas of interest like ^{85}Kr or ^{222}Rn . The second one is about a relatively new strategy for the optimization of MOFs light output by introducing the possibility of the occurrence of different energy transfer mechanisms by a controlled substitution of DPA ligands (which acts as energy acceptor) with a terphenyl donor dye. The benefits of this technique are two folded: the first one is the suppression of self-absorption that strongly increases the number of photons emitted upon excitation while the second benefit (strictly related to the first one) is a more precise matching of the quantum efficiency of common PMTs. It is worth noting that Chapter 5 represents a research line that is not completed yet while what is illustrated in Chapter 4 is in its advanced stage. The last chapter, Chapter 6, illustrates the conclusions of this 3-years work with some final remarks and future perspectives.

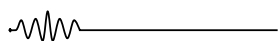
Milano, 31st October, 2023

Matteo Orfano

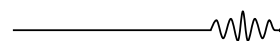


This project has received funding from the European Union's Horizon 2020 research and innovation programme under grant agreement No 896263





PEOPLE



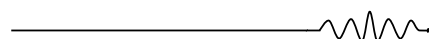
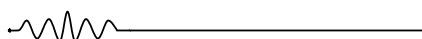
Everything presented in this text stems from many collaborations and interactions, learnings and mistakes. But above all, teachings. Firstly, I would like to thank Professor Angelo Monguzzi for sharing his knowledge with me and pushing me to develop my critical thinking in the scientific field, without placing (too many) limits on my imagination and creativity. Then I would like to thank Professor Angiolina Comotti and her research team. In particular, thanks to Dr. Jacopo Perego for the synthesis of the Metal-Organic Frameworks studied in this thesis and their structural characterisation. Thanks also to Dr. Charl Xavier Bezuidenhout for all the gas adsorption simulations and computations. Thanks to Dr. Silvia Bracco for the NMR analyses. I would also like to thank Professor Anna Vedda and her research group, especially Dr. Francesca Cova, essential for understanding the scintillation phenomenon studied in this writing. Thanks also to Dr. Irene Villa, who covered an essential role in this research. Furthermore, a heartfelt thanks goes to Professor Christophe Dujardin who, with his research group, welcomed me at the ILM institute in Lyon. Thanks a lot for having me there. Remaining in France, thanks also to Dr. Benoit Sabot for performing radioactive gas adsorption experiments in CEA, Paris-Saclay. In general, a great acknowledgement goes to every person in the SPARTE project that, at the end of its third year, is really reaching the possibility to propose a breakthrough solution in the radioactive gas detection field. I'm almost done. The biggest thanks therefore goes to all the people who accompanied me during this long period of my life and to the Fontaines D.C., Acid Arab, C'mon Tigre and Marco Castello for being the main background music during the writing.



This page was intentionally left blank.

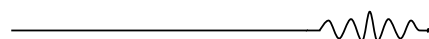
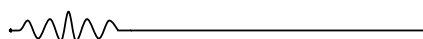


☀ Chapter 1: Introduction	1
⊗ 1.1 Ionizing radiation and its interaction with matter	1
1.1.1 Historical background	1
1.1.2 Radioactivity phenomenology	3
1.1.3 Types of ionizing radiation	7
1.1.4 Radiation-matter interaction	11
⊗ 1.2 Detection of ionizing radiation: scintillators	17
1.2.1 The physics of scintillation	20
⊗ 1.3 Radiation sources, hazards, and benefits	27
⊗ 1.4 Focus on radioactive gases	31
1.4.1 Gas of interest, hazards, and regulations	31
1.4.2 State of the art in β emitting gas detection and metrology	35
1.4.3 Thesis focus: Metal-Organic Frameworks as porous scintillators	37
⊗ 1.5 References	40
☀ Chapter 2: SPARTE project	44
⊗ 2.1 SPARTE project in detail	44
2.1.1 SPARTE consortium	47
2.1.2 Consortium goals	49
2.1.3 Work Packages (WPs)	50
☀ Chapter 3: Radioactive gas detection systems	53
⊗ 3.1 SAUNA	53
⊗ 3.2 SPALAX TM	57
⊗ 3.3 micro-TDCR	59
⊗ 3.4 References	64
☀ Chapter 4: Efficient radioactive gas detection by scintillating Metal-Organic Frameworks	66
⊗ 4.1 Synthesis and analysis of hafnium-based MOFs	69
4.1.1 9,10-bis(4-carboxyphenyl)anthracene ligand	69
4.1.2 Hf-DPA MOFs	71





☼ 4.2 Gas adsorption analysis	74
4.2.1 Isotherms analysis	75
4.2.2 Gas distribution inside Hf-DPA MOFs	76
☼ 4.3 Hf-DPA MOFs photoluminescence and scintillation properties	78
☼ 4.4 Radioactive gas detection by Hf-DPA MOFs	84
☼ 4.5 Methods	90
☼ 4.6 References	95
☼ Chapter 5: Hetero-ligand MOFs: a path to light output optimization	98
☼ 5.1 Synthesis and analysis of hetero-ligand zirconium-based MOFs	101
5.1.1 2',5'-dimethyl-[1,1':4',1''-Terphenyl]-4,4''-dicarboxylic acid	101
5.1.2 Zr-Tp-DPA MOFs	102
☼ 5.2 Gas adsorption analysis	105
5.2.1 Isotherms analysis	105
☼ 5.3 Zr-Tp-DPA photoluminescence and scintillation properties	106
☼ 5.4 Radioactive gas detection by Zr-Tp-DPA MOFs	114
☼ 5.5 Methods	117
☼ 5.6 References	122
☼ Chapter 6: CONCLUSIONS	123
☼ Appendix A: TDCR principle	127
☼ Appendix B: Hf-DPA MOFs size modulation	130



This page was intentionally left blank.



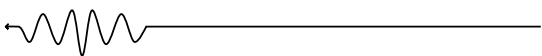
INTRODUCTION

1.1 Ionizing radiation and its interaction with matter

1.1.1 Historical background

November 8th, 1895 was a fruitful day for the German physicist Wilhelm Röntgen. While he was experimenting with Crookes tubes, an early electrical discharge tube by which cathode rays (i.e. stream of electrons) were discovered, he stumbled on a particular kind of radiation, so mysterious that he decided to call it X-rays¹. Indeed, these rays coming from the tube were able to light up the layer of barium platino-cyanide (a common phosphor at that age) deposited on a black piece of paper even with the paper facing the tube. This event made possible to discard any presence of UV photons interacting with the paper for their low penetration in that opaque medium. At that time, the phenomenon of light emission was known, and it was possible to observe it in different materials when heated up or subjected to high voltage or when interacting with light. Indeed, the best studied radiation was light, well described by Maxwell equations. It was clear that the interaction observed by Röntgen was of a totally new kind, a discover that revolutionized the scientific panorama opening new paths to better study and understand matter. The following years, the first radiographies of Röntgen and the word radioactivity were on every scientist's lips¹.

Indeed, the mathematician Henri Poincaré, physics enthusiast, formulated a hypothesis on Röntgen's observation making it public during a talk at the Académie des Sciences in Paris: he suggested that this X-ray emission could be a result of a general effect of fluorescence of the glass of the Crookes tube. Among the audience there was Henri Becquerel, professor at the Muséum d'Histoire Naturelle and expert in fluorescence. He directly set up an an experiment, placing a piece of potassium-uranyl sulfate on a



photographic plate wrapped in a thick piece of black paper and living it under the sunlight². “After developing the plate, one sees the outline of the phosphorescent substance in black. [...], the phosphorescent substance emits radiations able to traverse a paper which is opaque for light”, he wrote³. Next, for bad weather conditions, he left everything in a drawer that he only reopened days later, realising that the “shadow” spots were even more of a solid black. These first observations discarded the possibility of any interaction of the material with the sun and so the idea that the observed phenomenon was one of general fluorescence. After several experiments, Becquerel came up with the idea of “uranic rays”, an invisible phosphorescence able to traverse also aluminium sheets that seemed to be

endless. It was a mystery to understand where these uranium-related materials took that energy but the enthusiasm soon dropped, also related to the newly discovered Zeeman effect. The challenge to better understand these phenomena observed by Röntgen and Becquerel was then welcomed by the spouses Pierre Curie and Marie Skłodowska. Marie, in particular, started her doctorate thesis studying air electrical conductivity in presence of different materials, from Uranium compound to salts and minerals. She came to

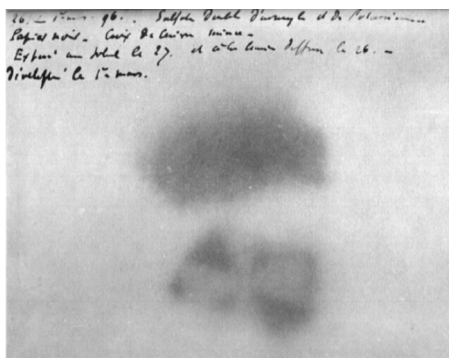


Fig. 1.1: photograph made by Henri Becquerel using uranium salts on a photographic plate.

an important conclusion: not only uranium but also thorium emits radiation⁴. “It is remarkable that the two most active elements, uranium and thorium, are those that have the highest atomic weight.”, writes Marie. It is now known that indeed heavy nuclei are unstable because short-range nuclear forces are not able to compensate the Coulomb repulsion between protons⁵. She then realized that some pitchblende compound, uranium ores and chalcocite were even more active than uranium, thus implying the presence of other elements with higher activity. It was in that time that polonium, radium and actinium were discovered, thanks also to the help of brilliant scientist Gustave Bémont, a chemist, and Eugène Demarçay, a spectroscopist⁶. If the list of elements displaying radioactive properties was expanding, little was known about the nature of this event. It was at that point, at the beginning of the twentieth century, that Becquerel, Marie and Pierre Curie, as well as Ernest Rutherford, joint knowledge and forces to better study these phenomena. Indeed, two components of these rays were



identified by Rutherford: one not so penetrating, stopped by a sheet of paper, and one so penetrating that only aluminium sheets could block it. Those two were both charged since air got ionized and their stream could be bent using a magnetic field. The first one, positively charged, was called α while the other one was called β , negatively charged. Then, Becquerel and Villard identified a third component that was not deflected by a magnetic field, an electromagnetic one, fact that was then proven by Rutherford and Andrad⁷. The so-called γ rays were discovered. Moreover, the analysis of the deviation of α particles permitted to Rutherford to identify their origin as ionized helium atoms. Still by Rutherford, together with Soddy, was the insight that the radioactive occurrence was strictly related to the transformation from one atom to another with different mechanisms. Nowadays, it is thanks to the works of all these scientists (and even more that here are not cited) that the subjects of radioactivity, particle physics and high energy physics are deeply understood, opening the way to the comprehension of matter and its building blocks.

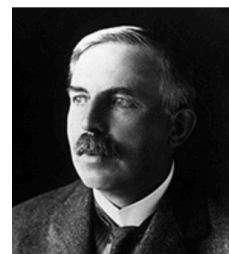
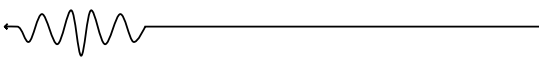


Fig. 1.2: Becquerel (top), Skłodowska (mid), and Rutherford (bottom).

1.1.2 Radioactivity phenomenology

Time passed from the first discovery of the “uranic rays” (later called Becquerel rays) and now we know that we are dealing with kinds of events that are called ionizing radiations, i.e. radiations that have enough energy to ionize matter. Moreover, thanks to different studies it has been possible to identify all the macro-components of an atom, starting with protons and electrons and then with neutrons. Indeed, the idea of Rutherford and Soddy about the connection with α , β and γ radiations and atom transformation was partly correct. It is now consolidated that the radioactive decay is the process by which an unstable nucleus loses energy reaching a new equilibrium condition. Shortly, this happens because of an unbalance between the number of protons and neutrons in the nucleus. The so-called “magic number” has to be reached. We know that there are two forces working here: the repulsion of protons and the strong nuclear force that creates a strong link between nucleons (protons and neutrons)⁸. These forces are short-range forces: when a nucleus become bigger for an excess of neutrons or protons it is more likely that it breaks up instead keeping everything together. Several



observations may be made regarding the relationship between the stability of a nucleus and its structure. Nuclei with even numbers of protons, neutrons, or both as well as nuclei with particular numbers of nucleons (2, 8, 20, 28, 50, 82, and 126) are more likely to be stable^{9,10}.

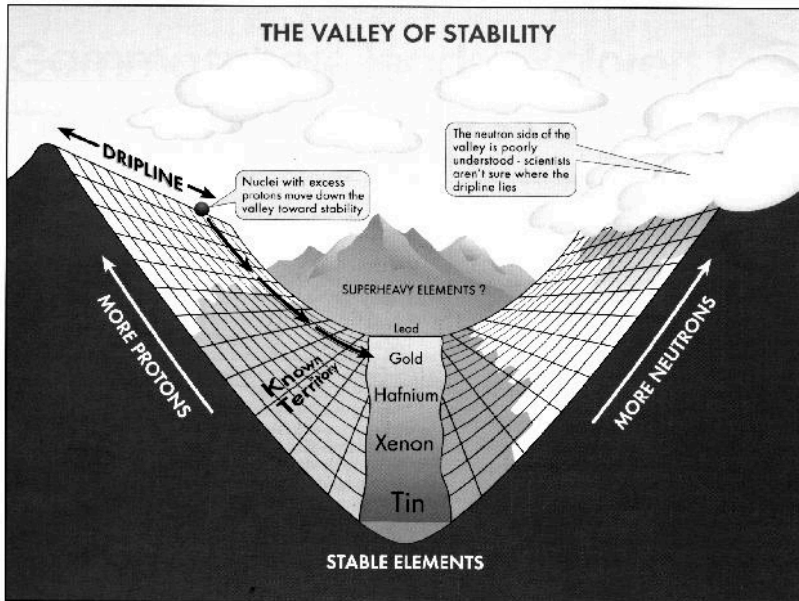


Fig. 1.3: valley of stability, reproduced from "Logos", Vol. 16, Numb. 2.

Nuclei that have magic numbers of both protons and neutrons are called "double magic" and are particularly stable. In this way it is possible to individuate a band of stability. Notably, if the lightest elements have an equal number of protons and neutrons, the heaviest ones occur to deviate from a linear behaviour, exceeding in nucleons. The nuclei that lie left or right of the band of stability are unstable and show radioactivity. They spontaneously decay into other nuclei that are either within or closer to the band of stability. These nuclear decay reactions change one unstable isotope (or radioisotope) into another more stable isotope. It is in this frame that the term "decay chain" takes place. These words refer to the series of radioactive decays that a nucleus must undergo to reach a stable isotope (more than 1 decay can be necessary to reach this condition). A parent isotope is one that undergoes decay to form a daughter isotope. An important figure of merit is the half-time $t_{1/2}$, i.e. the time that a given population of radioactive elements employs to undergo a radioactive decay. It could range from minutes to millions of years. Thus, radioactive decays follow a stochastic process. Given



a N number of atoms in the sample, it is possible to determine a decay constant λ :

$$\lambda = -\frac{(dN/dt)}{N}$$

that represents the probability of the decay of a given atom per unit time. By developing this equation it is possible to obtain an exponential decay law:

$$dN = -\lambda N dt$$

Thus:

$$\frac{dN}{N} = -\lambda dt$$

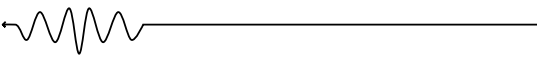
And by integration we obtain:

$$N(t) = N(0)e^{-\lambda t}$$

The decay constant λ should be now equal to the inverse of time (s^{-1}) so that:

$$\lambda = -\frac{1}{\tau}$$

where τ is called the mean lifetime and it is the average lifetime of atoms.



The link between t and $t_{1/2}$ could be obtained as:

$$N = \frac{N(0)}{2} = N(0)e^{-\frac{t_{1/2}}{\tau}}$$

$$2 = e^{\frac{t_{1/2}}{\tau}}$$

$$t_{1/2} = (\ln 2) \tau = 0.693 \tau$$

Unfortunately, this mathematics is of little use because N is a complicated quantity to estimate. More useful is surely the estimation of the number of decays that occur in a given amount of time. Thus, the activity A is given by¹¹:

$$A(t) = A(0)e^{-\lambda t}$$

which follows the same law as N . Literally, A is the number of disintegrations per second and, in the S.I. system the unit is (romantically) the becquerel (Bq), decays per second. Interestingly, when the production rate of a given

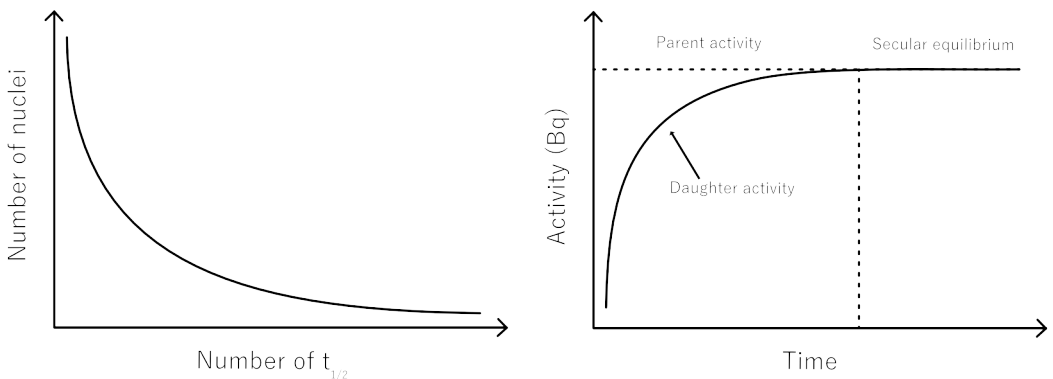


Fig. 1.4: number of nuclei remaining after subsequent radioactive decay of a generic element (left) and secular equilibrium conditions (right).



radioactive isotope is equal to its decay rate, the secular equilibrium is reached¹².

1.1.3 Types of ionizing radiation

Qualitatively speaking, the ways in which a generic radioactive isotope can radioactively decay are different. Below a list of them with their occurrence mechanisms is given.

X-rays

Discovered first by Röntgen, x-rays are ionizing radiation, high energy photons, typically emitted by the inner core electrons of an atom once they're excited and come back to the ground state. Typical x-rays energies can range from 140 eV (tens of nanometers in wavelength) to 120 keV (tens of picometers in wavelength)¹³. An usual way to obtain x-rays is to use a so-called X-ray tube, a vacuum tube at high voltage that accelerates electrons emitted by a hot cathode; these electrons hit a metal target (typically Tungsten) that emits x-rays from its inner shells. The radiation energy is strictly dependent on the type of metal house, given the different binding energies of every element. Tuning the emission energy means tuning the voltage but also, changing the metal. Other mechanisms by which X-ray can be emitted is by the so-called electron capture (see β particle below) or by Bremsstrahlung. In particular, in the latter, x-rays are generated by a charged particle that is decelerated by collisions with the nuclei and atomic particles¹⁴. In response, this event generates an x-ray continuous spectrum given by the loss of energy that the particle experiments when its trajectory is deflected by a nucleus or by collision with other species. The energy of the produced x-ray will be:

$$h\nu = E_i - E_f$$

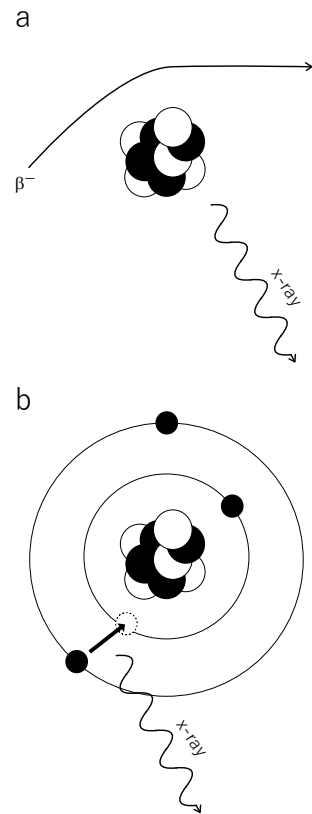


Fig. 1.5: illustration of the Bremsstrahlung effect and x-ray emission.

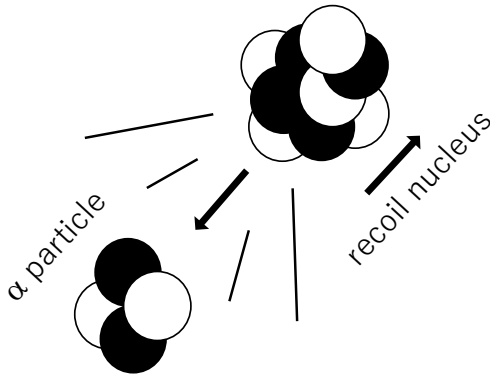
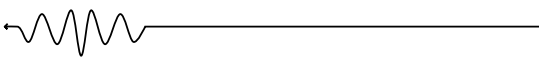
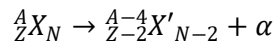


Fig. 1.6: illustration of an alpha particle emission.

α particles

α particles are generally emitted spontaneously, with an unbalance between the strong nuclear force and the Columbian repulsion. Thus, this kind of emission is typical of high Z atoms. α particles are positively charged particle, composed by four nucleons, two protons and two neutrons. They are considered as positively charged Helium atoms and they're sometimes indicated as He²⁺. They are lowly penetrating with a typical energy of 5 MeV. The spontaneous emission of an α particle can be described as follows⁸:

Helium atoms and they're sometimes indicated as He²⁺. They are lowly penetrating with a typical energy of 5 MeV. The spontaneous emission of an α particle can be described as follows⁸:



β particles

This kind of particles are maybe the first radioactive decay observed. Indeed,

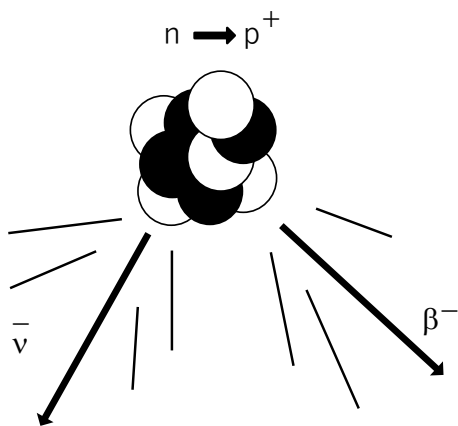


Fig. 1.7: illustration of an beta particle emission.

β decay is a process regarding the emission of an electron (or positron). The basic process involved in a production of a β particle is the conversion of a proton into a neutron or a neutron into a proton. In a nucleus, β decay changes both Z and N by one, so that A = Z + N remains constant⁸. Moreover, a third element is involved in this kind of process, that is a neutrino (or antineutrino). These are highly energetic particles, very difficult to

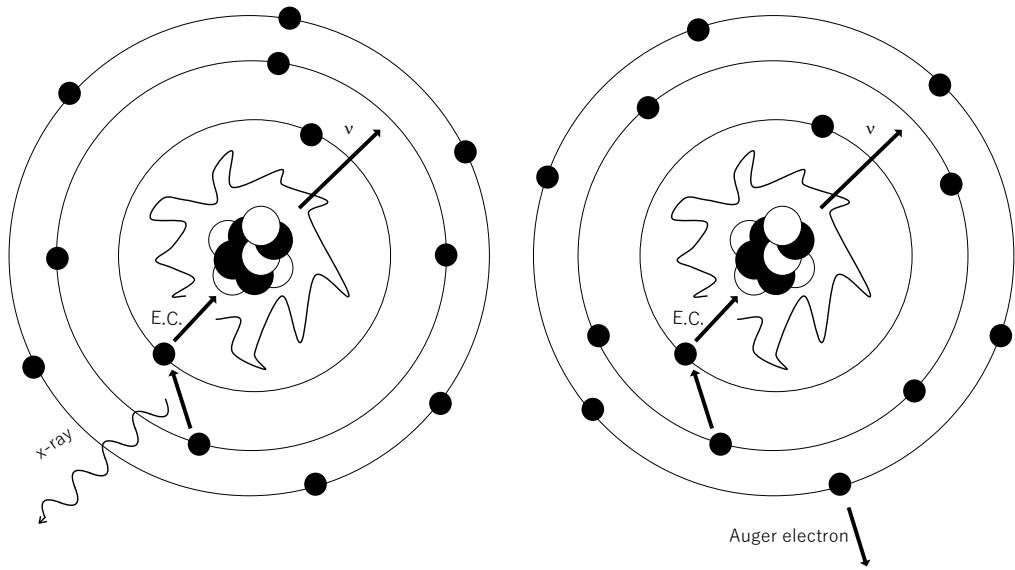


Fig. 1.8: sketch of the electron capture mechanism with x-ray production (left) and Auger electron production (right).

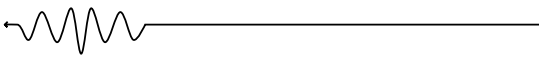
detect but that help maintaining the conservation of energy. The β decay can be thus described as follows:

$$n \rightarrow p + e^{-} + \bar{\nu}_e$$

$$p \rightarrow n + e^{+} + \nu_e$$

Where n is a neutron, p is a proton, e^{-} is an electron, e^{+} is a positron, ν_e is a neutrino and $\bar{\nu}_e$ is an antineutrino⁸. A third mechanism is probable, and it is called electron capture¹⁵. This is a process where an inner shell electron is attracted by a proton that converts itself in a neutron with the emission of a neutrino. By doing so, the hole left by the electron is than filled with another electron with a subsequent x-ray emission or the occurring of the Auger effect (electron expulsion from the shell).

$$p + e^{-} \rightarrow n + \nu_e$$



Thus, the decay chain is as follows:

$${}^A_Z X_N \rightarrow {}^A_{Z+1} X'_{N-1} + e^- + \bar{\nu}_e \quad (\beta^-)$$

$${}^A_Z X_N \rightarrow {}^A_{Z-1} X'_{N+1} + e^+ + \nu_e \quad (\beta^+)$$

$${}^A_Z X_N + e^- \rightarrow {}^A_{Z-1} X'_{N+1} + \nu_e \quad (E.C.)$$

γ rays

This kind of ionizing radiation is a form of electromagnetic wave emitted upon the decay of a nucleus. It differs from x-rays for the way in which it is generated and for the energy considered, since γ rays have usually higher energy than x-rays (they go from keV to MeV). Usually, after a parent nucleus decay, a daughter one is left in an excited state and the way it loses energy to get to its ground state is through the emission of γ rays¹⁴. To indicate the mechanism, here it is better working by examples using an atom of ${}^{60}\text{Co}$ as reference.

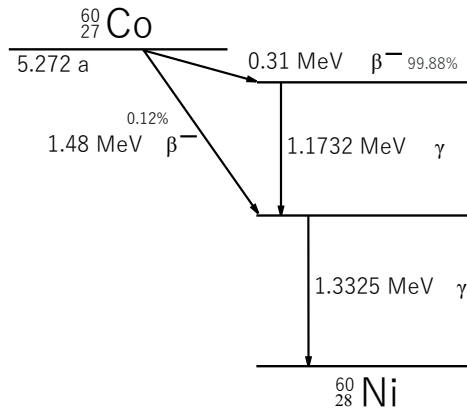


Fig. 1.9: ${}^{60}\text{Co}$ decay chain to ${}^{60}\text{Ni}$.

$${}^{60}_{27}\text{Co} \rightarrow {}^{60}_{28}\text{Ni}^* + e^- + \bar{\nu}_e + \gamma \quad (\beta^- + \gamma)$$

$${}^{60}_{28}\text{Ni}^* \rightarrow {}^{60}_{28}\text{Ni} + \gamma$$



1.1.4 Radiation-Matter interaction

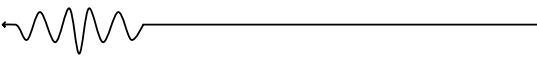
Typically, ionizing radiations can be grouped in two categories: directly and indirectly ionizing radiations. The first one is strictly related to the passage of charged particles in matter, while the second one is typical of photons.

Heavy charged particles interaction in matter

Heavy charged particles lose their kinetic energy through a process called collision loss process. The dominant interaction is electromagnetic that can lead to excitation or ionization processes in matter. These events are called of primary ionization since they strongly interact with matter. If the excited electrons are sufficiently energetic, they can also ionize matter starting a process of secondary ionization¹⁶. The energy deposited per unit path in the medium by this kind of interaction is usually less than the collision energy loss obtained by primary interactions, since electrons can travel far away from the ionization point and then be absorbed, or they can escape from the medium. The maximum energy that a charged particle in a single collision is $4Tm_e/m$, where T is the kinetic energy of the particle, m_e is the mass of the electron and m is the mass of the particle. At any given time, the particle velocity decreases due to various collisions and so it loses energy. The formula that better describes the energy loss in space for a charged particle is the Bethe-Block formula^{8,17}:

$$-\frac{dE}{dx} = \frac{4\pi r_e^2 m_e c^2 z^2}{\beta^2} NZ \left[\ln \frac{2m_e c^2 \gamma^2 \beta^2}{I} - \beta^2 \right]$$

where $\beta=v/c$, c is the speed of light, v is the incident particle velocity and z is the charge of the incident particle, $\gamma=1/(1-\beta^2)^{1/2}$, N and Z are the Avogadro number and the atomic number of the medium, r_e is the classical electron radius, e is the electronic charge and I is the ionization potential. In this way the stopping power is defined, and it is appreciable its dependency on Z : heavier atoms bring heavy charged particles to lose more energy reducing their path in matter. The Bethe-Block formula begins to fall apart at low particle energies where charge exchange between the particle and absorber becomes important. The positively charged particle will then tend to pick up electrons from the absorber, which effectively reduce its charge and



consequent linear energy loss. At the end of its track, the particle has accumulated Z electrons and becomes a neutral atom.

Light charged particles interaction in matter

This is the case of electrons travelling through matter, for example. The way in which they lose energy is via inelastic collisions against electrons of atoms and, sometimes, against nuclei. The energy loss can still be described by the Bethe-Block formula, with some adjustments due to the similar mass of the particles taken into account¹⁷:

$$-\frac{dE}{dx} = \frac{4\pi r_e^2 m_e c^2 z^2}{\beta^2} NZ \left[\ln \frac{2m_e c^2 \gamma^2 T \beta^2}{2I} - \ln 2 \left(\frac{2}{\gamma} - \frac{1}{\gamma^2} \right) + \frac{1}{\gamma^2} + \frac{1}{8} \left(1 - \frac{1}{\gamma} \right)^2 \right]$$

where the symbols have the same meaning of the formula above. The other way in which light charged particles can lose energy is via the Bremsstrahlung phenomenon that is, as said in 1.1.3, a radiative process that takes place when the trajectory of the particle is bended in correspondence of a nucleus of the medium. The energy loss is described as:

$$-\frac{dE}{dx} = 4r_e^2 Z^2 \alpha N E_0 \left[\ln \frac{2E_0}{m_e c^2} - \frac{1}{3} \right]$$

where $\alpha=1/137$ is the fine structure constant, and E_0 is the initial total energy of the electron. Being the probability of Bremsstrahlung inversely proportional to the mass of the particle, it can be negligible for heavy particles.

Photon interaction with matter

The lack of charge in radiation such as γ and x-rays makes necessary a new way to treat their interaction with matter. Indeed, this absence hinders their energy dissipation, in contrast with what we said about α and β particle, resulting in higher penetration depth in matter. Moreover, they can also be



absorbed. Above are described the main three ways in which indirect ionizing radiations lose their energy.

Photoelectric effect

A photon's energy may be entirely absorbed by an atom. In such a case, the full photon energy received is transferred to an atom's electron, which is then released and leads to the production of an ion pair. The energy of the expelled electron is therefore equal to the energy of the incoming photon less the electron's binding energy. The Einstein photoelectric equation explains this¹⁸:

$$E_e = h\nu - \Phi$$

where E_e is the energy of the expelled electron, $h\nu$ is the energy of the photon that struck the surface, and ϕ is the binding energy of the electron, which is the amount of energy needed to take the electron out of the atom. The expelled electron has the same properties as a β particle and, like β particles, causes ionization as it moves through matter. In this case, secondary ionization is the

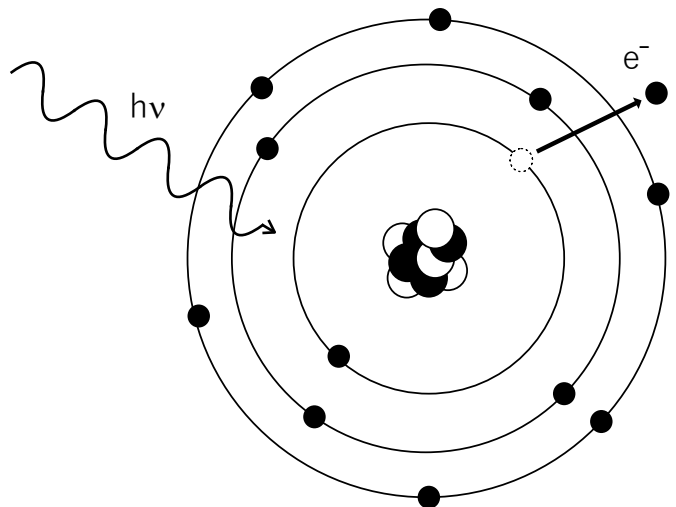
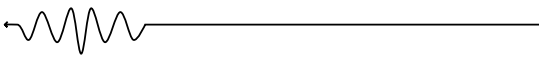


Fig. 1.10: illustration of the photoelectric effect.

process involved. Electrons from outer shells drop from their higher energy states to fill the void left when an electron from an inner atomic K or L shell is evicted. The atomic electrons release energy during these transitions which can be considered as soft (low-energy) x-rays. The characteristics of x-radiation and γ -radiation are the same. The difference between γ and x-rays is in where they come from. As was previously mentioned, atomic nuclei undergo energy state changes that give rise to γ radiation, whereas atomic electrons undergo energy state changes that give rise to x-radiation¹⁴. There



is not a unique way to describe the occurring probability of the photoelectric effect over all ranges of energies and atomic numbers of the absorber. A rough estimation can be pointed out as follows¹⁹:

$$\tau \cong \text{constant} \times \frac{Z^n}{E_\gamma^{3.5}}$$

Where n is a number between 4 and 5 that changes in the photon energy range and Z is the atomic number of the medium. It is depicted in fig. 1.11.



Fig. 1.11: depiction of the photoelectric cross section; the K, L and M edge indicates the energy at which the photoelectric probability is higher.

Compton effect

A second method exists by which a photon, such as an x-ray, γ ray, or other type of photon, transmits energy to an atomic electron. The photon, E_γ , in this interaction only transfers a little portion of its energy to the electron, which causes it to be deflected at an angle with energy E_γ , while the scattered electron is expelled at an angle Θ to the main photon's trajectory. The Compton effect and Compton scattering are two names for this interaction. As in the case of the photoelectric effect, an ion pair is created as a result of this interaction. The deflected photon, however, keeps moving through the material until it loses all of its kinetic energy through interaction with other

Introduction

electrons. The expelled electron, which has the same properties as a beta particle, loses energy due to secondary ionization caused by the mechanisms previously outlined¹⁴. It is possible to show that:

$$E'_\gamma = \frac{E_\gamma}{1 + \frac{E_\gamma}{m_0 c^2} (1 - \cos\theta)}$$

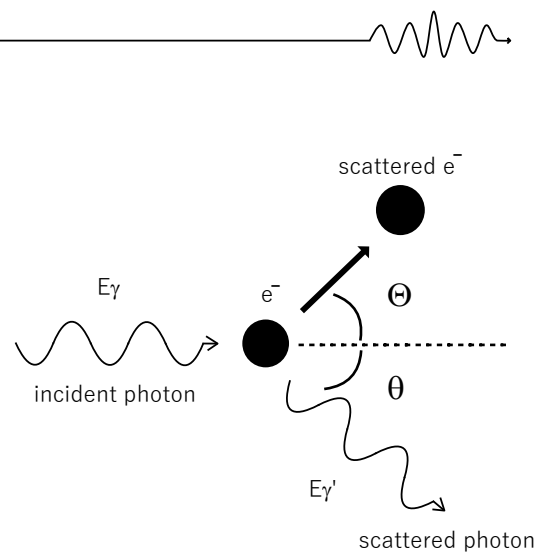


Fig. 1.12: illustration of the Compton effect.

The likelihood of Compton scattering per absorber atom is proportional to the number of electrons accessible as scattering targets, and hence grows linearly with Z. The Klein-Nishina formula for the differential scattering cross section $d\sigma/d\Omega$ predicts the angular distribution of scattered photons¹⁹:

$$\frac{d\sigma}{d\Omega} = Zr_0^2 \left(\frac{1}{1 + \alpha(1 - \cos\theta)} \right)^2 \left(\frac{1 + \cos^2\theta}{2} \right) \left(1 + \frac{\alpha^2(1 - \cos\theta)^2}{(1 + \cos^2\theta)[1 + \alpha(1 - \cos\theta)]} \right)$$

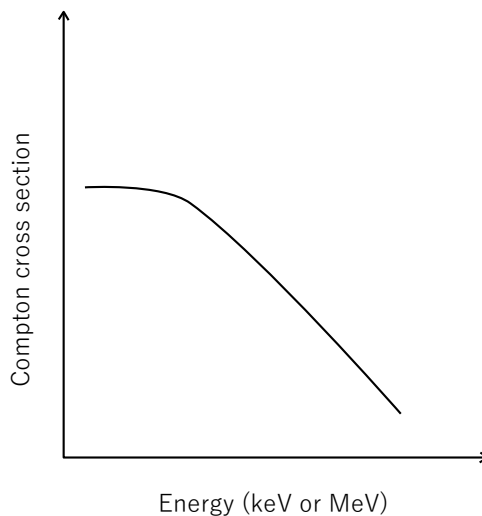


Fig. 1.13: Compton scattering cross section.

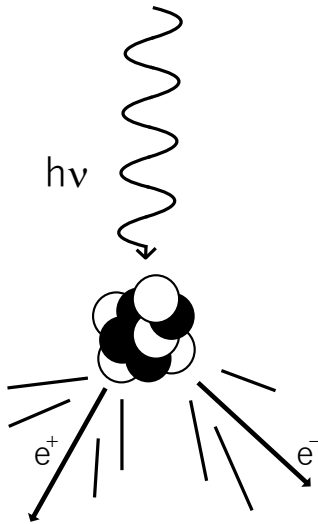
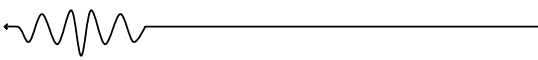


Fig. 1.14: pair production illustration.

Pair production

Gamma radiation interactions with matter entail the transmission of gamma energy, in whole or in part, to atomic electrons of the irradiated material. Another mode of gamma-energy dissipation in matter is pair generation, which results in the creation of atomic particles (i.e. electrons) from the gamma energy. A negatron and a positron are created when an individual gamma-ray photon interacts with the coulombic field of a nucleus. As a result, this phenomenon involves the formation of mass from energy. An electron requires a specific quantum of energy from a gamma-ray photon, which may be computed using Einstein's equation for mass and energy equivalence:

$$E = mc^2$$

where E is energy, m the electron rest mass, and c the speed of light in vacuum. The least energy required to create an electron (negatron) is 0.511 MeV. A gamma ray of 0.511 MeV energy, on the other hand, cannot produce a negatron without also producing its antiparticle, the positron of equal mass and opposite charge. The γ -ray photon energy required to produce the negatron-positron pair is

$$E_{pair} = m_{e^-}c^2 + m_{e^+}c^2 = 2 * 0.511 \text{ MeV} = 1.02 \text{ MeV}$$

Where m_{e^-} and m_{e^+} are the negatron and positron rest masses, respectively. Thus, γ radiation absorption by materials more than 1.02 MeV may result in pair creation^{14,19}. There is not an accurate description of the interaction cross section in case of pair production, but it can be estimated as proportional to the square of the atomic number Z of the material¹⁹. Fig. 1.15 shows the relative importance of the three processes discussed above for different absorber materials and photon energy. As a function of absorber atomic

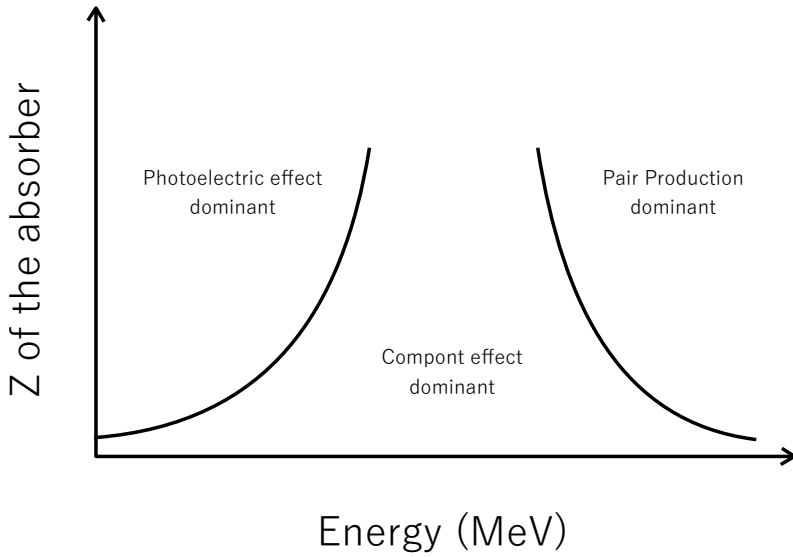


Fig. 1.15: depiction of the three different region in which each effect is dominant.

number, the line on the left depicts the energy at which photoelectric absorption and Compton scattering are equally likely. The right-hand line depicts the energy at which Compton scattering and pair creation are equally likely. On the plot, three zones are thus defined in which photoelectric absorption, Compton scattering, and pair creation each prevail.

1.2 Detection of ionizing radiation: scintillators

As mentioned above, all the ionizing radiations considered can be classified as high energy radiations. In particular, photons like x-rays or γ -rays belong to a portion of the electromagnetic spectrum that is invisible for our eyes, given their very short wavelengths. Standard direct detection technologies, such as Charged Coupled Devices (CCDs), are ineffective for higher X-ray energy >15 keV or 'Hard' X-rays. The solution is to incorporate a

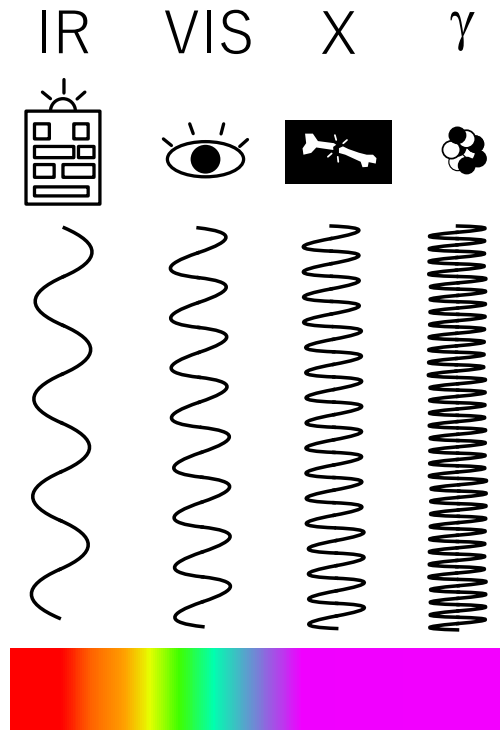
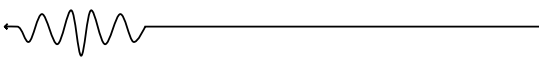


Fig. 1.16: part of the electromagnetic spectrum.



material called scintillator (or one called transducer) into the system to transform incident photons/particles into visible photons that can then be revealed by the detector.

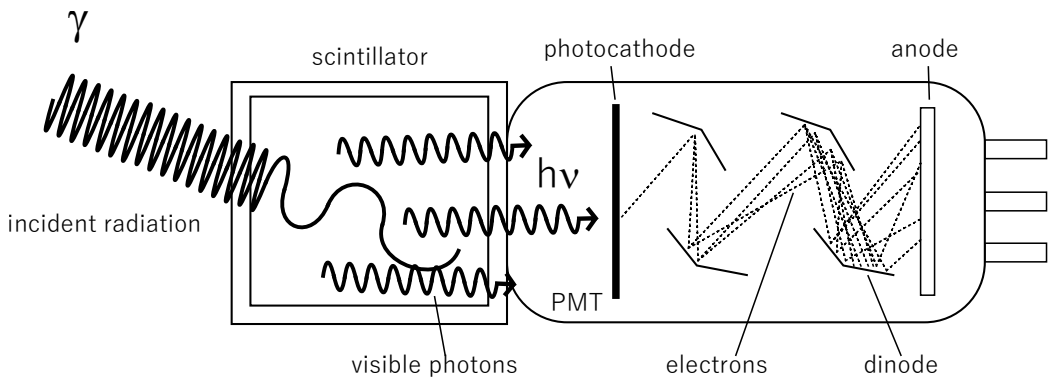


Fig. 1.17: simplified scheme of indirect detection.

Indeed, scintillators are materials in which high fractions of incident energy carried by impacting particles or radiation are absorbed and changed into measurable photons (visible or near visible light), which are then converted into an electric signal. The situation described above is usually referred to as indirect detection. Light emission can be classified into two types: fluorescence and phosphorescence. Fluorescence is the rapid emission of visible radiation from a substance after it has been excited in some way. It is customary to distinguish between numerous distinct processes that can result in the emission of visible light. Phosphorescence is the emission of longer wavelength light than fluorescence, and it has a significantly slower characteristic time. Delayed fluorescence produces the same emission spectrum as prompt fluorescence but has a significantly longer emission period after excitation. A good scintillator should convert as much of the incident photon energy as feasible to prompt fluorescence while limiting the generally undesired contributions from phosphorescence and delayed fluorescence¹⁹. Radiation detection employs both inorganic and organic scintillators. Different mechanisms are at the root of light creation in these two types of scintillators, as will be revealed later. Scintillators are defined by several parameters, but one of the most important is surely the scintillation efficiency, R_s . It is defined as the ratio of the average number of emitted photons $\langle N_{ph} \rangle$ to the incident radiation energy E_i deposited in the scintillator



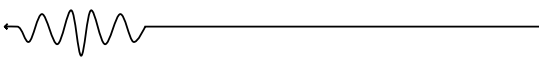
or absorbed by it:

$$R_s = \frac{\langle N_{ph} \rangle}{E_i}$$

If it is time-gated it is commonly referred to it as Light Yield (LY). The perfect scintillation material will have the following characteristics¹⁹:

- It should have a high scintillation efficiency in converting the kinetic energy of charged particles into visible light.
- This conversion should be linear. The light yield should be proportional to the deposited energy across the widest conceivable range.
- For effective light collection, the medium should be transparent to the wavelength of its own emission.
- The decay duration of the produced luminescence should be short in order to generate quick signal pulses.
- The material should be of good optical quality and capable of being manufactured in big enough proportions to be used as a practical detector.
- Its index of refraction should be close to that of glass (~1.5) for the scintillation light to be efficiently coupled to a photomultiplier tube or other light sensor.

No material can meet all these characteristics at the same time, therefore selecting a scintillator is always a compromise. The most used scintillators are inorganic alkali halide crystals, particularly sodium iodide, and organic-based liquids and plastics. With a few exceptions, inorganics have the best light output and linearity but are generally slow in response time. Organic scintillators are typically faster but produce less light. The planned application also has a significant impact on scintillator selection. Inorganic crystals are frequently favoured for gamma-ray spectroscopy due to their



high Z-value and density, but organics are often favoured for beta spectroscopy¹⁹.

1.2.1 The physics of scintillation

Inorganic scintillators

The mechanism of scintillation in inorganic materials is determined by the energy states of the material's crystal lattice. In materials classed as insulators or semiconductors, electrons have only distinct bands of energy available, as seen in Fig. 1.18.

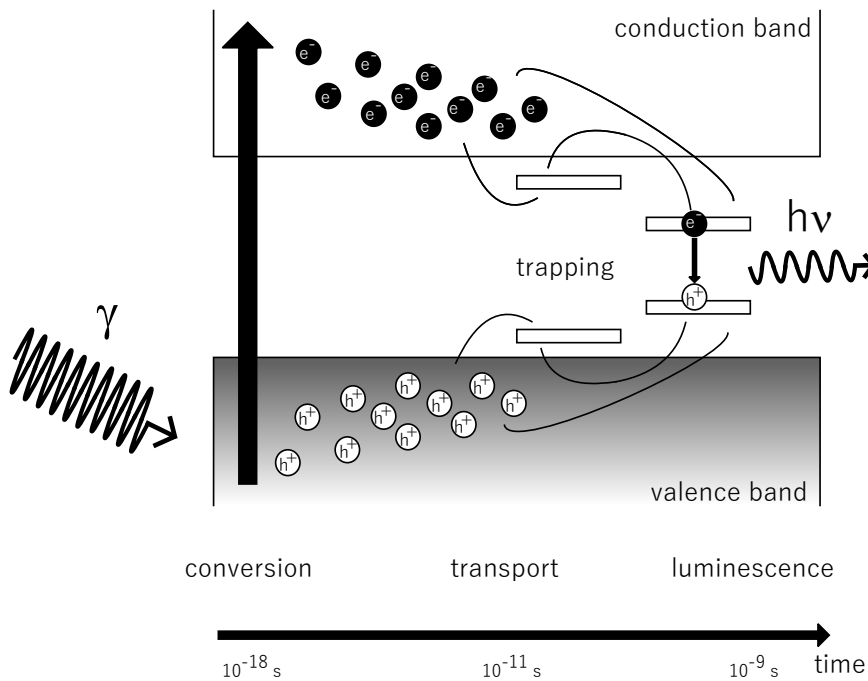
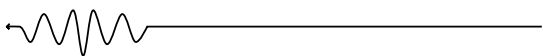


Fig. 1.18: scheme of the events happening in an inorganic scintillator upon the interaction with ionizing radiation. The γ ray interacts with the material ionizing it and then the as-generated free charges travel in the material until they meet a trap site and the the luminescence is generated.

The lower band, known as the valence band, represents electrons that are basically bonded to lattice sites, whereas the conduction band represents electrons that have enough energy to flow freely throughout the crystal. The forbidden band is an intermediate band of energies in which electrons can never be found in the pure crystal. Energy absorption can cause an electron to be elevated from its regular position in the valence band across the gap



into the conduction band, leaving a hole in the typically filled valence band. The return of the electron to the valence band with the emission of a photon is an inefficient process in a pure crystal. Furthermore, normal gap widths are such that the resultant photon has too much energy to be seen. Small amounts of an impurity are routinely added to inorganic scintillators to increase the likelihood of visible photon emission during the de-excitation process. Such purposefully inserted impurities, known as activators, produce specific places in the lattice where the regular energy band structure differs from that of the pure crystal. As a result, energy levels will be formed within the forbidden gap through which the electron can de-excite and return to the valence band. Because the energy is less than that of the entire prohibited gap, this transition can now produce a visible photon and so serve as the foundation for the scintillation process. These sites of de-excitation are known as luminescence centers or recombination centers. The energy structure of the scintillator in the host crystalline lattice controls its emission spectrum. When a charged particle passes through the detecting medium, it creates a significant number of electron-hole pairs due to electron elevation from the valence to the conduction band. Because the ionization energy of the impurity is lower than that of a conventional lattice site, the positive hole will swiftly wander to the location of an activator site and ionize it. Meanwhile, the electron is free to move through the crystal and will continue to do so until it encounters an ionized activator. The electron can now drop into the activator site, forming a neutral configuration with its own set of excited energy states (Fig. 1.18). If the created activator state is an excited configuration with an allowed transition to the ground state, de-excitation will occur very quickly and with a high probability, resulting in the emission of a corresponding photon. This transition can be in the visible energy range if the activator is suitably chosen. Lifetimes for such excited states are typically in the range of 50-500 ns. Because the electron's migration period is substantially shorter, all the excited impurity configurations are created basically all at once and will de-excite with the half-life typical of the excited state. Although some inorganic scintillators can be properly described by a single decay period or a simple exponential, more complex temporal behaviour is frequently observed. There are other processes that compete with the one mentioned above. When an electron arrives at an impurity site, it can generate an excited configuration whose transition to the ground state is restricted. Such states therefore necessitate an additional energy increment to elevate them to a higher-lying condition from which de-



excitation to the ground state is conceivable. Thermal excitation is one source of this energy, and the subsequent slow component of light is known as phosphorescence. It is a common source of background light or "afterglow" in scintillators. When an electron is trapped at an activator site, a third possibility exists. Certain radiationless transitions between some excited states obtained by electron capture and the ground state are feasible, in which case no visible photon is produced. Quenching processes describe loss mechanisms in the conversion of particle energy to scintillation light. Instead of the electron and hole migrating independently as stated above, the pair may migrate together in a loosely connected structure known as an exciton. In this situation, the electron and hole remain connected but are free to move within the crystal until they hit an activator atom. Similar excited activator configurations can be generated again, producing scintillation light upon deexcitation to the ground configuration. A simple energy calculation yields a measure of the efficiency of the scintillation process. It takes around three times the bandgap energy to make one electron-hole pair in a wide range of materials. One key result of luminescence via activator sites is that the crystal can be transparent to scintillation light. In a pure crystal, the energy required to excite an electron-hole pair is nearly the same as the energy liberated when that pair recombines. As a result, the emission and absorption spectra will overlap, and significant self-absorption will occur. However, as we have seen, emission from an activated crystal happens at an activator site with a lower energy transition than that represented by the formation of the electron-hole pair. As a result, the emission spectrum shifts to longer wavelengths and is no longer impacted by the bulk of the crystal's optical absorption band.

Organic scintillators

Because fluorescence in organics is caused by changes in the energy level structure of a single molecule, it can be observed from any molecular species regardless of its physical state. Anthracene, for example, has been reported to glow as a solid polycrystalline material, a vapor, or as part of a multicomponent solution. This characteristic contrasts sharply with that of crystalline inorganic scintillators like sodium iodide, which require a regular crystalline lattice as a foundation for the scintillation process. A broad class of viable organic scintillators is based on organic compounds having symmetry features that give rise to a p-electron structure. Fig. 1.19 depicts

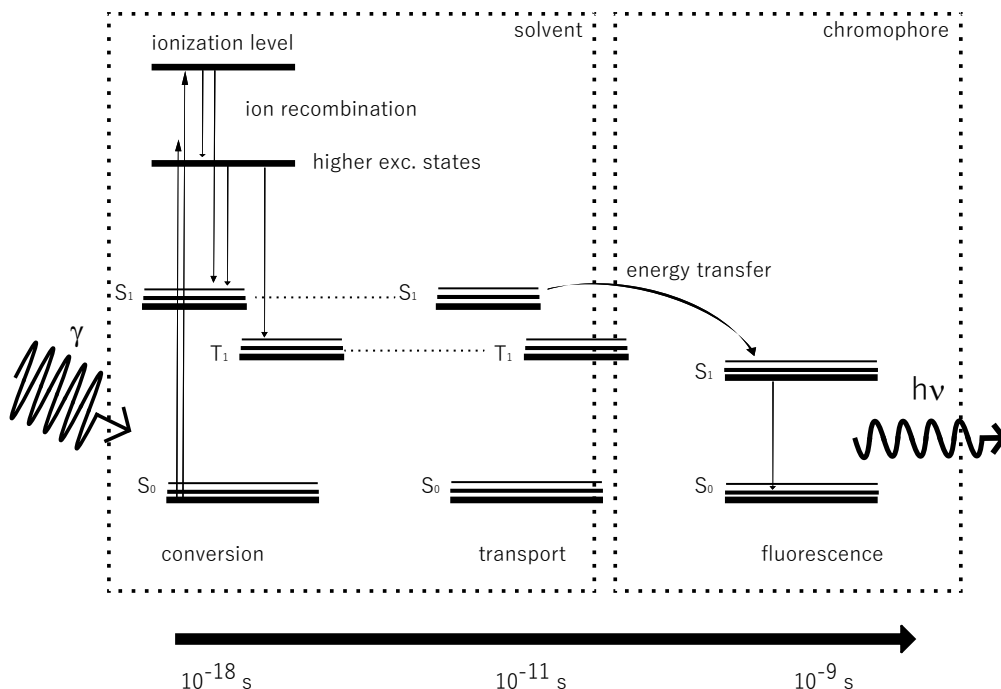
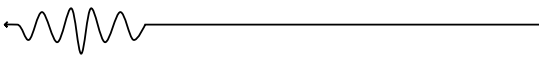


Fig. 1.19: sketch of the energy transition occurring inside an organic scintillator upon interaction with high energy radiations.

the p-electronic energy levels of such a molecule. Energy can be absorbed by causing the electron configuration to change into one of several excited states. In the picture, a sequence of singlet states (spin 0) are denoted as S_0 , S_1 , S_2 , etc. A similar set of triplet (spin 1) electronic levels is represented as T_1 , T_2 , T_3 , etc. The energy gap between S_0 and S_1 for molecules of interest as organic scintillators is 3 to 4 eV, although the spacing between higher-lying states is usually slightly smaller. Each of these electronic configurations is then subdivided into a number of levels with considerably finer spacing that correspond to different molecular vibrational states. The typical distance between these levels is 0.15 eV. To identify these vibrational states, a second subscript is frequently appended, and the sign S_{00} represents the lowest vibrational state of the ground electronic state. Because the space between vibrational states is considerable in comparison to average thermal energies (0.025 eV), practically all molecules are in the S_{00} state at room temperature. The arrows pointing upward in Fig. 1.19 depict the molecule's absorption of energy. These mechanisms describe the absorption of kinetic energy from a charged particle passing nearby in the case of a scintillator. The excited higher singlet electronic states are rapidly (on the order of picoseconds) de-excited to the S_{10} electron state via radiationless internal conversion.



Furthermore, any state with extra vibrational energy (such as S_{11} or S_{12}) is not thermally balanced with its neighbours and rapidly loses that vibrational energy. As a result, the net impact of the excitation process in a simple organic crystal is to produce a population of excited molecules in the S_{10}

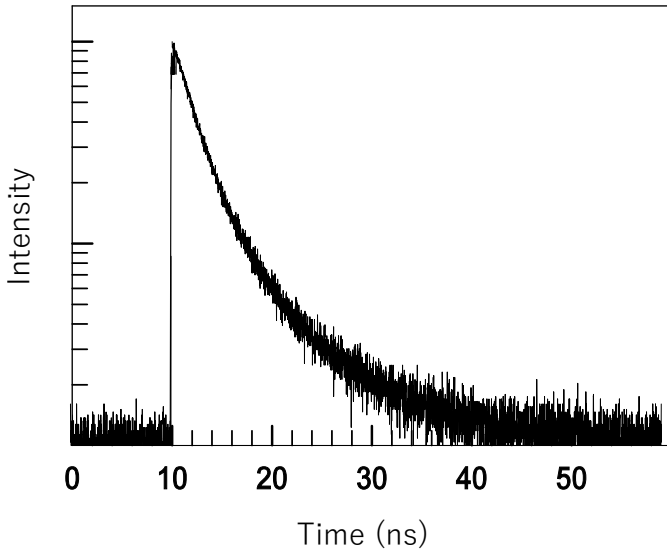


Fig. 1.20: decay of the intensity of the excited state in function of time.

state after a negligibly short period. The main scintillation light (or quick fluorescence) is emitted when this S_{10} state shifts to one of the vibrational states of the ground electronic state. The descending arrows in Fig. 1.19 represent these changes. If t is the S_{10} level's fluorescence decay period, then the prompt fluorescence intensity at time t after stimulation should simply be:

$$I = I_0 e^{-t/\tau}$$

where τ is the characteristic lifetime of emission from an excited state to the ground state. The parameter τ is usually a few nanoseconds in most organic scintillators, therefore the quick scintillation component is relatively fast. The lifespan of the initial triplet state T_1 is substantially longer than that of the singlet state S_1 . Some excited singlet states can be transformed to triplet states via a transition known as intersystem crossing. The lifespan of T_1 can be as long as 10^{-3} s, and the radiation emitted during a de-excitation from T_1 to S_0 is thus a delayed light emission known as phosphorescence. Because T_1 is lower in energy than S_1 , the wavelength of this phosphorescence spectrum is longer than the wavelength of the fluorescence spectrum. Some molecules in the T_1 state may be thermally stimulated back to the S_1 state and decay by regular fluorescence. This process is responsible for the delayed fluorescence that is sometimes observed in organics. Fig. 1.21 explains how organic scintillators can be transparent to their own fluorescence emission. The photon energy that will be strongly absorbed in the material are represented by the length of the upward arrows. Except for $S_{10} - S_{00}$, all the fluorescence transitions represented by the downward



arrows have a lower energy than the minimum required for excitation, so there is very little overlap between the optical absorption and emission spectra (often referred to as the Stokes shift), and thus little self-absorption of the fluorescence. Fig. 1.21 shows an example of these spectra for a typical organic scintillator. As said above, the scintillation efficiency is defined as the fraction of all incident particle energy that is transformed into visible light. One would like that this efficiency be as high as feasible, however there are various de-excitation modes available to excited molecules that do not entail the emission of light and in which the excitation is primarily degraded to heat. All these radiationless de-excitation processes are referred to as quenching. Impurities (such as dissolved oxygen in liquid scintillators) that decrease light output by providing other quenching mechanisms for the excitation energy are frequently removed during the production and use of organic scintillators. Before de-excitation happens in almost all organic materials, the excitation energy is transferred from molecule to molecule. This energy transfer method is especially relevant for the broad class of organic scintillators that contain many molecular types. When a little amount of an efficient scintillator is given to a bulk solvent, the energy absorbed, mostly by the solvent, can finally make its way to one of the efficient scintillation molecules and induce light emission. These "binary" organic scintillators are commonly employed in liquid and plastic solutions containing a wide range of solvents and scintillating compounds. The role of the secondary scintillant is to absorb the light produced by the primary scintillant and reradiate it at a longer wavelength. This change in the emission spectrum can be used to better match the spectral sensitivity of a photomultiplier tube or to reduce bulk self-absorption in large liquid or

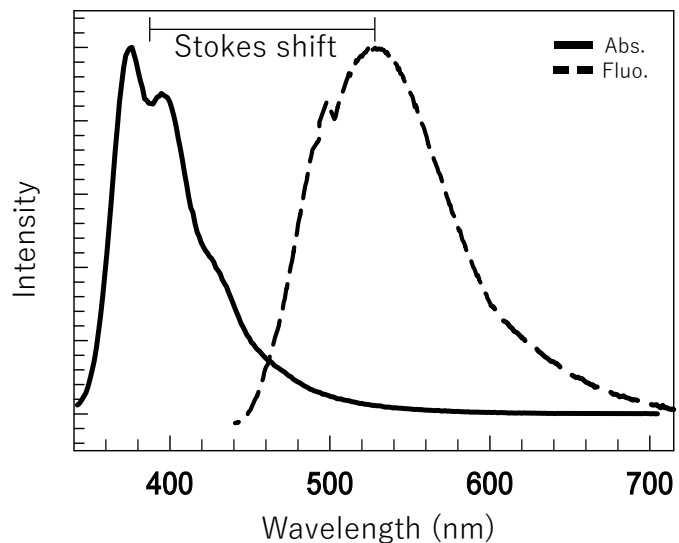
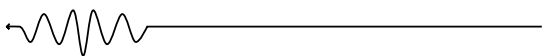


Fig. 1.21: representation of the Stokes shift as difference in wavelength between the absorption maximum and the emission maximum of a fluorescent dye.

and use of organic scintillators. Before de-excitation happens in almost all organic materials, the excitation energy is transferred from molecule to molecule. This energy transfer method is especially relevant for the broad class of organic scintillators that contain many molecular types. When a little amount of an efficient scintillator is given to a bulk solvent, the energy absorbed, mostly by the solvent, can finally make its way to one of the efficient scintillation molecules and induce light emission. These "binary" organic scintillators are commonly employed in liquid and plastic solutions containing a wide range of solvents and scintillating compounds. The role of the secondary scintillant is to absorb the light produced by the primary scintillant and reradiate it at a longer wavelength. This change in the emission spectrum can be used to better match the spectral sensitivity of a photomultiplier tube or to reduce bulk self-absorption in large liquid or



plastic scintillators. Birks and Pringle²⁰ examined the energy transfer mechanisms in binary and ternary organic mixtures, as well as their impact on scintillation efficiency and pulse timing properties. Below the main types of organic scintillators are described.

Organic crystals

As pure organic crystalline scintillators, only two materials have gained general acceptance. Anthracene is one of the oldest organic materials used for scintillation and has the best scintillation efficiency (or highest light production per unit energy) of any organic scintillator. Stilbene has a lower scintillation efficiency but is favoured in instances where pulse shape discrimination is required; discrimination is to be utilized to identify scintillations caused by charged particles and electrons. Both materials are brittle and difficult to get in significant quantities. Furthermore, the efficacy of scintillation is known to be dependent on the direction of an ionizing particle regarding the crystal axis²¹. If the incident radiation produces tracks in a range of directions within the crystal, this directional variation, which can be as high as 20-30%, degrades the energy resolution available with these crystals.

Liquid scintillators

Dissolving an organic scintillator in an adequate solvent yields a class of useful scintillators. A third ingredient is frequently introduced as a wavelength-shifter to adequate emission spectrum to better match the spectral response of common photomultiplier tubes in liquid scintillators. Liquid scintillators are frequently sold commercially in sealed glass containers and are handled similarly to solid scintillators. Large-volume detectors with diameters of several meters may be required in some applications. In these instances, the liquid scintillator is frequently the only cost-effective option. The presence of dissolved oxygen in many liquids can act as a severe quenching agent, resulting in significantly reduced fluorescence efficiency. The solution must next be sealed in a closed vessel that has been purged of most of the oxygen. Because they lack a solid structure that could be harmed by severe radiation, liquid scintillators are believed to be more radiation resistant than crystalline or plastic scintillators. Measurements support this notion, and reasonable resistance to change up to doses as high as 10^5 Gy has been demonstrated for several liquids²². Liquid



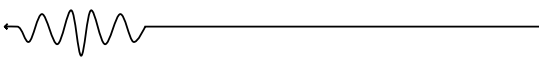
scintillators are also commonly used to count radioactive material that can be dissolved in the scintillator solution. In this situation, all radiations released by the source instantaneously travel through some section of the scintillator, and the counting efficiency can be nearly 100%. The approach is extensively used for measuring low-level beta activity, such as that emitted by carbon-14 or tritium.

Plastic scintillators

The equivalent of a “solid solution” can be generated by dissolving an organic scintillator in a solvent that can then be polymerized. A popular example is a solvent made of styrene monomer in which an organic scintillator is dissolved. After that, the styrene is polymerized to produce a solid plastic. Polyvinyltoluene (PVT) and polymethylmethacrylate (PMMA) are examples of other polymeric matrices. Plastics have become an incredibly valuable kind of organic scintillator due to the simplicity with which they may be shaped and produced. Plastic scintillators are commercially available in a wide range of conventional diameters for rods, cylinders, and flat sheets. Plastics are generally the only realistic alternative when large-volume solid scintillators are required due to their low cost. In these instances, the self-absorption of the scintillator light may no longer be insignificant, and the material's attenuation qualities should be considered. Light intensity can be reduced by a factor of two across several meters, while certain polymers exhibit substantially shorter attenuation lengths. Plastic scintillators are also available in a variety of small-diameter fibres. These scintillators, which may be used as single fibres or in bundles or ribbons, are well suited for applications where the location of particle interactions must be monitored with high spatial precision.

1.3 Radiation sources, hazards and benefits

On a daily basis, people are exposed to both natural and man-made radiation sources. Natural radiation is produced by a variety of sources, including over 60 naturally occurring radioactive elements present in soil, water, and air. Radon is a naturally occurring gas that is emitted by rock and soil and is the primary source of natural radiation. Every day, individuals breath in and consume radionuclides through the air, food, and water. Natural radiation from cosmic rays is



also a risk, especially at high altitudes. On average, naturally occurring terrestrial and cosmic radiation sources account for 80% of a person's annual dosage of background radiation. Because of geological changes, background radiation levels vary regionally. In certain regions, exposure can be more than 200 times higher than the world average. Human-made sources of radiation exposure include nuclear power generation and medical applications of radiation for diagnosis or treatment. People can be exposed to ionizing radiations in a variety of settings, including at home or in public areas (public exposures), at work (occupational exposures), and in a medical environment (medical exposures). Radiation exposure can occur through either internal or exterior mechanisms. Internal ionizing radiation exposure occurs when a radionuclide is breathed, swallowed, or otherwise enters the circulation (for example, by injection or wounds). Internal exposure is terminated when the radionuclide is removed from the body, either naturally (through excreta) or as a consequence of therapy. External exposure can occur when radioactive material in the air (such as dust, liquid, or aerosols) is deposited on the skin or clothing. This form of radioactive substance is frequently eliminated from the body by washing. Ionizing radiation exposure can also occur as a result of irradiation from an external source, such as medical radiation exposure via x-rays. When the radiation source is protected or the



Fig. 1.22: Homer Simpson handling an uranium bar in Simpsons opening.



individual travels outside the radiation field, external irradiation ceases. For radiation safety reasons, ionizing radiation exposure may be divided into three categories: planned, existent, and emergency. Planned exposure circumstances emerge from the planned introduction and operation of radiation sources for specified reasons, such as medical use of radiation for patient diagnosis or treatment, or industrial or research use of radiation. Existing exposure happens when radiation already exists and a control decision must be made, such as radon exposure in homes or workplaces or natural background radiation from the environment. Unexpected incidents needing immediate action, such as nuclear catastrophes or criminal activities, create emergency exposure scenarios. The use of radiation for medical purposes accounts for 98% of the population dose contribution from all human-made sources, and accounts for 20% of total population exposure. Every year, over 4200 million diagnostic radiological exams are conducted globally, 40 million nuclear medicine procedures are performed, and 8.5 million radiation treatments are administered. Beside medical use, the effect of ionizing radiation on health could very serious. Radiation damage to tissue and/or organs is determined by the dosage of radiation received, or the absorbed dose, which is measured in Grays (Gy). The potential harm from an absorbed dosage is determined by the kind of radiation and the sensitivity of various tissues and organs. The effective dose is used to assess the potential for damage from ionizing radiation. The sievert (Sv) is a measure of effective dosage that considers the kind of radiation as well as the sensitivity of tissues and organs. It is a method of assessing the potential for ionizing radiation to cause injury. Aside from the amount of radiation (dose), another crucial characteristic is the rate at which

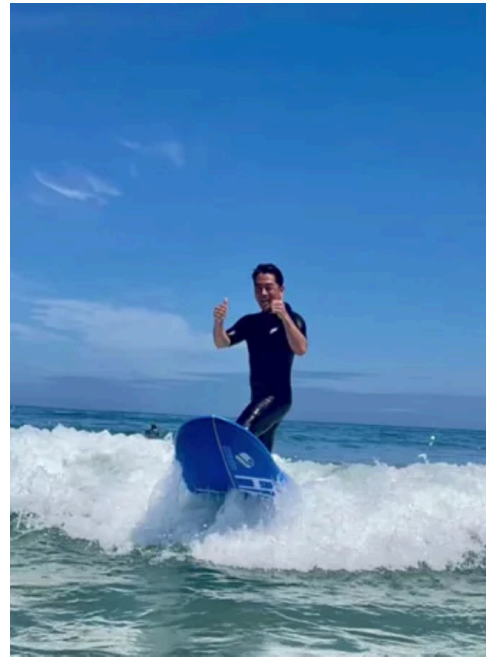
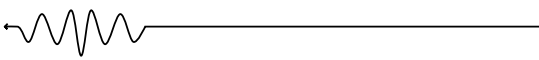


Fig. 1.23: Japanese liberal democratic party member Shinjiro Koizumi surfing in the water of Fukushima after the releasing of contaminated water, via PORTALFIELD News.



the dosage is administered (dose rate), which is expressed in microsieverts per hour (Sv/hour) or millisieverts per year (mSv/year). Radiation can damage the functioning of tissues and/or organs over specific thresholds and cause acute consequences such as skin redness, hair loss, radiation burns, or acute radiation syndrome. These effects are more severe with greater dosages and rates of administration. The dosage threshold for acute radiation sickness, for example, is around 1 Sv (1000 mSv). If the radiation dosage is minimal and/or provided over a lengthy period of time (low dose rate), the danger is significantly reduced since the damage is more likely to be repaired. An example could be found in the release of the tritium contaminated water of the Fukushima nuclear central in the Pacific Ocean, started from the 24th August 2023 and that will last decades. Acting in this way, the balance between the tritium naturally contained in the oceanic water will always be balanced because of water evaporation. On the other side, nuclear and radioactive sources could very beneficial in different fields, from medicine to biology. Medical instruments, such as x-ray machines and computed tomography (CT) scanners, are the most frequent man-made emitters of ionizing radiation today. Among the various applications of nuclear radiation for human health, the technology of medical radiation imaging for cancer detection and treatment is used across the world, and research in its development and applications is progressing at a rapid pace. Imaging with radiation medicine techniques is frequently the initial step in clinical management and diagnostic radiography, and nuclear medicine studies play essential roles in cancer screening, staging, therapy monitoring, and long-term surveillance. Moreover, the use of isotopes in biology has a long history. For example, the use of a radioactive tracer in biological sciences may be traced back to Melvin Calvin's work, in which he and colleagues employed the radioactive isotope carbon-14 as a tracer for CO₂ to describe the first metabolic steps in plant photosynthesis. He was awarded the Nobel Prize in Chemistry in 1961 for "his research on carbon dioxide assimilation in plants", according to the Nobel Committee.



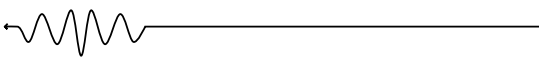
1.4 Focus on radioactive gases

It is now clear that the control of radioactive sources is a main issue for human safety and environmental protection, but also for diagnostics. One may think to radioactive substances as glowing heavy solid materials as seen in various tv series or cartoons. Indeed, at the beginning of this introductory chapter, we talked about the experiments of Becquerel and Marie Curie regarding pieces of high-Z materials such as potassium-uranyl sulfate that turned out to be one of the first examples of a radioactive material. Not so surprising is finding out that also gases can be radioactive. Consider isotopes such as ^{85}Kr and ^3H emitted by nuclear power plants, reprocessing plants, and nuclear waste treatment facilities²³: they are crucial to detect and monitor nuclear activities and expose unlawful reprocessing to produce plutonium for weapons. The elements ^{133}Xe and ^{37}Ar are particularly interesting because they may be used to identify clandestine activity and verify conformity with the Comprehensive Nuclear-Test-Ban Treaty²⁴. Gases from granite-rich areas, on the other hand, are pathogenic agents that must be quantified to reduce exposure risk, whereas xenon isotopes can be used as radioactive diagnostic contrast agents to evaluate pulmonary function, lung imaging, and cerebral blood flow via inhalation. The detection and radioactive metrology of gases is therefore an important feature of a contemporary, technologically sophisticated, and sustainable society, as seen by the frequent revisions of laws that demand increasingly sensitive detectors.

1.4.1 Gas of interest, hazard, and regulations

Radon-222 and Radon-220

Radon is a chemical element of the periodic table indicated with the symbol Rn with an atomic number $Z=86$. It is a noble, radioactive gas produced by the α -decay of radium, which in turn is produced by the α -decay of uranium. Polonium and bismuth are the highly toxic products of the radioactive decay of radon. The most hazardous isotopes of radon are ^{220}Rn and ^{222}Rn with a half-life of 56 second and 3.82 days, respectively. Thus, the presence of Rn is from natural geological sources: being very soluble in water, Rn is detectable in traces in superficial water (like lakes or rivers) while it is very concentrated in deep underground aquifers. Moreover, it is present in minerals and so in buildings too. The first evidence that radon might cause



lung cancer dates back to the early twentieth century, based on the disease's high frequency among Czechoslovakian miners. Research on lung cancer risk, begun in the late 1960s and based on radon measurements taken in Czechoslovakia uranium mines since 1949²⁵, was the second globally to establish the danger associated with cumulative exposure to radon progeny. Radiation protection measures for uranium miners, including radon monitoring, began to be adopted in numerous European nations beginning in the 1970s. Because of the incidence of increased radon levels in households, it was not until the mid-1980s that radon exposure was recognized not only as an occupational concern, but also as a possible public health risk²⁶. The current EU legislative framework for radon protection is outlined in regulation 2013/59/Euratom²⁷ (also known as the EU-BSS regulation or EU-BSS). This regulation is binding on EU Member States, but it has also been accepted by a number of non-EU nations, including Norway, the United Kingdom, and Switzerland. Articles 54 and 35.2 explicitly handle radon exposure in workplaces, whereas item 74 specifically addresses radon exposure in residences. In EU, for both workplaces and households, reference values of no more than 300 Bq m⁻³ must be established.

Xenon-133

¹³³Xe is a radioisotope that exists as a gas. It is mostly utilized for lung perfusion tests, which are used to diagnose lung diseases²⁸. It is also used to visualize blood flow, especially in the brain²⁹. ¹³³Xe is also an important fission product (together with ¹³¹Xe, ^{133m}Xe and ¹³⁵Xe). It is discharged to the atmosphere in small quantities by some nuclear power plants³⁰. It emits β^- particle in coincidence with γ rays, with a half-life of 5.7 days. Monitoring radioxenon concentrations in the atmosphere is important for providing evidence of atmospheric or subterranean nuclear bomb testing. As previously stated, radiopharmaceutical plants create the four radioactive xenon isotopes of importance for detecting nuclear bomb testing³¹. Each medical isotope manufacturing facility generates a few TBq of ¹³³Xe every day³², whereas nuclear power facilities release a few GBq of ¹³³Xe per reactor. In comparison, in the case of an underground 1 kT nuclear bomb test, releasing 1% of the initially created ¹³³Xe into the atmosphere would result in a few tenths of TBq of ¹³³Xe. As a result, depending on the location of the release and the weather circumstances, ¹³³Xe from industrial activity is likely to be detected at International Monitoring System (IMS) stations in amounts



comparable to those predicted from a nuclear explosion. This makes distinguishing between civilian and military uses extremely difficult³³.

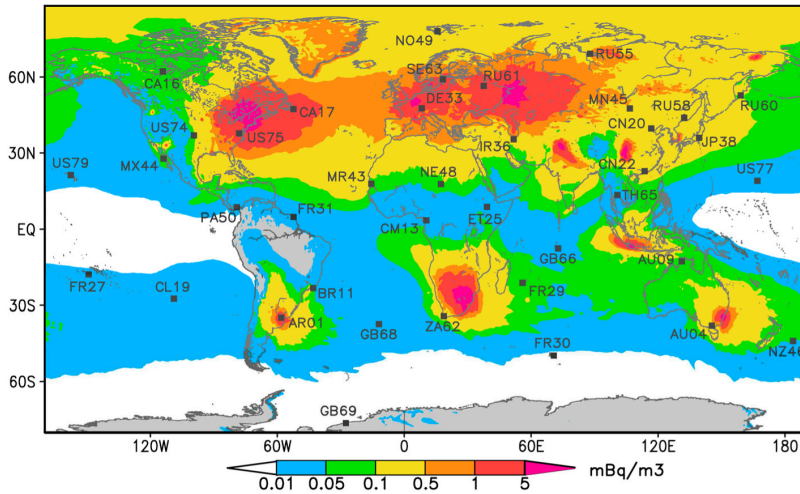


Fig. 1.24: Annual average activity concentrations of Xe-133 calculated from two years of simulated data, at ground level. The noble gas stations of the IMS are shown in black squares³³.

Krypton-85

Krypton-85 (⁸⁵Kr) is a radioactive isotope of the element krypton, which degrades to the stable rubidium-85. Its half-life is 10.756 years, and the highest decay energy is 687 keV. The most prevalent decay (99.57%) is β^- particle emission, with a maximum energy of 687 keV and an average energy of 251 keV. The second most common decay (0.43%) is β^- particle emission with the highest energy of 173 keV. γ ray emission (maximum energy of 514 keV) is the third most common decay. Other decay modes have low probability and produce less intense γ rays³⁴. Krypton-85 is created in modest quantities in the atmosphere by the interaction of

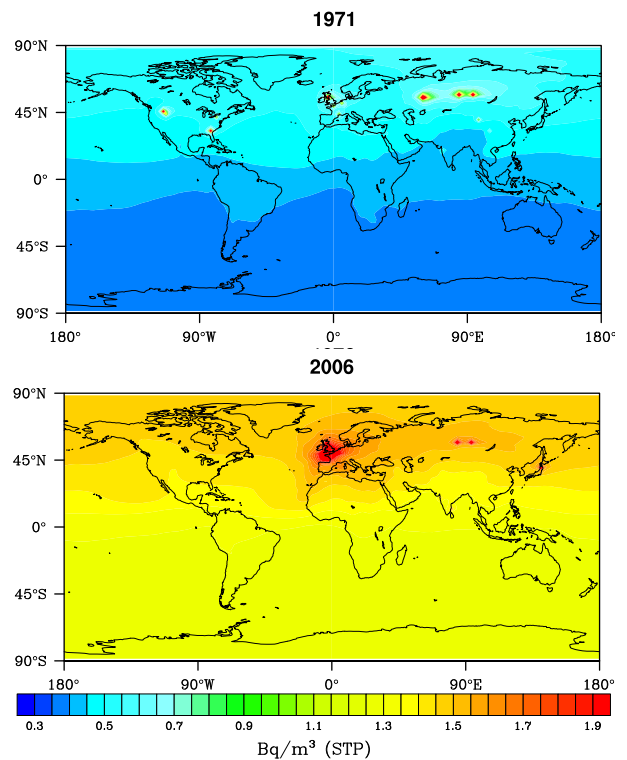
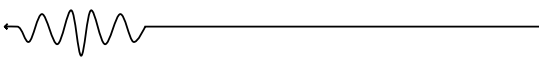


Fig. 1.25: Annual mean ⁸⁵Kr concentration at the surface in 1976 and in 2006³³.



cosmic rays with stable krypton-84. Natural sources keep an equilibrium inventory of around 0.09 pBq in the atmosphere. On the other hand, ^{85}Kr can also be anthropogenic, being one of the medium-lived fission products in nuclear fuel reprocessing³⁵. Indeed, Reprocessing spent nuclear fuel and separating the contained plutonium from it is one route to a nuclear weapon. As a result, the capacity to detect covert nuclear reprocessing plants is crucial for nuclear weapons control and non-proliferation. Previous research has established ^{85}Kr as the best environmental tracer for detecting and quantifying such nuclear reprocessing activity³⁵. For many years to come, the ^{85}Kr background will be too high to support an efficient stationary network like the one used for CTBT verification. In comparison, the CTBTO's International Monitoring System depends on 40 noble-gas monitoring stations across the world to identify ^{133}Xe emissions from nuclear explosions²⁴. There are ^{133}Xe background sources, mostly medical isotope manufacturing facilities, but no worldwide baseline has been established due to its short half-life of 5.2 days. As a result, 40 stations are sufficient to cover the majority of the world. The amplitudes of ^{85}Kr source terms from reprocessing are equivalent to those of ^{133}Xe source terms from nuclear explosions, but due to the high ^{85}Kr baseline, plumes from recent emissions become indistinguishable within 2/3 days and a few hundred kilometers³⁶. In instance, ^{133}Xe emissions from a North Korean nuclear test in 2006 were observable 14 days later and across a distance of 7000 km in Canada³⁷. As a result, a fixed network for ^{85}Kr monitoring to identify clandestine reprocessing is now impractical due to the sheer number of stations required to cover the whole globe. Instead, it appears that a technique in which a large number of air samples are collected at random over the Earth's landmass and examined in a smaller number of regional laboratories is more realistic³⁸.

Argon-37

Argon-37 is a radioactive isotope of Argon generated from in-situ neutron activation of Calcium-40. From the event of electron capture, the primary ^{37}Ar nuclear decay signature consists of five low-energy Auger electrons with a total energy of 2.5 keV. The presence of ^{37}Ar , as ^{133}Xe , is mostly related to the occurring of nuclear explosion (being its natural background level very low due to only cosmic rays interaction with geological ^{40}Ca). The quantity of ^{37}Ar created by a nuclear event is determined by the number of neutrons produced as well as the amount of ^{40}Ca in the surrounding geology. Most



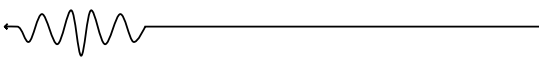
fission and activation products from an underground event will be retained within the explosion cavity in a well-contained test; nevertheless, the chemically inert properties of Ar and Xe can result in these two gases migrating through the subsurface to ground level. The relatively long half-life of ^{37}Ar of 35 days is appealing because it allows field teams to begin operations while also providing a visible signal near the surface for several months. This fact could be beneficial for the detection of clandestine nuclear test but, on the other hand, the low decay energy of ^{37}Ar makes it very hard to detect.

H-3 (Tritium)

Tritium is a radioactive hydrogen isotope with a half-life of 12.3 years. It degrades by emitting a β -particle with a maximum energy of 18.7 keV and an average energy of 5.7 keV³⁹. In tissue, the mean free path of tritium's decay beta particle is roughly 0.6 μm , which equals the diameter of a human chromosome. It may be found in nature mostly as elemental tritium (HT) and radioactive water (HTO). Tritium has unusual properties that make dosimetry and health-risk evaluation difficult. For example, tritium in gas form may permeate through practically any container, including steel, aluminum, and plastics. Tritium in the oxide form is largely undetectable by frequently used survey tools. Tritium may be taken up by all hydrogen-containing molecules in the environment, causing it to spread broadly on a global scale. Tritium may enter the human body by inhalation, ingestion, and skin diffusion. Its detrimental effects are only seen after it is absorbed by the body. Several sources contribute to the tritium inventory in our environment. Cosmic ray interactions with atmospheric molecules, nuclear reactions in the earth's crust, nuclear testing in the atmosphere, continuous release of tritium from nuclear power plants and tritium production facilities under normal operation, incidental releases from these facilities, and consumer products are examples of these³⁹. Thus, as for other gases in this list, the tritium level monitoring is essential for security and safety. The need of detectors able to discriminate the effective rise of this level in comparison to the natural or facility-related background is really pushing.

1.4.2 State of the art in β emitting gas detection and metrology

Thus, radioactive gas detection is a serious matter of study and its application is strictly related to human health, safety and sustainability.



However, nowadays technology has several limitations regarding the detection, especially for what concerns pure β emitting gas as those studied in Section 1.4.1. Because of the short-range path of β particles in matter,

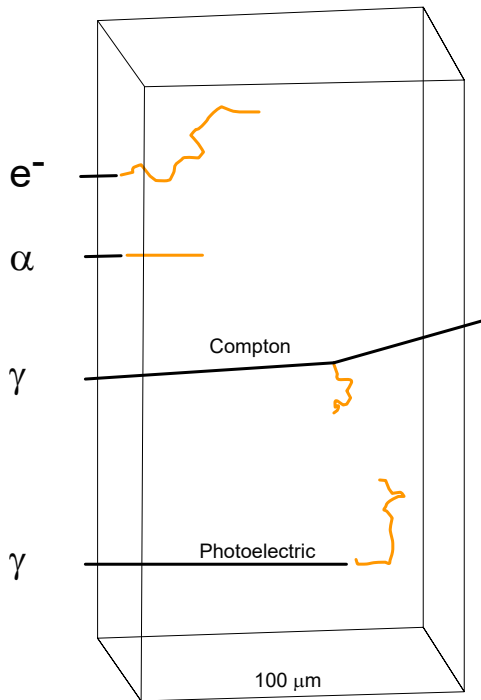


Fig. 1.26: transport of ionizing photons and particles in matter.

detecting electron emitters in fluid is often difficult. In contrast to photons, electrons interact with matter and deposit energy as seen in Section 1.1.4. Liquid scintillation counting techniques (LSC) are the gold standard in environmental laboratories for measuring radioactive liquids and gases. In the case of gas analysis, it is bubbled in a solution containing an aromatic solvent and a fluorophore such as 2,5-diphenyloxazole (PPO), resulting in the formation of a liquid scintillator (LS). In laboratories, the solution is deposited in conventional liquid scintillation vials, and detection is accomplished using calibrated

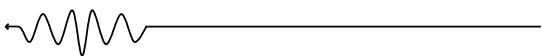
commercial LSC counters equipped with two photomultiplier tubes (PMTs) that function in tandem to ensure the rejection of PMT noise. In National Metrology Institutes, the LS vials are tested with three PMT detectors to get absolute measurements using the triple to double coincidence ratio (TDCR) approach (See Chapter 3). The employment of this technology on a broad scale produces a substantial quantity of organic pollution and necessitates the mixing of gas and liquid, resulting in dual chemical and radioactive waste. On the other hand, on-site measurements of certain isotopes in the environment make use of advanced detection techniques. Several systems for measuring β emitter gas have been developed, based on the radionuclide (energy of emission) and activity concentration to detect, as well as the sort of measurements necessary. Some commercial systems that use an ionisation chamber or a silicon drift detector to measure the activity concentration of noble gases in the atmosphere have been created. These detectors are sufficiently efficient for routine environmental research



(radioprotection and radon risk) in the case of radon isotopes (α -emitter). In recent years, advanced approaches such as SPALAX-NG⁴⁰ and SAUNA⁴¹ have been developed to monitor low concentrations of Xe isotopes in air, relying on coincidence techniques and massive filtration and compressor gas systems to minimize the detection limit. It is employed by the CTBTO. One of the primary concerns with these systems is the lack of quality control and calibration, which are confined to select tests done with CEA/LNHB or are at a high level of activity concentration. One of the primary challenges is then the certification and calibration of such equipment, which necessitate a well-known traceability of the measurement connection to a radioactive reference standard. As a result, National Metrology Institutes like CEA/LNHB⁴⁰ have created primary standards based on the triple compensated length proportional counter to offer worldwide traceability for reference gases standards^{42,43}. However, such a technique needs mixing the noble gas with a gas counting such as propane and then measuring it with an activity range of 2.5 to 15000 Bq cm⁻³, which is quite high in comparison to environmental value. Furthermore, in this concentration range, this approach is limited to the isotopes ¹³³Xe, ³H, and ⁸⁵Kr with a relative standard uncertainty of 0.6% and ¹²⁷Xe, ^{131m}Xe, and ^{133m}Xe with a greater relative standard uncertainty of 1%. Despite this, there is no standard at the level of some Bq m⁻³ for ¹³³Xe, ³H, and ⁸⁵Kr, and no standard at all for ³⁷Ar. This sophisticated technology is also presently only being used in national laboratories in France, the United Kingdom, and Korea, and is being developed in China with the assistance of CEA/LNHB. It should be noted that a specialized proportional counter, specifically for ³⁷Ar, has also been created in the United States, yielding a high sensitivity (1.2 mBq m⁻³) at the expense of an underground laboratory and ultra-purified material used to achieve ultra-low background counting. Furthermore, certain metrology institutions experienced contamination with ³H in the counter, necessitating a lengthy decontamination process.

1.4.3 Thesis focus: Metal-Organic Frameworks as porous scintillators.

Briefly, the liquid scintillation counting technique is the gold standard for measuring radioactivity but mixing ³H-labeled water with the scintillator is a time-consuming and difficult operation. This impedes in-situ online measurements and generates liquid radioactive waste that must be controlled properly. Furthermore, it cannot be used with other insoluble gas radionuclides. The only choice in this circumstance is to utilize gas meters



that require enormous quantities of gases to maximize detection efficiency, resulting in extremely impractical equipment. To overcome the limitations of the detection systems described above, new solutions are being explored. One of these could be the realization of porous scintillators. In general, porous materials are materials able to adsorb gases or liquids, acting like “sponges”. This property can guarantee a perfect intermixing between the matrix and the adsorbed fluid without any problem of miscibility. Moreover, porous materials can be very light and shapable, like aerogels. The possibility that a material with these characteristics can also be a scintillator looks very

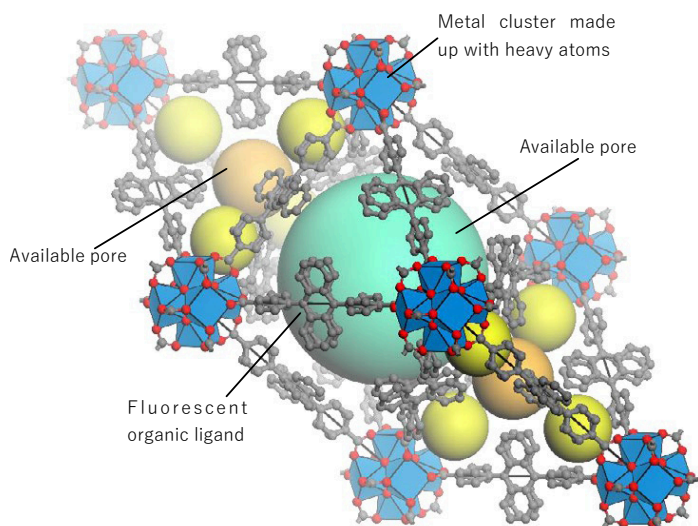
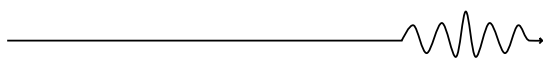


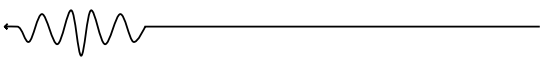
Fig. 1.27: Metal-Organic Framework 3D illustration. In this case, the framework displays heavy metal clusters (blue) linked one another with a fluorescent (conjugated) ligand (grey). In the picture are also indicated the different cavity that can be made with a three dimensional architecture like the one depicted. These cavities are particularly suitable for hosting gases.

promising for the future of gas detection, opening new ways for nuclear power plants security and human safety. Indeed, this work will focus on the realization, study and use of solid porous scintillators as detectors for radioactive gases. In particular, the aim of the study will be to prove for the first time the gas detection scintillation efficiency of a well-known class of materials, Metal-Organic Frameworks (MOFs). These are a type of

hybrid materials composed of organic molecules known as ligands that are coordinated to metal ions or clusters. These building components have exceptional self-assembly characteristics, allowing for the controlled creation of crystalline MOFs in one, two, or three dimensions⁴⁴⁻⁴⁶. Moreover, their size can range from mm to nm. The tuneable porosity of these hybrid materials has sparked interest in them, making MOFs suitable candidates for industrial applications such as gas storage and detection. In the last two decades, there has been a surge in study on this topic, giving rise to a vast family of multifunctional materials. Allendorf and colleagues' pioneering work proved that luminous Metal-Organic Frameworks may function as scintillators, implying the creation of a new class of materials with the requisite level of structural and composition control⁴⁷. Scintillating organic



chromophores can be used as ligands in MOFs, resulting in fluorescent ordered networks of molecular-size scintillators linked by high atomic number (Z) elements (metal ions) capable of interacting with ionizing radiation and sensitizing the ligand luminescence⁴⁸. Importantly, if appropriately built, these structures can maintain the qualities of constituent fluorophores that do not interact with one another, such as fluorescence yield and quick recombination dynamics, which are critical for the creation of fast and sensitive detectors. The fluorophores may be dissociated from one another and behave as gases in a solid-state medium. In comparison to the known scintillation materials now under investigation, MOFs display an excellent opportunity to generate the potential for rational design of a new generation of scintillators due to the adaptability of crystalline engineering. The formulation and creation of such system is the basis of the project SPARTE (Scintillating Porous Architecture for RadioacTivE gas detection), a consortium of different universities joint together under the European program Horizon 2020 to reinvent the gas detection paradigm. Thus, the SPARTE project is the frame of the three years Ph.D. program in which I was involved in the University of Milano-Bicocca (UNIMIB). I was specifically involved in the study of the photo- and radioluminescence properties of MOFs as scintillating porous materials for radioactive gas detection and metrology. MOFs are not the only matter of study for SPARTE, also aerogels come into play. Indeed, to better frame SPARTE, the next chapter will be a description of the activities of the project with a discussion on all the different participating and collaborating working packages (WPs).

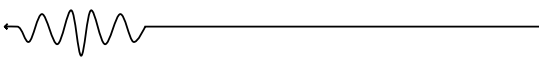


1.5 References

1. Röntgen, W. On a New Kind of Rays. *Nature* **53**, 274–246 (1896).
2. Allisy, A. Henri Becquerel: The Discovery of Radioactivity. *Radiat Prot Dosimetry* **68**, 3–10 (1996).
3. Becquerel, H. Sur les radiations émises par phosphorescence. *Comptes rendus de l'Académie des Sciences* 420–421 (1896).
4. Skłodowska Curie, M. Rayons émis par les composés de l'uranium et du thorium. *Comptes rendus de l'Académie des Sciences* 1101–1103 (1898).
5. Radvanyi, P. & Villain, J. The discovery of radioactivity. *Comptes Rendus Physique* vol. 18 544–550 Preprint at <https://doi.org/10.1016/j.crhy.2017.10.008> (2017).
6. Skłodowska Curie, M., Curie, P. & Bemont, G. Sur une nouvelle substance fortement radio-active contenue dans la pechblende. *Comptes rendus de l'Académie des Sciences* 1215–1217 (1898).
7. Villard, P. Sur la réflexion et la réfraction des rayons cathodiques et des rayons déviables du radium. *Comptes rendus* 1010–1012 (1900).
8. Krane, K. S., Wiley, J., York, N., Brisbane, C. & Singapore, T. *INTRODUCTORY NUCLEAR PHYSICS*. (1988).
9. Wigner, E., Tuve, M. A., Heydenburg, N. P. & Hafstad, L. R. On the Consequences of the Symmetry of the Nuclear Hamiltonian on the Spectroscopy of Nuclei. *Phys. Rev.* 106 (1937).
10. Goeppert Mayer, M. On Closed Shells in Nuclei. II. *Phys. Rev.* (1949).
11. Loveland, W. D., Morrissey, D. J. & Seaborg, G. T. (Glenn T. Modern nuclear chemistry. (Wiley-Interscience, 2006).
12. Prince, J. R. Comments on equilibrium, transient equilibrium, and secular equilibrium in serial radioactive decay. *J Nuc. Med.* 162–164 (1979).
13. Whaites, E. *Essentials of Dental Radiography and Radiology*.
14. L'Annunziata, M. *Radioactivity Introduction and History*. (Elsevier, 2007).
15. Alvarez, L. Nuclear K Electron Capture. *Physical Review* 134–135 (1937).



16. Leroy, G. & Rancoita, P. G. Principles of radiation interaction in matter and detection. (World Scientific Publishing Co. Pte. Ltd., 2009).
17. Bigelow, R. Nuclear and particle physics simulations. (1995).
18. Einstein, A. Concerning an heuristic point of view toward the emission and transformation of light. *Ann Phys* (1905).
19. Knoll, G. F. Radiation detection and measurement. (Wiley, 2000).
20. Birks, J. B. & Pringle, R. W. Organic Scintillators with Improved Timing Characteristics. *Proceedings of the Royal Society of Edinburgh. Section A. Mathematical and Physical Sciences* **70**, 233–244 (1972).
21. Brooks, F. D. & Jones, D. T. L. Directional anisotropy in organic scintillation crystals. *Nuclear instruments and methods* **121**, 69–76 (1974).
22. Zorn, C. & et al. Radiation damage effect on liquid scintillating fibers. *Radiation Physics and Chemistry* **41**, 237–242 (1993).
23. Schoeppner, M. & Glaser, A. Present and future potential of krypton-85 for the detection of clandestine reprocessing plants for treaty verification. *J Environ Radioact* **162–163**, 300–309 (2016).
24. Comprehensive Nuclear-Test-Ban Treaty Organization (CTBTO, 2022); <https://www.ctbto.org/>.
25. Pirchan, A. & Sikl, H. Cancer of the lung in the miners of Jachymov (Joachimstal). *Am J Cancer* **16**, (1932).
26. Swedjemark, G. A. The history of radon from a Swedish perspective. *Radiat Prot Dosimetry* **109**, 421–426 (2004).
27. Council Directive 2013/59/Euratom of 5 December 2013 laying down basic safety standards for protection against the dangers arising from exposure to ionising radiation, and repealing Directives 89/618/Euratom, 90/641/Euratom, 96/29/Euratom, 97/43/Euratom and 2003/122/Euratom.
28. Gold, W. M. & Koth, L. L. Pulmonary function testing.
29. Hoshi, H. & et al. Cerebral blood flow imaging in patients with brain tumor and arterio-venous malformation using Tc-99m hexamethylpropylene-amine oxime--a comparison with Xe-133 and IMP. *Kaku Igaku* 1617–1623 (1987).



30. Tachimori, S. & Amano, H. Preliminary study on production of xenon-133 from neutron-irradiated uranium metal and oxides by oxidation. *J Nucl Sci Technol* **11**, 488–494 (1974).
31. Matthews, K. M., Bowyer, T. W., Saey, P. R. J. & Payne, R. F. The Workshop on Signatures of Medical and Industrial Isotope Production - WOSMIP; Strassoldo, Italy, 1-3 July 2009. *J Environ Radioact* **110**, 1–6 (2012).
32. Gueibe, C. et al. Setting the baseline for estimated background observations at IMS systems of four radioxenon isotopes in 2014. *J Environ Radioact* **178–179**, 297–314 (2017).
33. Achim, P. et al. Characterization of Xe-133 global atmospheric background: Implications for the international monitoring system of the comprehensive nuclear-test-ban treaty. *J Geophys Res* **121**, 4951–4966 (2016).
34. Sievers, H. Nuclear data sheets update for A=85. *Nuclear Data Sheets* **62**, 271–365 (1991).
35. Kalinowski, M. & et al. Conclusions on plutonium separation from atmospheric krypton-85 measured at various distances from the Karlsruhe reprocessing plant. *J Environ Radioact* **73**, 203–222 (2004).
36. Ole, J. & Berichte Zur Erdsystemforschung, R. Simulation of atmospheric krypton-85 transport to assess the detectability of clandestine nuclear reprocessing. (2010).
37. Saey, P. R. J. et al. A long distance measurement of radioxenon in Yellowknife, Canada, in late October 2006. *Geophys Res Lett* **34**, (2007).
38. Schoeppner, M. & Glaser, A. Present and future potential of krypton-85 for the detection of clandestine reprocessing plants for treaty verification. *J Environ Radioact* **162–163**, 300–309 (2016).
39. Okada, S. & Momoshimat, N. Overview on tritium: characteristics, sources, and problems. (1993).
40. Le Petit, G. et al. Spalax™ new generation: A sensitive and selective noble gas system for nuclear explosion monitoring. *Applied Radiation and Isotopes* **103**, 102–114 (2015).



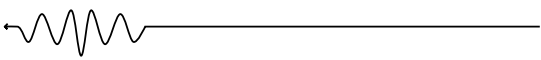
41. Aldener, M. et al. SAUNA field - A sensitive system for analysis of radioxenon in soil gas samples. *J Environ Radioact* **240**, (2021).
42. Unterweger, M., Johansson, L., Karam, L., Rodrigues, M. & Yunoki, A. Uncertainties in internal gas counting. *Metrologia* **52**, S156–S164 (2015).
43. Ratel, G. Uncertainty vade-mecum in radioactivity measurement. *Metrologia* **44**, (2007).
44. Férey, G. & Serre, C. Large breathing effects in three-dimensional porous hybrid matter: Facts, analyses, rules and consequences. *Chem Soc Rev* **38**, 1380–1399 (2009).
45. Kitagawa, S., Kitaura, R. & Noro, S. I. Functional porous coordination polymers. *Angewandte Chemie - International Edition* vol. 43 2334–2375 Preprint at <https://doi.org/10.1002/anie.200300610> (2004).
46. Yaghi, O. M., Ockwig, N. W., Chae, H. K., Eddaoudi, M. & Kim, J. Reticular synthesis and the design of new materials. www.nature.com/nature (2003).
47. Doty, F. P., Bauer, C. A., Skulan, A. J., Grant, P. G. & Allendorf, M. D. Scintillating metal-organic frameworks: A new class of radiation detection materials. *Advanced Materials* **21**, 95–101 (2009).
48. Wang, C. et al. Synergistic assembly of heavy metal clusters and luminescent organic bridging ligands in metal-organic frameworks for highly efficient X-ray scintillation. *J Am Chem Soc* **136**, 6171–6174 (2014).



SPARTE PROJECT

2.1 SPARTE project in detail

To sum up, when the nuclei of atoms are unstable, they become radioactive. It usually happens with isotopes that exist either naturally or as a result of human activity. Radionuclides are unstable and naturally emit ionizing radiations at a certain decay rate known as the half-life (which can range from ns to billions of years). These ionizing radiations are photons or particles such as X-rays, α and β particles, γ rays and so on. Ionizing radiations can interact with materials, causing free charges to form. Charges can be detected directly (using ionization chambers or germanium detectors) or transformed into visible photon emissions that can be detected using standard photodetectors. Scintillation is the latter detecting method. While detection systems for γ and X-rays are developed and commercially accessible, α and β particles are more difficult to detect due to their short mean free path through matter. This short mean free path greatly relies on the particle's energy; in the instance of β , it can range from some meters in water to some cm for higher energy particles, and it can range from some cm to a meter in air. Their detection becomes crucial when their energy is lowered since they must be virtually in touch with the sensor to be noticed. Beyond identifying the existence of radioactive materials, metrology requires quantifying the activity, which entails modelling the matter radiation, and reliable and widely deployable technology does not exist for most of the β -active crucial elements. By introducing highly porous scintillating aerogels and/or Metal-Organic Frameworks designed to drastically expand gas-matter interaction for effective detection by scintillation, the project SPARTE will execute and realize a radically unique radioactive gas detection and

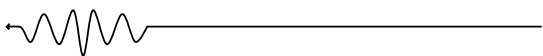


excellent sensitivity for metrology. As a result, Europe will take the lead in developing technologies to identify and monitor strategic radioactive pollutants. Thus, the project's goal will be to develop practical solid-based sensors that provide tight intermixing between the sensor and the analyte while combining efficiency and uniformity. A porous material built in a shape that fits the currently employed liquid container enables for the absorption of a considerable volume of gas, with the gas always near the active solid. The random porosity distribution, together with the usual penetration depth of the β particles and the sequential scattering paths, provides an isotropic behaviour that allows 4π detection geometry. This approach also provides a possible greater volume of detection, depending on the material and light detection system, boosting sensitivity, and may be utilized in a variety of devices such as the SPALAX system. Simple SPALAX upgrade devices, such as ionization chambers, already exist, but they work in the integrating regime, limiting system sensitivity, and they frequently employ pressurized methane as a gas carrier, implying an extra explosive danger. Aside from the potential for greatly better performance, this enabling technology might be widely used for on-site surveys of human activities in the production of manufactured radioisotopes and naturally occurring radionuclides. The approach will also be developed for specific isotopes such as ^3H and even ^{37}Ar , which will be the most difficult due to the low energy of its β -emission. This will significantly expand the range of measuring capabilities, not only for the National Metrology Institute and the development of new radioactive standards, but also for environmental laboratories participating in the activity survey. High specific areas and a 4π detection enable the development of a previously unknown reference detection system, and hence a way of calibration for noble radioactive gases with low concentration-activity down to the level of mBq/m^3 . It is critical for the CTBTO and currently does not exist since existing reference measurement methods are restricted to roughly $300 \text{ Bq}/\text{cm}^3$ for just select noble gas isotopes such as ^{85}Kr , ^{133}Xe , ^3H , and ^{127}Xe using Triple Compensated Length Proportional Counters (see Chapter 3). SPARTE's novel materials might potentially lead to a simpler reference measurement approach that could be applied in other national metrology institutions. The detection difficulty of a porous scintillator grows as the energy of the β particle lowers. The difficulty may therefore be readily



classified as follows, from "easiest" to "most difficult" to detect: ^{85}Kr , ^{133}Xe , ^3H , and ^{37}Ar . SPARTE will thus target the following four breakthrough objectives. While the current calibration methods are limited to 1 kBq/m^3 for ^{85}Kr and ^{133}Xe , the first target is to reach a detection sensitivity of mBq/m^3 and to propose a calibration method for low activity range (down to 1 Bq/m^3). The second target, based on the experience gain of the first one, is to achieve real time detection of ^3H with a significantly improved sensitivity in an easy deployable system. The most sensitive device in lab experiment uses liquid scintillation and achieve 2 kBq/m^3 after 1h of accumulation while ionisation chamber have a limit of 12.5 kBq/m^3 . The project aim is to combine real time and a sub- kBq/m^3 sensitivity. The concept can in addition be widely deployable for the ^3H and tritiated water vapour detection in air which would be an important breakthrough in this field. The third target is to develop real time on-site measurements as an alternative to current technologies which could be widely deployed considering their cost-effective aspects. Currently, very expensive detectors are used (see Chapter 3) and are specific to CTBTO. Simpler and cheaper systems could be advantageously deployed, such as ^{85}Kr survey next to Fukushima, or to nuclear reprocessing plants. The fourth target, which is the most challenging and risky, is to achieve the detection of ^{37}Ar . This isotope is strategic, because it is produced by the activation of calcium by high energy neutrons and has a relative long half-life time. It is thus a clear and good indicator of underground nuclear tests. We cannot reasonably propose quantified target, and even with a poor sensitivity, an on-site detector would be a significant step.

The material SPARTE is looking for has to combine a high specific surface to ensure an efficient interaction with the volume of gas to analyse, a significant scintillation yield ($>10\text{ photons/keV}$) to ensure a significant emission of photons, a fast response ($<100\text{ ns}$) in order to achieve efficient coincidence measurements. It will be transparent, with respect to the diffusion (translucent accepted) and also regarding the self-absorption, which is necessary to reach high metrology level as well as to improve some β/γ coincidence techniques. Additionally, the materials can be modified in such a way to be moulded to specific shapes in the range of a few cm^3 and in some cases can be obtained as flexible elastomeric composites easy adaptable for



specific uses. It will be non-hygroscopic, homogeneous and with a perfect reproducibility, which for metrology is a very important target. The targeted geometries are the current liquid scintillator vials while, for on-site detectors, the geometry is not defined (but in the range of cm^3) and depends on the achieved scintillating performances. In this perspective, SPARTE aims to design porous scintillating materials following two strategies:

1. the use of porous Metal-Organic Frameworks (MOFs), which intrinsically contain scintillation metal sites, in the form of single crystal, microcrystals or amorphous nanoparticles.
2. the use of monoliths of tailored geometry obtained by a supercritical drying of polymeric gels to generate hierarchically porous aerogels with a high content of scintillating material or by self-assembly of MOF precursors.

2.1.1 SPARTE Consortium

SPARTE includes experts from different fields in academia and from young high-tech SMEs, which are required to successfully address the main objectives. From material chemistry, physics, detection and metrology, SPARTE gathers the whole chain of knowledge and skills which are required to successfully address the main objectives and bring the developed components and method to the demonstrator level and potentially to the market. The participants to the project are listed above in alphabetical order:

CEA: The French Alternative Energies and Atomic Energy Commission is a key player in research, development and innovation in four main areas: defence and security, low carbon energies (nuclear and renewable energies), technological research for industry, fundamental research in the physical sciences and life sciences.

CTU: Czech Technical University in Prague is counted among the oldest technical universities in Europe and represents also one of the largest universities in the Czech Republic.

ICOHUP: spin-off aiming to develop competitive pollution measurement instruments.



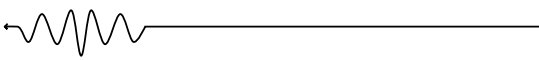
LIP: Lyon Ingénierie Projets, is owned and controlled by the Université Claude Bernard Lyon 1, and performs a mission for the University dedicated to research promotion and grant management.

NAF: Nano Active Film Srl was founded in 2010 as an academic Spin-Off of the University of Salerno operates in the sector of new materials based on polymer materials.

UCBL-ILM-LdC: University Claude Bernard Lyon 1 is a multidisciplinary university in the primary fields of physics, chemistry, technical and material sciences, life sciences, medicine and pharmacy. UCBL is involved through 2 of its major research units: The Institute of Light and Matter (ILM), which is concerned essentially with the study of matter and its physico-chemical properties, and The Chemistry Laboratory (LdC), which is a joint unit operated by the CNRS, the École Normale Supérieure of Lyon and Université Lyon 1.

UNIMIB-Department of Materials Science: The Department of Materials Science focuses its research activity in the field of functional materials. Over the years, also stimulated by the extraordinary growth of nanotechnologies worldwide, the Department has extended the research of bulk functional materials towards the nanosciences and their technological applications.

The project coordinator from UCBL-ILM has long-term expertise in scintillating materials, at the interface between material synthesis and detection systems, both on fundamental and applicative aspects, including transfer to the market since he is a co-founder of the spin-off company ICOHUP. CTU, UCBL-ENS, CEA-LCAE and UNIMIB combine experts in nanoparticles, synthesis of MOF nanoparticles to be integrated in porous, densified materials or single crystals. It includes all the required morphological and structural characterization expertise. CEA-LNHB has developed many reference measurement methods to produce radioactive standards. It also produces several experimental detection systems and electronics. It has now a new reference radioactive gases facility to produce atmosphere of radioactive noble gases from high activity sample and perform dilution in a wide range of activity concentration. This facility was developed to test and qualify new materials and measurement methods for the radioactive gases and is the only one in the world that can be used for all the gases. LNHB is the biggest metrology lab in the world for radioactivity (due to the fact it was built with the CEA) and has recognized experts in detection



and associated modelling to push the detection to the metrological level and share it with other metrology laboratories over the world. They are active member of the international board of metrology CIPM-MRA from BIPM (Bureau International des Poids et Mesures) by performing various comparison with different National Metrology Institute over the world. CEA-LNHB is working closely with CEA-LCAE with the aim to develop scintillator and detector techniques for the industries, one of the objectives of their direction from CEA in the field of research and technologies (CEA-Tech). The two laboratories of CEA have also experience in commercialization of detection systems or related technologies. Beyond the technological challenge, SPARTE project anticipates the market aspect and has 2 spin-off companies in the consortium. Nano Active Film (NAF) is a spin-off company from the University of Salerno with a strong expertise in the preparation and characterization of nanoporous polymeric materials, especially porous polymeric aerogels towards the market. ICOHUP aims to develop competitive pollution measurement instruments. Focused on radiation measurements, ICOHUP developed a specific knowledge for compact and connected instruments. In particular, ICOHUP has developed a g spectrometer 20 times cheaper than the market which allows wide uses in industrials networks. ICOHUP has also developed a pocket size energy compensated GM counter with dual calibration, both for telluric radioactivity and cosmic particles.

2.1.2 Consortium goals

The project is at an early stage of this technological field since no detection system achieving the targeted performances already exists. For one of the radioisotopes (^{37}Ar), it is not even detected, and another one (^3H) can be detected under some specific conditions and always out of metrological consideration, particularly for low activities. The scintillating porous material as a building block for β -emitter radioactive gas detection has not been previously considered. So far, no widely deployed technology exists because of the complexity, cost and performances currently achieved with other technologies. UCBL (and its Linked Third Party ENS-Lyon, and CEA have performed a proof of concept demonstrating the feasibility for ^{85}Kr detection, and this first result obtained on preliminary samples, allows to consider porosity as a solution of high potential towards the metrology of radioelement analysis as well as environmental survey of a selection of radiotracers. Regarding MOFs, UCBL-ILM and UNIMIB have started a work for the proof of concept, and the preliminary scintillating performances are

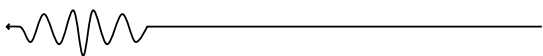


promising. The project is ambitious and visionary with the potential to revolutionize the metrology of gas radioactivity as well as the environmental and security survey regarding these components. The long-term vision on society includes widely deployed detectors either for CTBTO, but also for all nuclear activities. These points illustrate how ambitious, novel and foundational this concept and the related demonstrator, will be.

2.1.3 Work packages (WPs)

Through a tight integration of partners and exchanging team members, we ensure the best possible dovetailing of all competences involved. SPARTE is structured into four WPs, including a management/ exploitation/ dissemination WP responsible for smooth interaction and communication between the partners and three research-focused WPs.

WP1: the aim is to prepare aerogel type monolithic porous materials that result from supercritical drying (CO_2 , alcohol) of gel. The ideal situation is to avoid silica to reach a sensor made of a 100% active scintillating material. The required versatility to reach a controlled panel of performances is to develop the process for various materials showing different compromise of performances. The active starting material can be prepared following several approaches. Small, crystalized nanocrystals can be obtained using solvothermal methods. The proof of concepts has been demonstrated with $\text{Y}_3\text{Al}_5\text{O}_{12}:\text{Ce}^{3+}$ and GdF_3 nanocrystals (5-10nm) (ENS, UCBL LTP). Another method to prepare the aerogel “precursor” will involve a radiation technique, which is based on irradiation of aqueous solutions containing suitable precursors with ionizing radiation or non-ionizing (UV) radiation (CTU). The material formed by irradiation needs to be annealed at high temperature in order to obtain nanocrystals. The resulting nanomaterials are significantly larger (30-60 nm). CTU has developed a large-scale irradiator allowing to produce large quantities of precursors (more than 100g of scintillating nanocrystal in one batch), a requirement towards the objective of reproducibility of the sensor performance. A gel must be formed from these nanoparticles. Depending on the considered material, thermal treatment of the resulting material is required to reach the full crystallization and thus the optimum scintillating performances. Note that in both cases, the scintillating material based on doped inorganic crystals does not show significant self-absorption. They are in fact already used as large single crystal detectors.



WP2: These materials have nanometric porosity due to their intrinsic scaffolding. Their synthesis is highly challenging because it is necessary to balance the pore formation (governed by capillarity forces) and lattice formation (driven by the enthalpy for the frameworks formation). The MOFs as porous scintillating monoliths will be obtained along two strategies to minimize the risk. The first one performed by UNIMIB will be obtained by a self-assembly of dicarboxylic ligands and metal-cluster nodes. They are endowed with high surface areas in the 2000-3000 m²/g range and can host several gas-guest molecules. The synthesis conditions can be modulated in order to control the MOF crystalline size, from a few tens of nanometers to microns, and to tune the pore size. These properties will have the advantage of enhancing the adsorption efficiency and the fluorescence yield, thus maximizing the detection ability. The new scintillating MOFs will be further engineered by realizing “molecularly doped” crystals, in which a fraction of the original ligand dyes will be substituted by emitter molecules with similar steric hindrance and structural properties but with red shifted electronic energies and emission spectrum. The idea underpinning this concept is to exploit the fast migration of optical exciton created within the metal-organic framework by the ionizing radiation to reach the dopant chromophores. In such a way, this system will work as a photonic antenna able to emit at frequencies Stokes shifted with respect to the original luminescence, thus avoiding the self-absorption due to the high concentration of emitters in the MOF structure and therefore maximizing the out-coupling of the scintillation light produced, thus the overall detector sensitivity. MOFs will be incorporated in high porosity polymeric aerogels, or pressed into translucent pellet to prepare monoliths that can be handled for final aims. In order to maximize the transport properties of MOF/polymer composite aerogels, aerogels with nanoporous (or ultra-microporous according to IUPAC classification) crystalline phase based on syndiotactic polystyrene (s-PS) and poly(2,6-dimethyl-1,4-phenylene oxide) (PPO) will be prepared. The combination of a macroporous phase common of all aerogels and a nanoporous crystalline phase typical of s-PS and PPO polymers allows a high sorption capacity associated with a fast sorption kinetics of volatile molecules even at low activities. The second strategy (CEA) aims to directly grow large single crystals of MOF since large scale crystallinity with minimized edge defect guarantees high purity. Chemically wise, a focus will be made on MOFs based on classic scintillating molecules regarding the CEA extensive background on scintillation phenomenon. Nevertheless, the largest



crystals obtained so far are in the range of a few mm, while application requires monolith in the cm range. CEA is developing adaptable protocol for MOFs synthesis and crystal growth, which are unique in the fields.

WP3: MOF and aerogel structures will be characterized by X-ray diffraction experiments, surface area and gas adsorption measurements (N_2 , CO_2 , Xe and Ar adsorption isotherms), thermal analyses, electron microscopy. As for the optical and scintillating performances, the preliminary on-site tests will be performed on site to speed up the feedback process (when equipment are available) or at UCBL-ILM. When the composition will reach acceptable performances, a complete scintillation characterization with x-ray or gamma sources will be performed at UCBLILM for reliable comparison of performances and to reach optimal composition. Then measurements for benchmarking in “real use condition” will be performed with radioactive gas at CEA. It includes the use of the triple to double coincidence ratio (TDCR) technique with the functional sensors. For these benchmarking, CEA has developed a unique new laboratory facility to produce reference atmosphere in a gas chamber of all radioactive gases including standards. As for the reference measurement method, they will rely on the combination between Monte-Carlo simulation (CEA) and on the achieved performances of the porous materials.

WP4: gathers the scientific coordination of the project and the overall management of its administrative, financial, and legal aspects. Its main objective is to ensure smooth coordination and efficient project management thus contributing to the successful implementation of the project workplan. Based on its strong experience in the management of transnational and intersectoral large consortia in various fields, LIP will in this WP assist the coordinator and the consortium in the monitoring of the other work packages, the timely production of deliverables and achievement of milestones, in the overall reporting process and in the risk detection and mitigation. LIP will also support the definition and implementation of the communication, dissemination and exploitation strategy defined by the consortium in compliance with the rules and best practices governing the European-funded projects.

Now that the entire project has been explained, it is time to dig deeper in the gas detection systems and, in particular, to focus on WP3 tasks which are some of the fundamental bricks for a next generation gas detection devices.

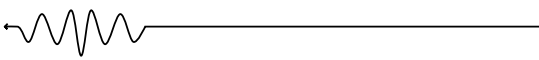


RADIOACTIVE GAS DETECTION SYSTEMS

The following paragraphs illustrate the actual state of the art for the detection of radioactive gases. The Swedish SAUNA system as well as the CEA SPALAX™ are described. Particular emphasis is given to the detector developed by SPARTE's WP3, the micro-TDCR, a new generation of detectors that will permit an on-site sampling and analysis.

3.1 Swedish Automatic Unit for Noble gas Acquisition (SAUNA)

The Sauna system is mainly devoted to radioxenon detection, and it is thus conceptualized as β - γ analyzer¹. A schematic of the full process is presented in Fig. 2.1². The sample is adsorbed on an Ag-ETS-10³ trap (an Ag coated porous material with a particular affinity with xenon) within the sampling oven (SOV) at an absolute pressure of 8 bar and at room temperature. The measured gas is passed via a coalescing filter, a pressure swing adsorption (PSA) module comprising two molecular sieve traps, and an extra molecular sieve (MS) trap before entering the Ag-ETS-10 trap to lower the CO₂ and H₂O content. The PSA unit can handle samples containing extremely high amounts of CO₂. The argon contained in the sample may be collected using the exhaust from the sampling trap. This portion of the sample will mostly comprise N₂, O₂, and Ar. During the sample phase of the operation, the gas can be collected and analysed by an argon detection/processing system. To prevent disrupting the SAUNA process by changing the pressures at the



exhaust, collection should employ an expandable container¹. The xenon sample is processed in the processing oven (POV) by transferring it to an active charcoal (AC) trap. By heating the trap, xenon is desorbed from the xenon adsorption trap in the sample oven. The transfer is aided by the evacuation of the trap and the application of a constant flow of nitrogen carrier gas. The carrier gas is utilized to help the transfer in all phases of the gas process except the PSA. Purification of xenon happens throughout the process by selectively transferring xenon and eliminating both CO₂ and radon¹. A circulation fan and a ventilation hatch were added to ensure rapid and uniform heating and cooling. Except for the two tiny ovens carrying the carbogenic molecular sieve (CMS) traps, all ovens have this configuration⁴. Before the sample is adsorbed onto the charcoal, the MS trap in the POV eliminates any leftover CO₂ and H₂O. This AC trap is substantially smaller than the SOV trap, allowing for more precise sample transmission.

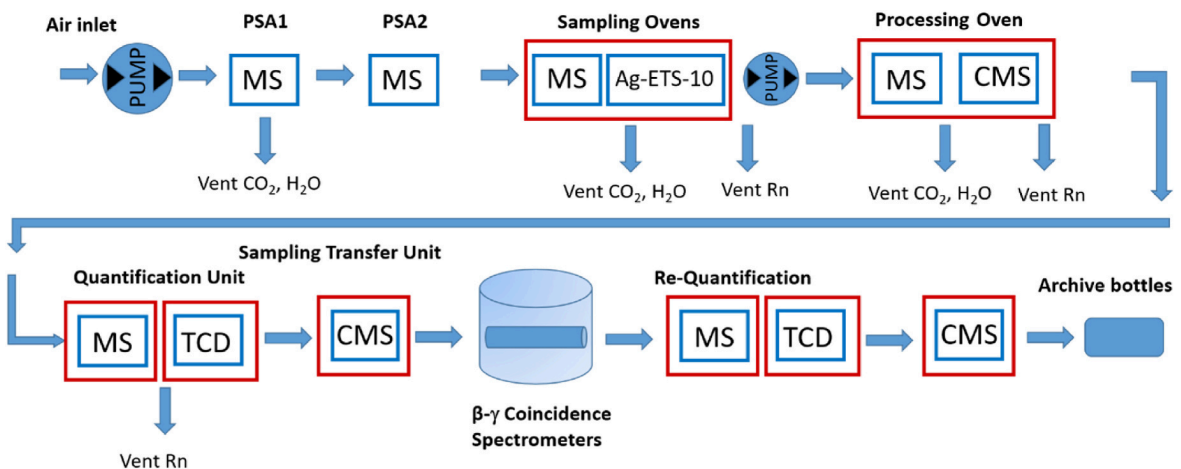


Fig. 2.1: Overview of the SAUNA III process. CO₂, H₂O and Rn are removed in most of the processing steps prior to the injection of the xenon sample into the detector. Different materials are used in the process to enrich xenon; several types of molecular sieve (MS), Ag-ETS-10 and carbogenic molecular sieve (CMS), and the amount of stable xenon is measured using a thermal conductivity detector (TCD). The red boxes indicates parts of the system that are heated during the process. The PSA and the re-quantification steps are added as compared to the SAUNA II process. Reproduced from Aldener, M. et al².

The sample is then further processed by heating the POV and transferring the xenon onto the quantification unit (QU) column using a carrier gas flow. The QU is a gas chromatograph that further purifies xenon, mostly from radon, and quantifies the stable xenon volume using a thermal conductivity detector (TCD). The pure xenon sample is put onto a tiny CMS trap in the sample transfer unit (STU) after the QU. This compact trap enables for



regulated injection into the detector cell's restricted volume, which is emptied prior to the transfer. A typical sample takes roughly 6 hours to process from the start of the procedure until the sample is put into the measurement cell and the acquisition measurement can begin¹. To assess the activity in the sample, the device employs four β - γ coincidence detectors⁵. The sample activity is determined using three separate measures. Two background measurements are performed prior to the sample measurement: the detector background, which is normally collected during system setup before the detector cells are exposed to radioactivity, and the gas background measurement, which is performed just before injecting the sample into the detector cell. The gas background measurement is used to account for any leftover activity in the detector from prior samples. Following the activity measurement, the measuring cell is evacuated, and the sample's stable xenon concentration is measured a second time using the same gas chromatograph that was used in the first quantification. The sample can then be preserved in one of 14 archive bottles. A minor CMS trap is used to inject into the archive bottle. The archival bottles have a capacity of 350 ml and are filled to an absolute pressure

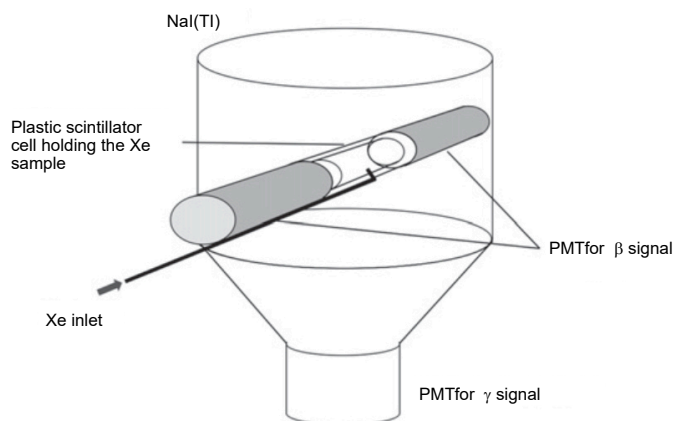
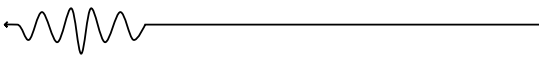


Fig. 2.2: Sauna system detectors. Reproduced from Blackber, L. et al⁸.

of roughly 0.5 bar. To simplify Chain of Custody of the sample, the archive bottles are labelled with RFID (radio frequency identification) tags. The device can handle sample amounts of up to 12 m³ before a substantial decline in xenon extraction yield occurs. The system has been adjusted to provide the greatest possible gas separation with very minimal cross contamination between samples (0.1%) and good radon separation. Larger samples can be analysed, but the process's tight gas separation setting will result in a lower yield. The major goal of this stringent separation setting is to provide a satisfactory separation even for samples with high concentrations of other gases, which can vary widely in soil gas. If excess water and carbon dioxide are not eliminated, they can disrupt the system's functioning. For example, too much CO₂ adsorbed in the sample oven will



alter the temperature profile during desorption owing to the de-gassing process. Radon is commonly found in high amounts in soil gas samples. If it is not removed, it will generate an interfering signal in the detector¹. Each gamma detector is made up of a 4.4 inch NaI cylinder connected to a single PMT. The beta detector, a plastic scintillator EJ-204, is coupled to two PMTs and is positioned in a 35 mm (diameter) hole through the NaI crystal's center. The beta cylinder has an interior capacity of 18 cm³ and a wall thickness of 1 mm^{6,7}. The adsorption of xenon in the detector cell plastic might leave a faint radioactive "memory" of the prior sample. This impact can be mitigated by taking a gas background measurement before each sample measurement. The beta cells were coated with Al₂O₃ to minimize the quantity of adsorbed xenon⁸. The memory effect in coated cells was investigated by introducing a high concentration of ¹³³Xe and monitoring the remaining activity after the cell was evacuated. The apparatus in its components is reported in Fig. 2.3. The minimum activity detected for xenon isotopes is < 1 mBq/m³, well below the minimum requirements request by the CTBTO⁹. This system is thus very efficient in revealing radioxenon isotopes but it is not optimized for other radioactive gases. Moreover, it is limited in its dimensions making it not suitable for on-site measurements. Indeed, the analysis is divided in two: sampling and testing.

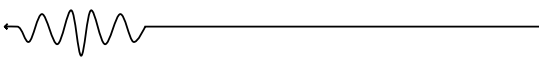


Fig. 2.3: A picture of the first SAUNA III system, with the two detector lead-shields in the back.

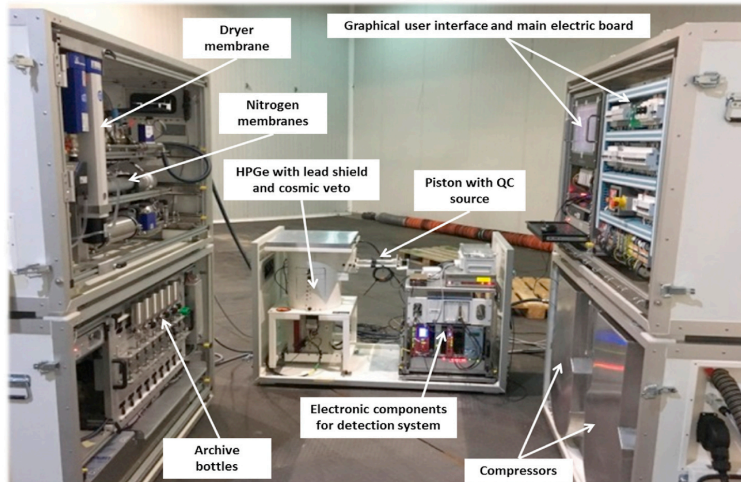
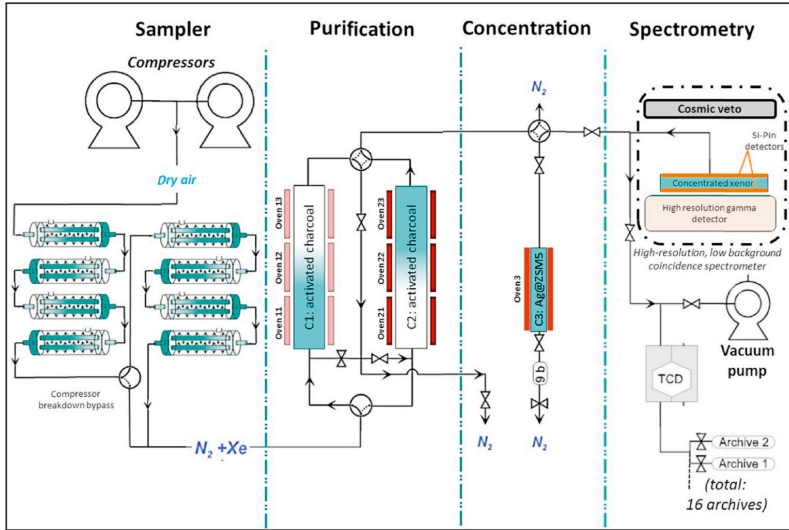


3.2 Système de Prélèvement Automatique en Ligne avec l'Analyse du Xénon (SPALAX™)

SPALAX™ idea and design have been fully explained in different works^{10,11}. Moreover, the first design of the SPALAX™ apparatus comes from the '90s with a design made by CEA. The new generation system is divided into five main units, each of which houses all of the necessary equipment: sample production is handled by three units (the sampling, purification, and concentration modules); sample analysis is handled by the detection unit; and system operation is handled by the control and command unit, which houses the programmable logic controller, graphical user interface, and electric board. The SPALAX-NG process's uniqueness in sample manufacturing is based largely on the pre-enrichment of xenon utilizing permeation membranes. This allows for self-production of the carrier gas (N_2) used in the purification and concentration processes. Two dry piston compressors work concurrently in the sample unit. One drier membrane and eight commercial nitrogen membranes are connected in series to remove water and generate pure nitrogen with a greater amount of xenon. The flow rate at the membrane exit is set to achieve a xenon concentration of around 2-3 parts per million by volume (ppmv)¹². The concentration unit contains an initial separation and concentration step on two sets of activated charcoal columns that operate alternately to separate radon and krypton from xenon and recover xenon at a greater concentration into N_2 . These gas fractions, including Xe, are delivered every 2 hours into the final concentration column, which includes a CEA-developed silver-exchanged zeolite^{13,14}. At the end of the cycle, the greatest quantity of N_2 is removed from this column by pushing it via a vacuum pump before transferring the sample through heat and expansion into the PIPSBox™ gas cell¹⁵. For a volume of 13 Ncm³, the final sample comprises roughly 35% Xe and 65% N_2 . The detecting unit is primarily based on the usage of a high-purity germanium detector (HPGe) and two silicon pin detectors mounted on the inner face of a gas cell (PIPSBox™) and put on top of the hyper-pure germanium crystal in coincidence mode¹¹. The entire device is protected by lead shielding and a plastic scintillator utilized as a cosmic veto on the top to lower the spectrometer's cosmic radiation background. This setup provides high resolution for γ /X-rays photons detection (HPGe) on 4096 channels with an energy range of 0-700 keV and a typical FWHM of 0.4 keV at 30 keV, as well as high resolution for β /conversion electron (CE) detection (PIPSBox™) on 1024 channels with an



a



b



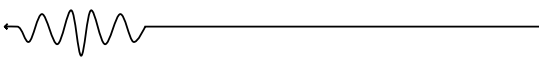
Fig. 2.4: a, Schematic of four major steps for production and analysis of atmospheric xenon sample by SPALAX-NG station (reproduced from Topin, S. et al.¹⁰). b, Left, germanium/silicon (PIPSBOX™) radioxenon detection setup devoted to the SPALAX™NG (without the shielding); middle/right: gas cell of 11.7 cm³ active volume equipped with two silicon detectors for electron detection and protected by a 600 μm carbon epoxy window entrance.



energy range of 0-900 keV and a typical FWHM of 12 keV at 129 keV. The HPGe detector is calibrated using a multi-gamma source in a custom designed shape that resembles the PIPSBox™ cell. By detecting a standard radioxenon gas, the PIPSBox™ detector is calibrated in conjunction with the HPGe¹¹. The HPGe/PIPSBOX™ spectrometer is a triple detection device working in coincidence, that is a system with three detectors that give the right signal when three events happen into the three different detectors¹¹. Also here, the sensitivity is under 1 mBq/m³ but this system is still limited to xenon analysis and its dimensions make it not suitable for quick transportation and use, as SAUNA.

3.3 micro-Triple to Double Coincidence Ratio (TDCR)

The limitation of systems like SPALAX™ and SAUNA resides in the fact that they are β/γ detectors, able to detect radionuclides which emits both of them, like xenon. On the other hand, the micro-TDCR system is a radioactive gas detector employing three photomultipliers working in coincidence, strictly used for the measurements of the activity of pure β emitters. It was developed by Dr. Benoit Sabot, one of the SPARTE project members, and collaborators in CEA. This device has been conceptualized for on-site measurement of environmental gas radioactivity. In a first time, it was designed for liquid scintillation counting (LSC) but, given the interest in having detector with higher efficiency and sensitivity, it is now employed in SPARTE as host system for the porous scintillators considered in Chapter 2. The triple-to-double coincidence ratio (TDCR) approach is a direct measurement method acknowledged as a fundamental measuring methodology for various radionuclides (pure β or α emitter, electron capture, etc.) by the worldwide metrology community. If the scintillating sources are created by precision weighting, the measurand is the activity of the scintillating source, which may be connected to the mass activity of the solution¹⁶. The radionuclides that can be calibrated using this approach are those for which the energy spectrum absorbed by the scintillating source following a radioactive decay may be estimated¹⁷. The use of three PMTs working in coincidence enables fast and precise measurements, avoiding spurious signals that are not related to the presence of a radionuclide. The functioning principles are illustrated in APPENDIX A while a detailed review on how TDCR devices work and the way in which they can measure and estimate the activity of a certain sample can be found in the article of R.



Broda¹⁶. Previous research by various national metrology institutes (NMIs), including the Commissariat à l'énergie Atomique (CEA) Laboratoire National Henri Becquerel (LNELNHB), has demonstrated the importance of having portable TDCR devices in order to perform on-site calibrations, particularly for the measurement of ^3H in nuclear power plants¹⁸. Moreover, in the case of sample of water containing ^{222}Rn where the half-life is greater (3.8232 d), source transportation, preparation, and sampling are highly difficult, necessitating on-site calibration of the liquid scintillation counters. In practice, transportation and restrictions governing the use of radioactive sources are becoming increasingly challenging¹⁹, thus having on-site capabilities, requiring the use of a transportable and reference device, becomes a valuable tool for metrology reasons. The design of the portable instrument was primarily oriented by the geometry of the selected PMTs in order to maximize the detection efficiency. To do so, the following characteristics were considered:

- The typical sample is placed in a 20 ml glass vial.
- Optimization of the distance between the sample and the PMTs.
- The addition of neutral density filters could be useful to vary the detection efficiency (avoiding saturation).
- The shape of the chamber was designed to optimize the collection of reflected light.
- The system is compact, and the power supply is included.
- The device is shielded to avoid any electromagnetic interference from the outside.
- The PMTs threshold must be easily adjustable to detect single photon.
- It must be possible to combine different detectors with the TDCR, like spectrometers.

The Hamamatsu H11934-203 PMTs²⁰ used in the micro-TDCR have a 30 mm square window and a depth of 32 mm. The sensitive area measures 23 mm



square. The ultra bialkali photocathode of these PMTs is paired with a diffusive quartz window. Because of the modest size of these PMTs, a compact device, as illustrated in Fig. 2.5, may be developed.

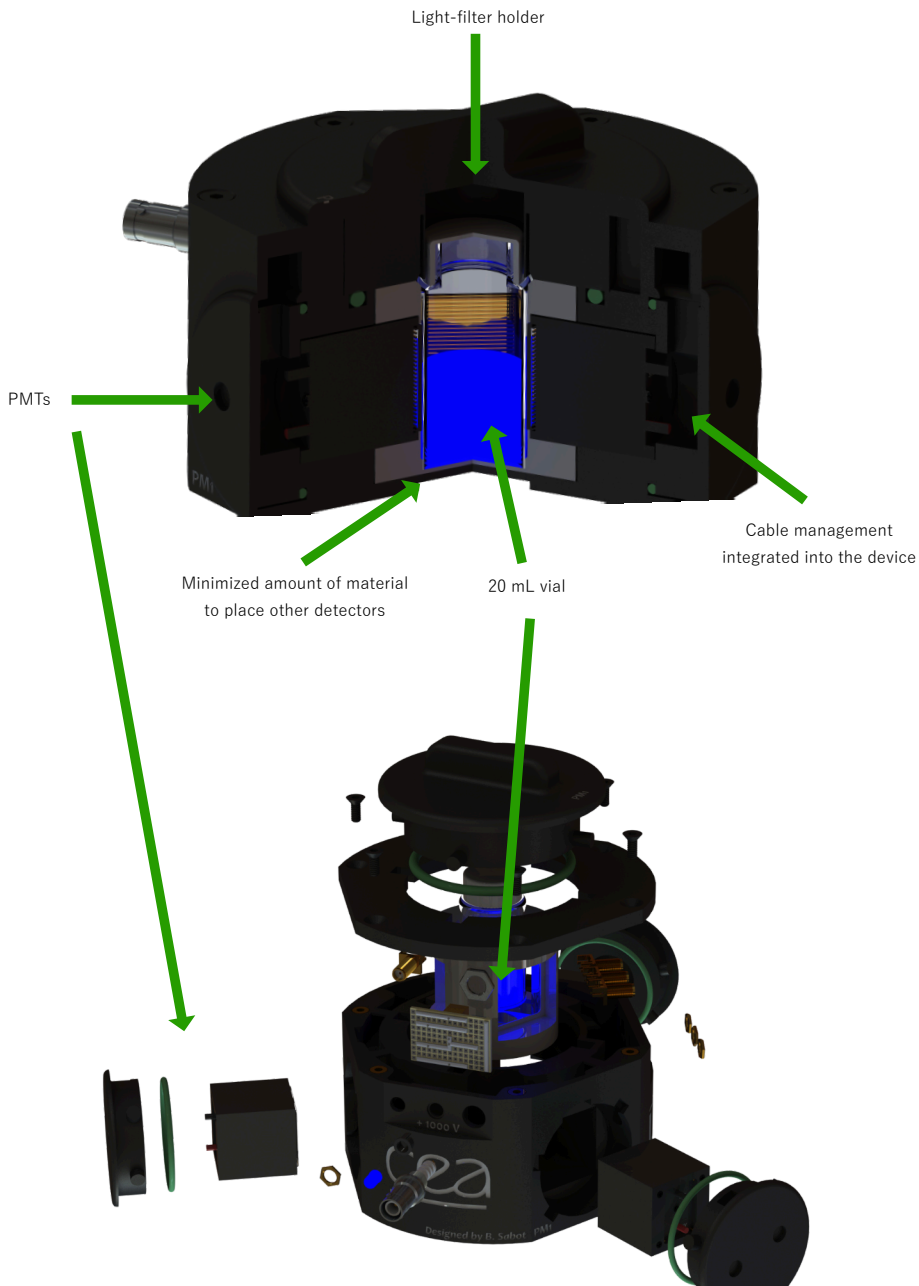
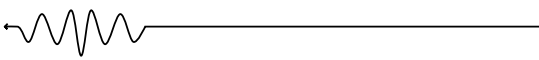


Fig. 2.5: exploded views of the micro-TDCR system in its main components. Reproduced from Sabot, B. et al¹⁷.



The optical chamber is produced in a single piece, which is only achievable with 3D printing. In this scenario, white PLA is employed, resulting in a surface that is not extremely reflective. PC-PTFE, which has a high reflective index, would have been ideal, but tests revealed that it was not possible to create an optical chamber with the mechanical and dimensional constraints required for its use. As a consequence, white PLA was employed, and surface reflectivity was improved utilizing additional surface treatments such as painting or aluminum or reflective foil coating. A little cylindrical cut-out on the bottom of the optical chamber has been built to guarantee that the vial is always positioned in the same way. The radius of the cut-out is only slightly bigger than the size of a typical vial, reducing the possibility of the vial moving inside the chamber. One disadvantage is that a portion of the vial's bottom is not immediately visible to the PMTs, which may result in some little light loss. The optical chamber's form was then optimized by treating its surface as a perfect mirror. Various geometries were explored between the PMTs while the top and lower ends were adjusted to produce a surface sloped at 45° . To focus photons on the PMT windows, triangular,

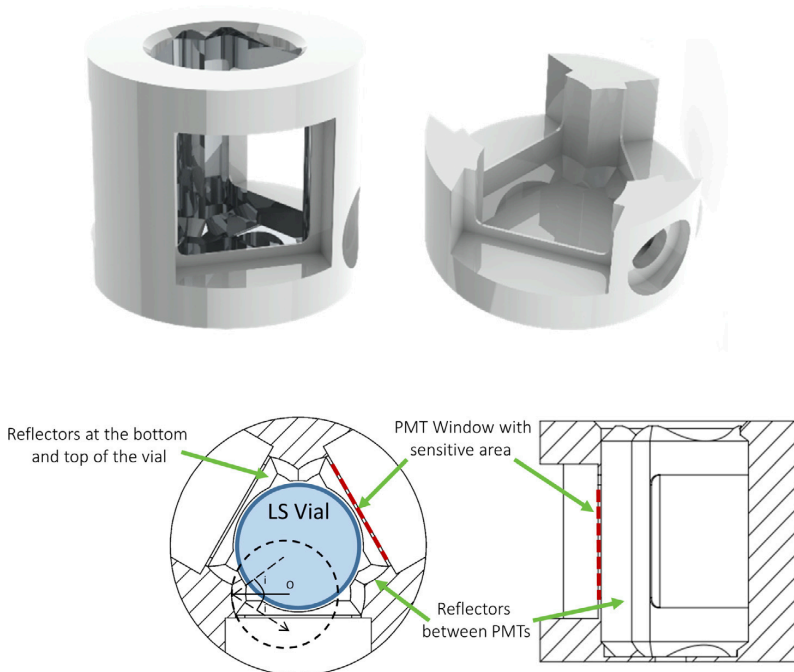


Fig. 2.6: 3D optical chamber modeling of the micro-TDCR system (top) and cross section of the optical chamber (bottom). Reproduced from Sabot, B. et al¹⁷.

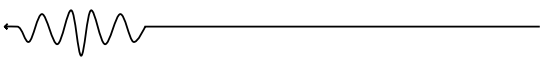


cylindrical, and flat spaces between PMTs were less effective than two concave portions.

Fig. 2.7 depicts the entire micro-TDCR in its case. The power supply for each device are produced locally, with +1000 V for the micro-TDCR and 1 mA for each. The three PMTs are powered by the same power sources, and a voltage divider built into the TDCR device ensures that each PMT receives the same voltage. Because the PMTs were not chosen, their efficiencies are not comparable, but it was decided to supply them with the same voltage and perform an asymmetry correction during the measurement analysis. A nanoTDCR module is used for signal processing. This module was created concurrently for portable devices and tested with the TDCR system. The nanoTDCR has several advantages, including the ability to run four acquisitions in parallel — with two different user-selectable coincidence windows (CW) and two different user-selectable base dead-time (DT) durations. A single use of this system yields to four measurements at once (2 CW and 2 DT).



Fig. 2.7: The whole set of components, including locally-made high voltage supply, can be easily handled and connected to a portable computer. Reproduced from Sabot, B. et al¹⁷.



3.4 References

1. Aldener, M. et al. SAUNA field - A sensitive system for analysis of radioxenon in soil gas samples. *J Environ Radioact* **240**, (2021).
2. Aldener, M., Axelsson, A., Fritioff, T., Kastlander, J. & Ringbom, A. SAUNA III - The next generation noble gas system for verification of nuclear explosions. *J Environ Radioact* **262**, (2023).
3. Kuznicki, S. M. et al. Xenon adsorption on modified ETS-10. *Journal of Physical Chemistry C* **111**, 1560–1562 (2007).
4. Aldener, M. et al. Results from a 6-month acceptance test of the SAUNA III prototype at FOI.
5. Ringbom, A., Larson, T., Axelsson, A., Elmgren, K. & Johansson, C. SAUNA - A system for automatic sampling, processing, and analysis of radioactive xenon. *Nucl Instrum Methods Phys Res A* **508**, 542–553 (2003).
6. Axelsson, A. SAUNA System Beta-Gamma Detector Calibration Stability Monitoring and Correction. (2017).
7. Ringbom, A. & Axelsson, A. A new method for analysis of beta-gamma radioxenon spectra. *Applied Radiation and Isotopes* **156**, (2020).
8. Bläckberg, L. et al. Memory effect, resolution, and efficiency measurements of an Al₂O₃ coated plastic scintillator used for radioxenon detection. *Nucl Instrum Methods Phys Res A* **714**, 128–135 (2013).
9. Comprehensive Nuclear-Test-Ban Treaty Organization (CTBTO, 2022); <https://www.ctbto.org/>.
10. Topin, S. et al. SPALAX new generation: New process design for a more efficient xenon production system for the CTBT noble gas network. *J Environ Radioact* **149**, 43–50 (2015).
11. Le Petit, G. et al. Spalax™ new generation: A sensitive and selective noble gas system for nuclear explosion monitoring. *Applied Radiation and Isotopes* **103**, 102–114 (2015).

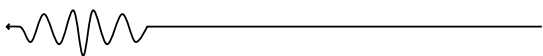


12. Topin, S. et al. 6 months of radioxenon detection in western Europe with the SPALAX-New generation system - Part1: Metrological capabilities. *J Environ Radioact* **225**, (2020).
13. Monpezat, A. et al. Migration and Growth of Silver Nanoparticles in Zeolite Socony Mobil 5 (ZSM-5) Observed by Environmental Electron Microscopy: Implications for Heterogeneous Catalysis. *ACS Appl Nano Mater* **2**, 6452–6461 (2019).
14. Deliere, L. et al. Role of silver nanoparticles in enhanced xenon adsorption using silver-loaded zeolites. *Journal of Physical Chemistry C* **118**, 25032–25040 (2014).
15. Sobel. Characterization of PIPS Detectors for Measurement of Radioxenon.
16. Broda, R. A review of the triple-to-double coincidence ratio (TDCR) method for standardizing radionuclides. *Applied Radiation and Isotopes* **58**, 585–594 (2003).
17. Sabot, B., Dutsov, C., Cassette, P. & Mitev, K. Performance of portable TDCR systems developed at LNE-LNHB. *Nucl Instrum Methods Phys Res A* **1034**, (2022).
18. Merelli, D., Annual IEEE Computer Conference, International Conference on Advancements in Nuclear Instrumentation, M. M. and T. A. 3 2013. 06. 23-27 M. & ANIMMA 3 2013.06.23-27 Marseille. 3rd International Conference on Advancements in Nuclear Instrumentation, Measurement Methods and Their Applications (ANIMMA), 2013 23-27 June 2013, Marseille, France; conference proceedings.
19. L, M. DE & Mer, D. LA. Décrets, arrêtés, circulaires TEXTES GÉNÉRAUX. <http://www.legifrance.gouv.fr>.
20. Hamamatsu. Hamamatsu, Photomultiplier Tubes R11265U and H11934 Series, Hamamatsu photonics, 2019,. https://www.hamamatsu.com/content/dam/hamamatsu-photonics/sites/documents/99_SALES_LIBRARY/etd/R11265U_H11934_TPMH1336E.pdf www.hamamatsu.com.



EFFICIENT RADIOACTIVE GAS DETECTION BY SCINTILLATING METAL-ORGANIC FRAMEWORKS

Metal-organic frameworks, or MOFs, have developed as a broad family of crystalline materials with ultrahigh porosity (up to 90% free volume) and massive interior surface areas exceeding 5000 m²/g. These properties, along with the extraordinary degree of variability for both organic and inorganic components of their structures, make MOFs appealing for potential applications in clean energy, most notably as storage media for gases such as hydrogen and methane, and as high-capacity adsorbents to meet various separation needs. Membranes, thin-film devices, catalysis, and biological imaging are among the other applications that are gaining traction¹. In particular, MOFs are an extension of the class of coordinated network materials. MOFs are made up of two major parts: an inorganic metal cluster (also known as a secondary-building unit or SBU) and an organic molecule known as a linker. As a result, the materials are sometimes referred to as hybrid organic-inorganic materials². Organic units are commonly monovalent, divalent, trivalent, or tetravalent ligands³. The structure and hence characteristics of the MOF are determined by the metal and linker used. The coordination preference of the metal, for example, determines the size and form of pores by defining how many ligands may bind to the metal and in which orientation. Interestingly, organic linkers could be also dyes/chromophores opening the way to thousands of combinations and applications. The earliest reports of luminescence that we are aware of, in which the structure was referred to as a "MOF," occurred in 2002. Since then, more than 500 studies have been published reporting light emission by MOFs, as well as a few reviews covering specific features of MOF luminous



characteristics. Although not always fully defined, it is noticeable that fluorescence, phosphorescence, and scintillation have all been recorded. Indeed, the hybrid nature of MOF materials, which include both an organic ligand and a metal ion inside a (usually) porous structure, allows for a wide range of emissive phenomena present in few other groups of materials⁴. There are several examples of fluorescent linkers. Organic linkers, particularly those with π -conjugated backbones, have negligible spin-orbit coupling, hence the symmetry of the singlet ground and excited states determines the selection principles. As a result, the most intense emission (fluorescence) is generally from the lowest excited singlet state to the singlet ground state. As anticipated before, scintillation is one of the fields in which MOFs can emerge. Indeed, the interplay between the two components of MOFs is striking: the fluorescent organic linkers that can scintillate by themselves and the metal cluster nodes that, being typically heavy and so with high Z , can stop ionizing radiation very efficiently. Thus, the MOF architecture is really beneficial for the generation of free charges upon interaction with ionizing radiation that can be then readily collected by the fluorescent organic linkers resulting in visible light emission. One of the first examples of scintillating MOFs comes from the expertise of prof. Allendorf and co-workers. They presented two different MOFs architecture, based on Zinc metal clusters as nodes and stilbene dicarboxylate as emitting ligand, able to well detect both α and β particles^{5,6}. Since this first discovery, several are the geometries discovered with different ligands involved and with different applications, from imaging to detection. And this brings us to the main topic of this writing. Following the pioneering work of Allendorf, here at the University of Milano-Bicocca we developed, synthesized and studied a new kind of MOF, specifically engineered for the field of ionizing radiation detection and, more in detail, for the detection of pure β emitting gases thanks to the material's high degree of porosity.

To sum up, to be controlled as pathogenic agents, radioactive diagnostic agents, or nuclear activity indicators, natural and anthropogenic gas radionuclides such as radon, xenon, hydrogen, and krypton isotopes must be monitored. Modern detectors based on liquid scintillators are hard to prepare and have limited gas solubility, which affects measurement accuracy. The fundamental difficulty is to discover solid scintillating materials that can concentrate radioactive gases while also creating visible light with great



sensitivity. These requirements can be accomplished because to the high porosity of metal-organic frameworks (MOFs) and the usage of scintillating building blocks. We show that a hafnium-based MOF with dicarboxy-9,10-diphenylanthracene as a scintillating conjugated ligand may detect gas radionuclides. Fast scintillation, a fluorescence yield of 40%, and accessible porosity appropriate for hosting noble gas atoms and ions are all characteristics of metal-organic frameworks. The adsorption and detection of ^{85}Kr , ^{222}Rn , and ^3H radionuclides are investigated using a newly constructed apparatus based on a temporal coincidence approach. Metal-organic framework crystalline powder displayed superior sensitivity, with a linear response down to a radioactivity value of less than 1 kBq/m^3 for ^{85}Kr , outperforming commercial devices. These findings support the application of scintillating porous MOFs in the fabrication of sensitive detectors for natural and anthropogenic radionuclides. In Fig. 4.1 a sketch of the Hf-DPA MOF and the working principle are presented.

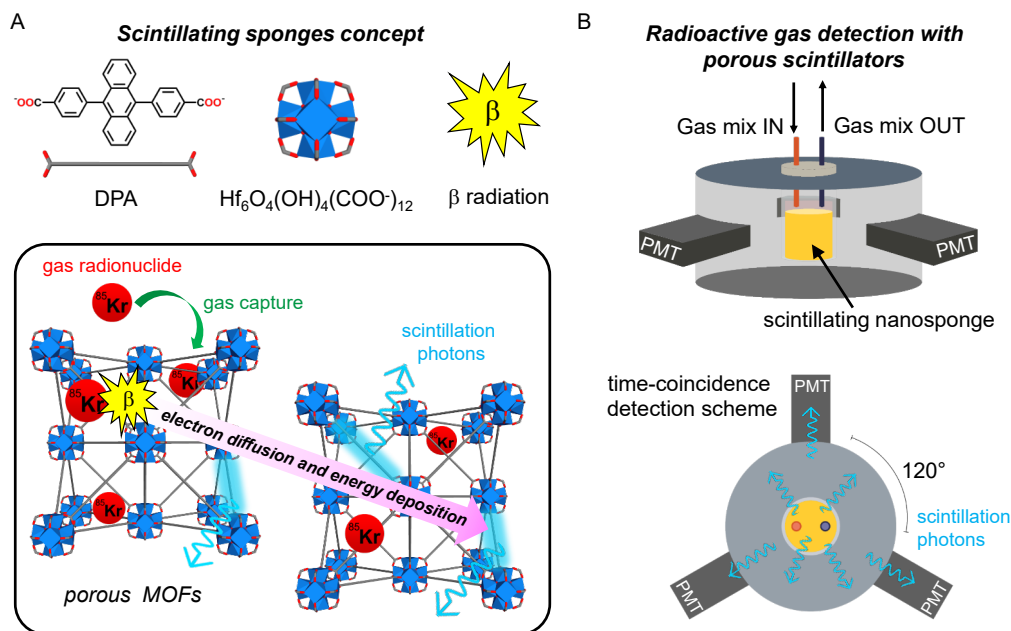


Fig. 4.1: Time-coincidence-based detector for radionuclides gases exploiting porous scintillators. a, Schematic representation of the scintillation mechanism inside fluorescent hafnium-based MOFs. The porous frameworks can uptake radioactive gaseous species through physical adsorption and concentrate them inside the pores. The decay process produces β -particles that can effectively interact with the porous particles during their diffusion and thermalization, triggering a sensitized scintillation process. The ligand and metal node that constitutes Hf-DPA, as well as the β -radiation emitted by radionuclides, are shown at the top. b, Sketch of the triple coincidence system designed to reveal radioactive gases by exploiting a porous scintillator.

4.1 Synthesis and analysis of hafnium-based MOFs

This paragraph is fully dedicated to the synthesis and basic characterization of the two fundamental elements of the MOF architecture studied: the hafnium oxide cluster nodes and the dicarboxy-9,10-diphenylanthracene scintillating ligand. In general, Hafnium-based MOFs containing luminescent DPA ligands (Hf-DPA) were synthesized using a solvothermal synthesis^{6,7} optimized to produce octahedral crystals with a cubic crystal structure 385 nm in diameter—at which size the emission properties are best—in highly reproducible batches ranging from a few tens of milligrams to 200 mg⁸.

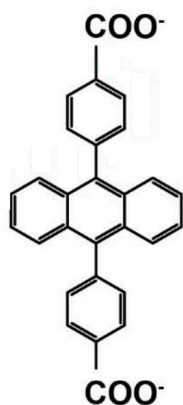


Fig. 4.1: 9,10-bis(4-carboxyphenyl)anthracene ligand.

4.1.1 9,10-bis(4-carboxyphenyl)anthracene ligand

9,10-bis(4-carboxyphenyl)anthracene (DPA) was synthesized using a Suzuki coupling with a modified procedure⁹. Briefly, 9,10-dibromoanthracene (1 g, 2.98 mmol) and 4(methoxycarbonyl)phenylboronic acid (1.18 g, 6.55 mmol) were dispersed in a 1:1 acetonitrile/water mixture (20 mL each) in a Schlenk tube. Nitrogen was bubbled for 1 hour to remove the oxygen from the reaction vessel. Potassium carbonate (2.89 g, 20.9 mmol) and Pd(PPh₃)₂Cl₂ (0.25 g, 0.36 mmol) were added and the reaction was stirred and heated at 100°C for 96 hours. The reaction was allowed to cool to room temperature and rotary dried under vacuum. The product was extracted with chloroform, dried over anhydrous sodium sulphate, filtered and rotary dried under vacuum. The yellow

solid was purified by column chromatography using chloroform as eluent. A yellowish crystalline solid was recovered after rotary evaporation and was dried under high vacuum to obtain dimethyl 4,4'-(anthracene-9,10-diyl)dibenzoate. Then, the yellow solid (1g, 2.24 mmol) was dispersed in a mixture of THF (90 mL), ethanol (30 mL) and deionized water (30 mL) and potassium hydroxide (1.56 g, 27.8 mmol) was added. The mixture was stirred and heated at 66°C for 24 hours. The completion of the reaction was assessed by TLC analysis using chloroform as eluent. Then, the mixture was allowed to cool to room temperature and concentrated HCl was added until pH ~ 1. The organic solvent was removed by rotary evaporation and the precipitate was collected by filtration and washed with deionized water. The solid was dried under vacuum and recrystallized from THF to obtain 9,10-bis(4-carboxyphenyl)anthracene⁸. In Fig. 4.3 ¹H liquid NMR of 9,10-bis(4-



carboxyphenyl)anthracene is showed to account for the purity of the obtained product. Moreover, in Fig 4.4 it is reported optical microscopy mages of crystal of 9,10-bis(4-carboxyphenyl)anthracene under sunlight and under 365 nm UV light.

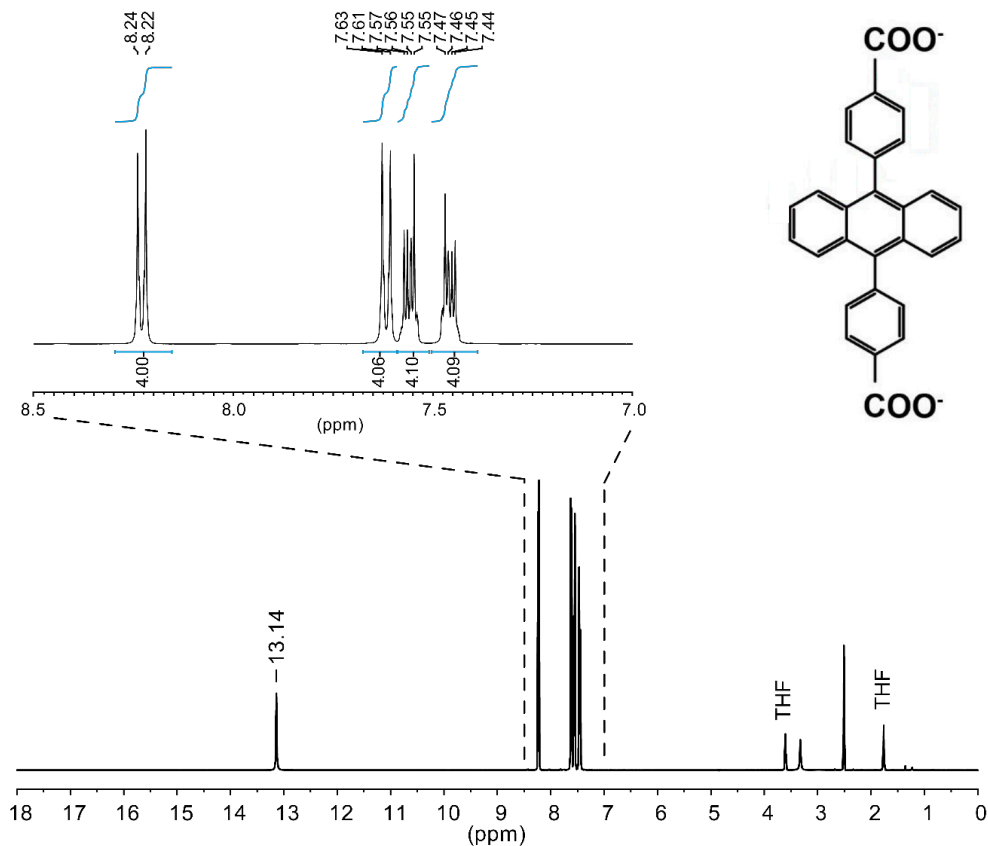


Fig 4.3: ^1H liquid NMR of 9,10-bis(4-carboxyphenyl)anthracene.

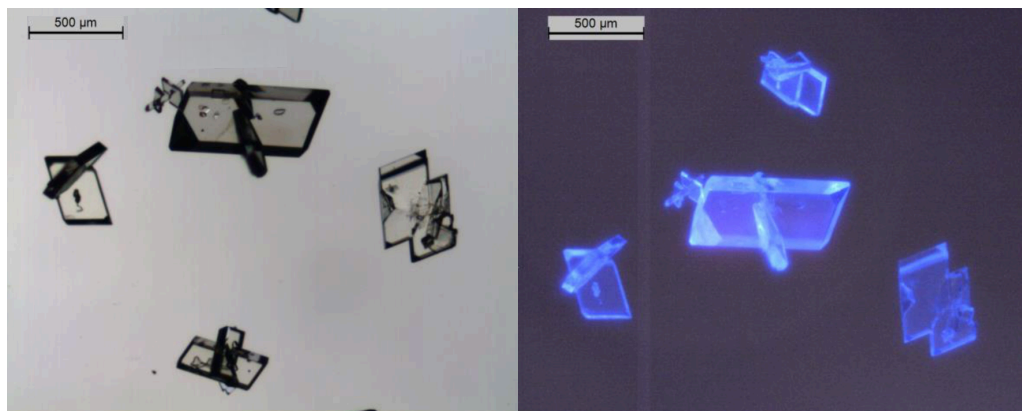


Fig 4.4: Optical microscopy images of crystals of 9,10-bis(4-carboxyphenyl)anthracene under sunlight (left) and UV light (365 nm, right).

4.1.2 Hf-DPA MOFs

MOF crystal growth was controlled by an increasing amount of modulator (formic acid). The screening reaction was performed on a small scale of tens of milligram. 9,10-bis(4-carboxyphenyl)anthracene (10.44 mg, 0.025 mmol) and HfCl_4 (8.0 mg; 0.025 mmol) were added to a 12 mL glass vials. Dry DMF (2.5 mL) and the proper amount of formic acid was added. The mixture was sonicated for 60 seconds to produce a homogeneous dispersion and the vials were heated in a preheated oven at 120 °C for 22 hours. Then, the vials were removed from the oven and cooled down to RT. The yellowish solid was filtered on a 0.2 μm PTFE membrane and washed with DMF (3 x 10 mL) and then with CHCl_3 (3 x 10 mL). The powder was recovered and dried at 120 °C under high vacuum before further analysis. In this way it was possible to obtain octahedral crystals with a cubic crystal structure and 385 nm in diameter. Notably, different sizes of Hf-DPA MOFs can be obtained following the above synthetic pathway and changing the amount of formic acid used as modulator⁸.

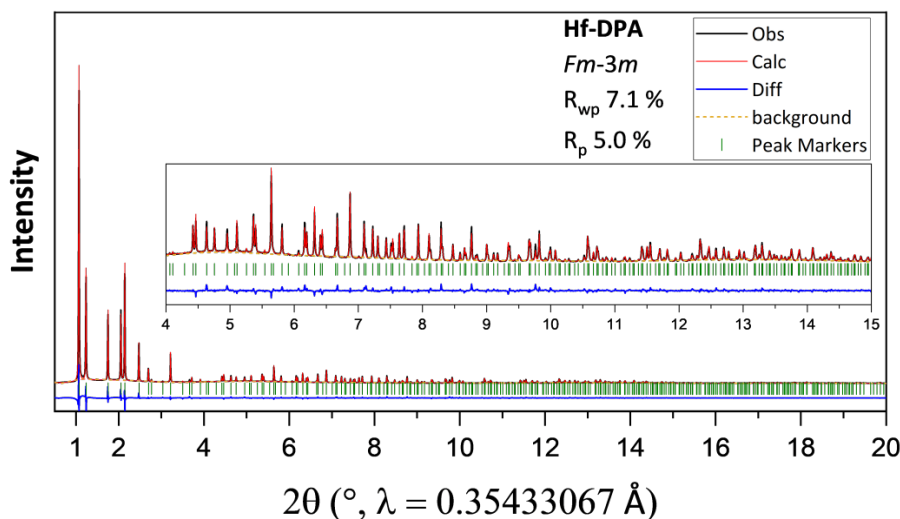


Fig. 4.5: the Rietveld refinement plot of synchrotron-source PXRD pattern of activated Hf-DPA collected at RT. Data were collected at the ESRF ID22 beamline by synchrotron radiation at 0.35433 Å. The structure was solved by Rietveld refinement combined with PW-DFT.

The crystal structure was solved by Rietveld refinement combined with PW-DFT of synchrotron-source PXRD. Hf-DPA crystals display a cubic crystal structure (space group $Fm-3m$) with fcu topology comprising connected octahedral and tetrahedral cavities (10.2 Å and 17 Å diameter fitted spheres, respectively). These cavities are connected by triangular windows through



which a sphere of 5.3 Å in diameter can pass, thus yielding highly connected three-dimensional pores. The total available pore volume corresponds to 70%, as explored by a sphere of 1.82 Å radius. The Hf-DPA MOFs has been reproduced in different batches with an optimum agreement as it is showed by the XRD patterns in Fig. 4.6. Thus, from the data obtained from XRD patterns, it was possible to reconstruct the structure of Hf-DPAs MOFs in $Fm-3m$ space group. In Fig. 4.7 is showed the primitive cell representation of the Hf-DPA structure with best fitted spheres included in the structure to highlight the void volumes. Representation of the connectivity between the nodes to highlight the tetragonal and octahedral regions is also underlined.

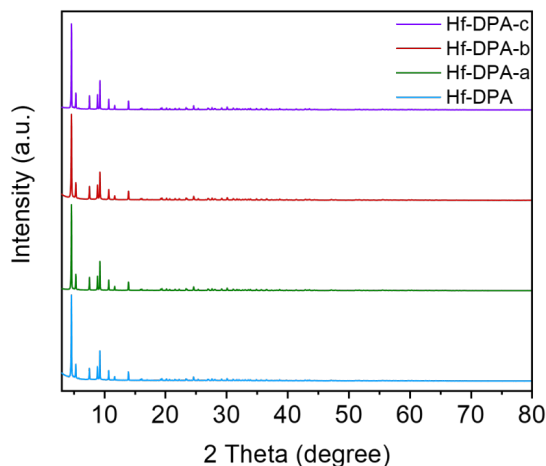


Fig. 4.6: Powder x-ray diffraction patterns of Hf-DPA (light blue), Hf-DPA-a (green), Hf-DPA-b (red) and Hf-DPA-c (purple) collected on a Rigaku Smartlab diffractometer using Cu K α radiation.

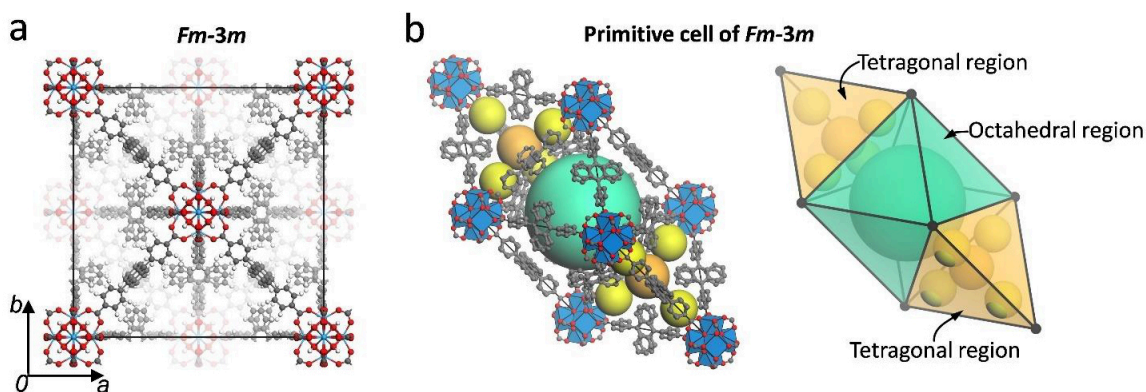


Fig. 4.7: a, structure of Hf-DPA MOFs in the $Fm-3m$ space group as refined by powder-XRD data. B, the primitive cell of Hf-DPA MOFs displaying tetragonal and octahedral cavities.

In order to study the size distribution Hf-DPAs and to better investigate on their crystalline structure, Scanning Electron Microscopy (SEM) images are reported in Fig. 4.8. The particle size was evaluated using more than 200 particles with software ImageJ. The data were fitted with a gaussian distribution resulting in an average size of 385 nm. The obtained Hf-DPAs MOFs were then analyzed by Energy-Dispersive Spectroscopy (EDS) means

that enabled the compositional analysis of Hf-DPA. The sample was deposited on a graphite stab and coated with graphite to increase the conductivity before EDS analysis.

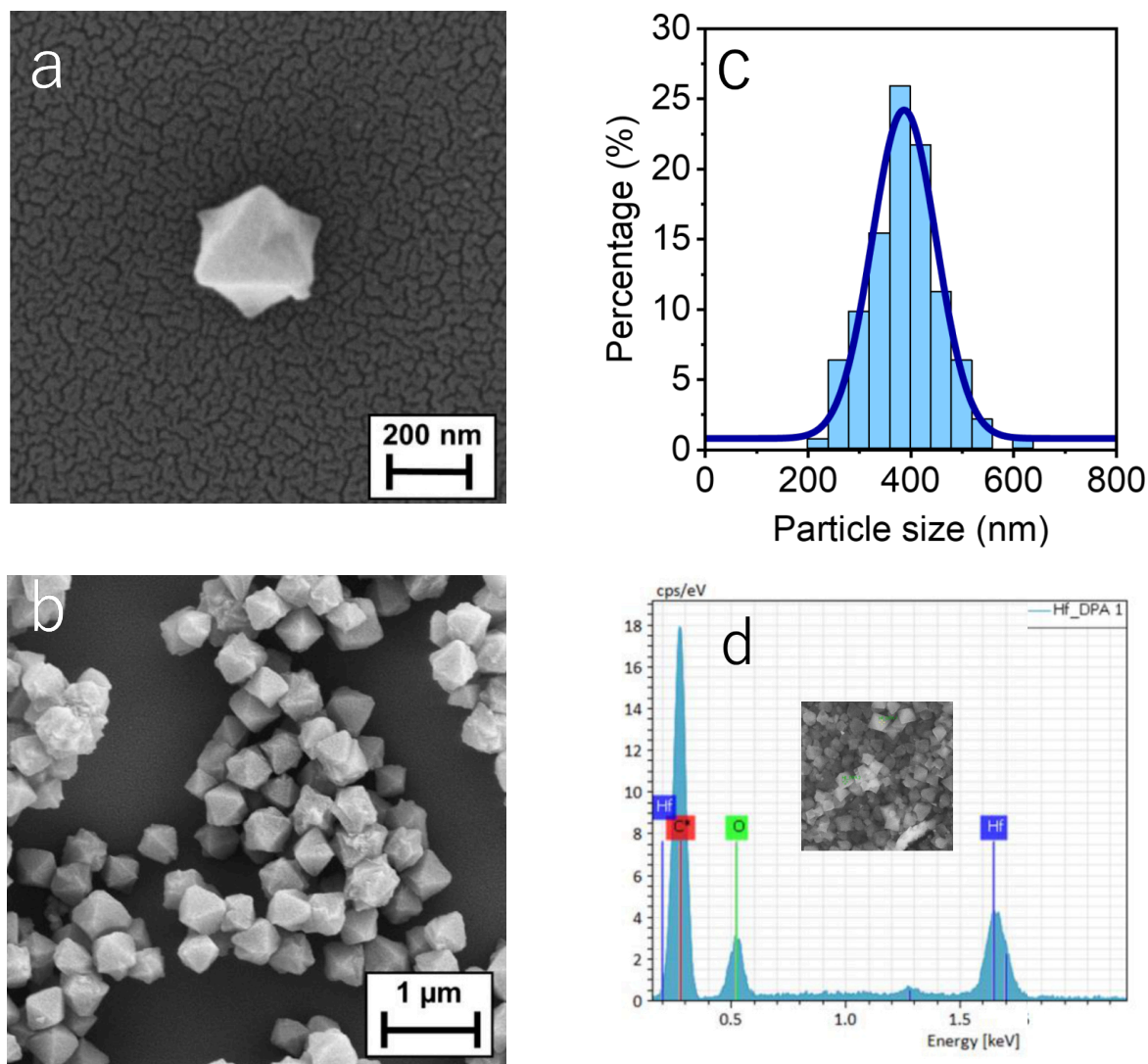


Fig. 4.8: a,b, Scanning electron microscopy (SEM) images of Hf-DPA MOFs at different magnification. Hf-DPA MOF crystals were casted on silicon surface and sputtered with gold before image acquisition. c, Particle size distribution of Hf-DPA nanocrystals calculated from SEM images. The particle size was evaluated using more than 200 particles with software ImageJ. The data were fitted with a gaussian distribution (blue line). d, Energy-Dispersive Spectroscopy (EDS) means that enabled the compositional analysis of Hf-DPA. The sample was deposited on a graphite stab and coated with graphite to increase the conductivity.



4.2 Gas adsorption analysis of Hf-DPA MOFs

The major concern when dealing with porous materials is the need to understand their internal structure, and, in particular, to quantify the extension of their internal surface. Acting in this way it is possible to study their porosity and gas adsorption capabilities. Thus, for Hf-DPA MOFs low-temperature gas adsorption isotherms show the microporous character of Hf-DPA as well as the adsorption of noble gases like argon and krypton. At ambient temperature, the argon and krypton adsorption isotherms were also measured, confirming gas diffusion inside the cavities under pressure and temperature circumstances similar to the operational situation of radioactive gas detection. In this context, hyperpolarized ^{129}Xe NMR measurements offer direct detection of noble gas diffusion through the pores of the Hf-DPA, even in competition with other gaseous species and under flow circumstances^{7,10-14}. Interestingly, all the gas used to test the Hf-DPA MOFs adsorption capability are also key target for the SPARTE project (Chapter 2). In Fig. 4.9 it is possible to appreciate that the free space inside the MOFs primitive cell is well fitted to host several gases of interest.

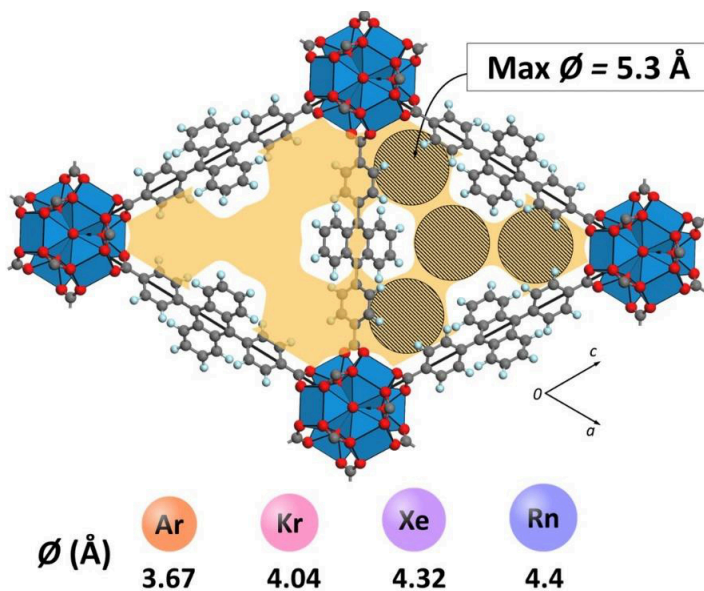


Fig. 4.9: The yellow cross-sectional area of the Hf-DPA triangular windows was mapped using a probe radius of 1.2 nm. The grey circles represent the largest diameter of sphere that can pass through the cross-section. The Van der Waals diameters of the noble gases from Argon to Radon are presented below. Gas molecule radii are consistent with pore size and may freely diffuse through the Hf-DPA structure.

4.2.1 Isotherms analysis

Adsorption isotherms for N_2 , Ar, and Kr obtained at 77 K and room temperature demonstrated the open porosity and pore accessibility of Hf-DPA to gases. According to the Langmuir and BET models, the N_2 adsorption isotherm obtained at 77 K reveals an uptake as high as 29.7 mmol g^{-1} and surface areas of $2887 \text{ m}^2 \text{ g}^{-1}$ and $2613 \text{ m}^2 \text{ g}^{-1}$, respectively.

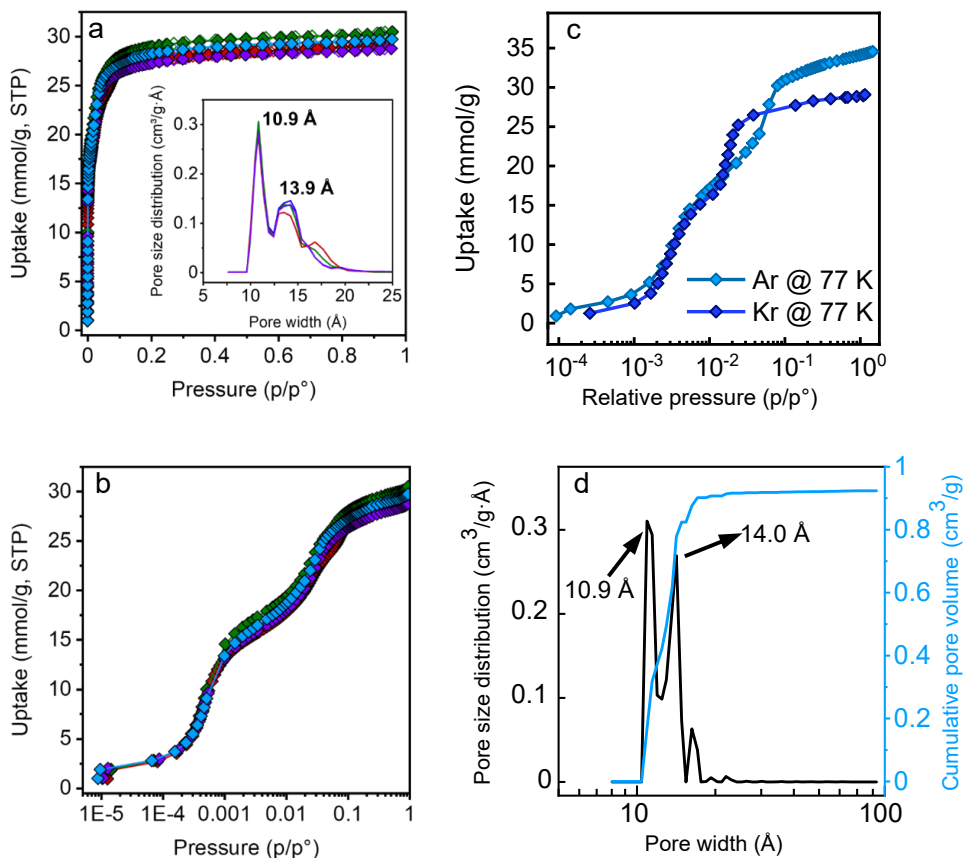


Fig. 4.10: a, b, N_2 adsorption isotherms collected at 77 K for 4 different batches of Hf-based MOF with the x-axis displayed in linear (left) and logarithmic scales (right). Inset: comparison of the differential pore size distributions calculated from the adsorption isotherms using non-local density functional theory and carbon slit pore model. Hf-DPA (light blue), Hf-DPA-a (green), Hf-DPA-b (red) and Hf-DPA-c (purple). c, Argon (light blue) and krypton (dark blue) adsorption isotherms collected at 77 K. d, pore size distribution calculated from argon adsorption isotherm using the non-local density functional theory method.

Notably, noble gases like Ar and Kr are also successfully adsorbed. The adsorption isotherms at low partial pressure and 77 K show sequential gas adsorption at distinct pressures consistent with the filling of the smaller tetrahedral cavity, followed by the larger octahedral cavity, with mean pore



sizes of 10.9 Å and 14.0 Å, respectively, consistent with the crystal structure. Importantly, total pore filling is already obtained at partial pressures as low as 0.2 p/p⁰, showing that both pores are fully accessible to all of the investigated gases. Ar exploration of the octahedral cavity with regard to the bigger Kr exhibits a different behavior. Because of higher Kr-Kr interactions, the latter fills these holes at a lower pressure than Ar. The estimated pore volume using Ar and N₂ is 0.92 cm³g⁻¹, which coincides with the computed pore volume from the crystal structure. Moreover, the Hf-DPA MOFs sample has been analysed via hyperpolarized ¹²⁹Xe NMR which is a peculiar NMR technique performed under a mixture of gas containing xenon. It monitors the change in the chemical shift associated to xenon when diffusing in a material in comparison with the signal of free xenon. This is a valuable method to understand the porosity of a material. In this case, a direct proof of the diffusion of a noble gas like ¹²⁹Xe inside Hf-DPA MOFs is given, even in competition with other gaseous species. The detection of the signal at $\delta = 97.7$ ppm within 200 ms demonstrates the fast diffusion in the Hf-DPA MOFs restricted pores⁸.

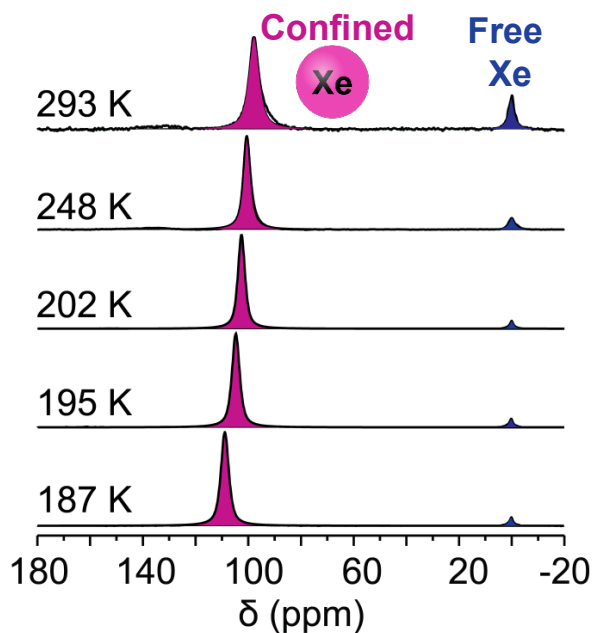


Fig. 4.11: Hyperpolarized ¹²⁹Xe NMR spectra of Hf-DPA at variable temperature, 2% xenon in a mixture with nitrogen and helium at different working temperatures.

4.2.2 Gas distribution inside Hf-DPA MOFs

The capacity of porous Hf-DPA to adsorb and concentrate radioactive isotopes of argon, krypton, xenon, and radon at room temperature was established using a combination of experimental and simulated methodologies. The adsorption isotherms derived using Grand Canonical Monte Carlo (GCMC) simulations are shown in Fig. 4.12. They correctly recreate the experimental isotherms for argon and krypton, indicating the predictive utility of the developed modeling. The simulation of adsorption at

a given pressure reveals a relationship between the quantity of gas adsorbed and the atomic mass, with a preference for heavier radon. Smaller gases, such as krypton, are more homogeneously distributed in all available space, whereas the larger radon atom is preferably hosted in the MOF's smaller tetrahedral cavities, due to more effective interactions between the gas molecules and the framework walls. The gas-matrix interaction energies provide insight into the framework's affinity and retention capabilities for the exploration gases, which are relevant for selectivity and detection applications in air. The gas diffusion model in the presence of air at room temperature shows that krypton atoms pervade the entire MOF crystals in tens of microseconds, demonstrating that noble gas radionuclides could be rapidly adsorbed into the pores under standard working conditions.

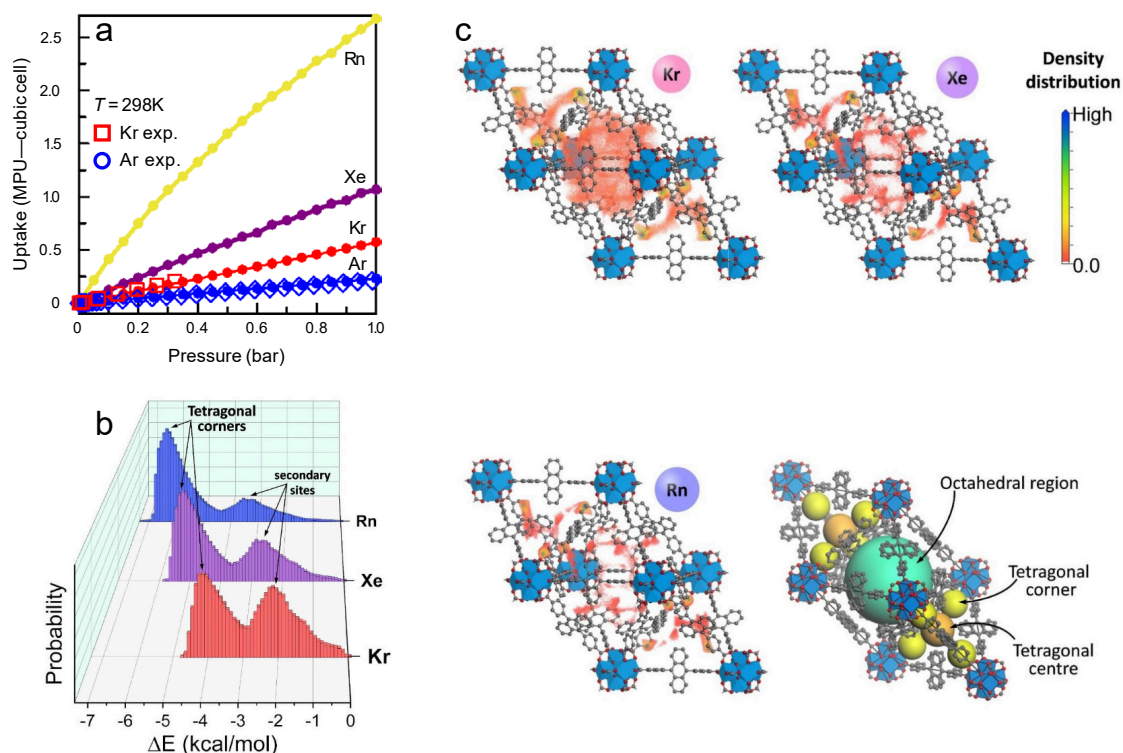


Fig. 4.12: a, Experimental argon and krypton isotherms and GCMC simulated adsorption isotherms of argon, krypton, xenon and radon for a cubic unit-cell of Hf-DPA ($32.79 \times 32.79 \times 32.79 \text{ \AA}^3$) at 298 K. The uptake is expressed in molecules per unit-cell (MPU). b, Energy distributions obtained from the fixed pressure GCMC adsorption simulations, performed at 5 kpa (0.05 bar) and 298 K, for Kr, Xe and Rn. c, Gas density distributions calculated at 5 kpa (0.05 bar) and 298 K using fixed pressure GCMC adsorption simulations for Kr, Xe and Rn using the primitive unit-cell of Hf-DPA. Red indicated very low density while blue indicates the highest. The use of the primitive cell allows for better visualization of the pore occupancy. The spherical representations of the different pores are shown to more easily correlate the pores with the density distribution.



4.3 Hf-DPA MOFs photoluminescence and scintillation properties

Hf-DPA MOFs has been synthesized as porous scintillators, thus the study of their photophysical properties is the starting point for the understanding of the potentialities of this material in the gas detection field.

The first element to be analysed is the photoluminescence of the DPA ligand. In general, DPA is a well-known molecule extensively used in the scintillation field due to its high light yield (>10000 ph/MeV)¹⁵ in crystal form and its photoluminescence decay time under ten of nanoseconds. Here are presented the continuous wave photoluminescence (CW-PL), the absorption (ABS) and time resolved photoluminescence (TR-PL) signals of 9,10-bis(4-carboxyphenyl)anthracene excited at 340 nm and collected at 430 nm in a tetrahydrofuran (THF) solution. In Fig 4.13 it is appreciable how the time resolved signal of the moieties resembles a full mono-exponential decay, typical of conjugated organic molecules, with a characteristic lifetime of 5 ns.

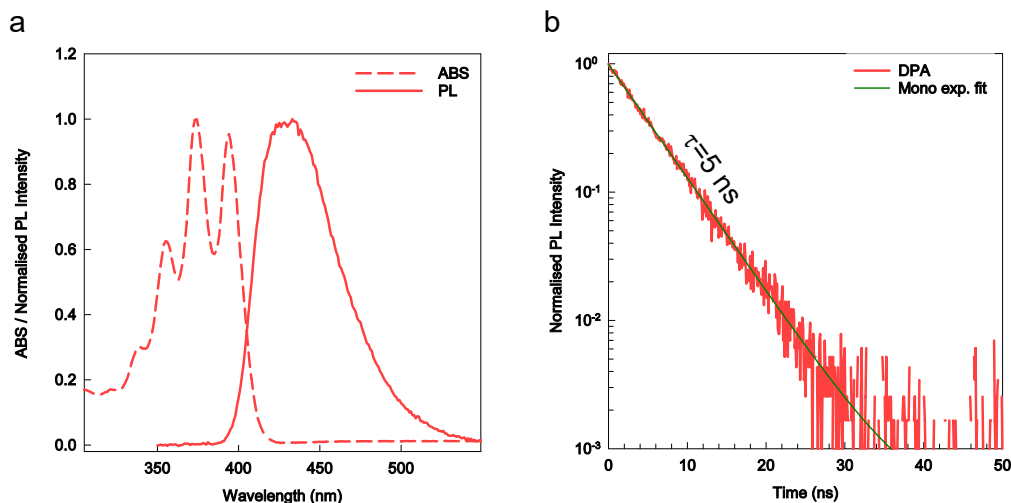


Fig. 4.13: a, photoluminescence (PL) and absorption (ABS) spectra of 9,10-bis(4-carboxyphenyl)anthracene. b, Time resolved photoluminescence spectra (TR-PL) of 9,10-bis(4-carboxyphenyl)anthracene (red) and mono-exponential fitting function (green) displaying a typical lifetime of 5 ns.

When dealing with MOFs architecture, the properties displayed by the single molecule change. Fig. 4.14 shows the steady-state photoluminescence and excitation photoluminescence (PLE) spectra of Hf-DPA dispersed in THF. Upon 405 nm ultraviolet excitation, the solution showed a bright blue fluorescence peaked at 450 nm. With the respect to DPA single molecule, the PL spectrum of Hf-DPA MOFs resulted to broadened. This peculiarity mirrors the presence of an environment strongly affected by the local distribution of the sizes of Hf-DPA MOFs^{5,16}. Bigger MOFs tend to emit at longer wavelength in comparison with smaller ones, resulting in a superposition of the different emission spectra. Moreover, the high density of DPA molecules present in a single framework pushes the fluorescence peak at longer wavelengths, still in comparison to the single molecule photoluminescence properties. On the other hand, the PLE profile collected at 450 nm matches the vibronic replica of the DPA moieties. The same experiments executed above are performed also on Hf-DPA MOFs in powder form. Fig. 4.14 shows also the PL spectra collected at a cryogenic temperature of 77 K that display a blue shift of the emission in comparison to the measurements acquired at room temperature. The PL peak for the solution shifts from 450 nm to 440 nm while in powder form shift from 490 nm to 480nm. Furthermore, the spectra display a narrowing of the emission. Both the narrowing and the blue shift at 77 K are linked to the vibration-free alignment of the transition happening at the cryogenic regime that reduces the phenomenon of self-absorption.

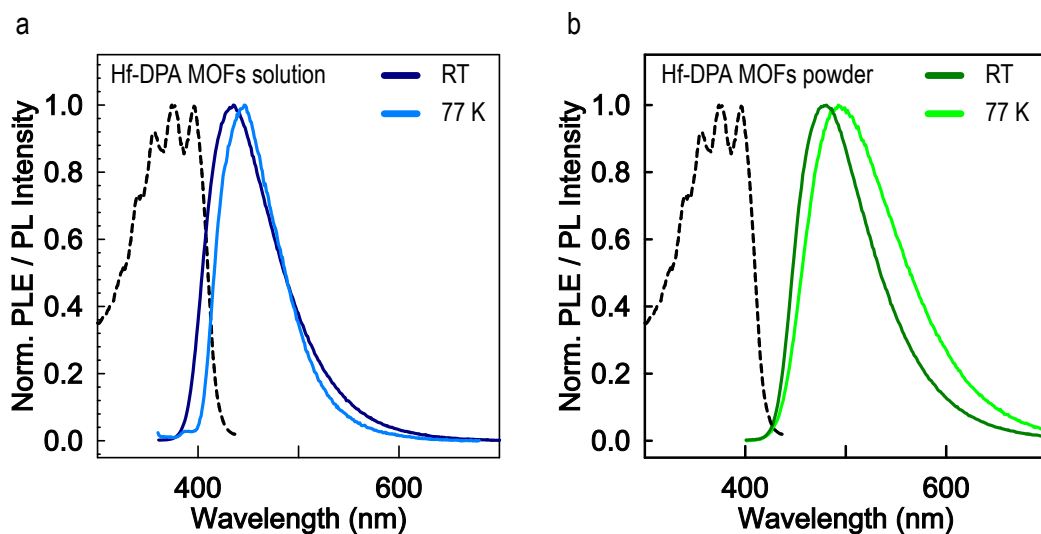


Fig. 4.14: The excitation photoluminescence (PLE, dashed line) and photoluminescence (PL) emission spectra of MOF crystals dispersed in THF (5×10^{-8} M) (a) or as bare powder (b). The photoluminescence was recorded at 300 K (solid line) and 77 K (dotted line). The excitation wavelength is 355 nm.



Time resolved photoluminescence was also performed on the MOF dispersion and on the powder sample. The Hf-DPA MOFs dispersion at room temperature displayed a characteristic average decay time of 2.8 ns and a photoluminescence quantum yield of 0.41 ± 0.06 (relative QY in comparison with DPA, QY=0.97). When dealing with cryogenic temperature, it is registered an increased decay time of 3.3 ns, which indicates an emission yield increment to $0.41 \times (3.3 \text{ ns}/2.8 \text{ ns}) = 0.48$ (+18%). This verifies the absence of significant thermal quenching by intramolecular vibrational processes in Hf-DPA MOFs^{5,10,16}. When dealing with powder, the emission lifetime of 2.4 ns remains almost constant. At 77 K, the emission maxima is slightly blue shifted to 480 nm, with a lifespan increase to 3.5 ns, demonstrating that the MOF powder's excited state electronic properties are similar with those of single crystals in diluted dispersion.

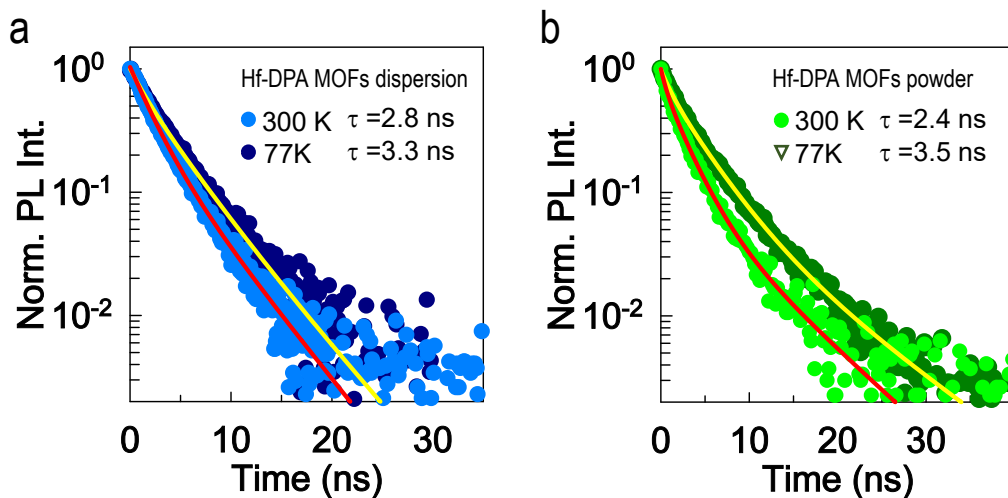
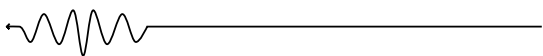


Fig. 4.15: a, b, Photoluminescence intensity (PL int.) decay as a function of time recorded at the photoluminescence maximum emission wavelength under 340 nm pulsed excitation. The solid lines represent the fit of data with multi-exponential decay functions that results in the average emission lifetime values reported.

Interestingly, the behaviour represented by the time decay dynamics is totally different from the one observed in DPA-only solution. Indeed, the TR-PL signal of Hf-DPA MOFs display a multi-exponential dynamic and a characteristic lifetime very different from the one of the DPA molecule. This can be explained through the phenomenon of concentration quenching: the presence of a multitude of DPA molecules surrounding a single Hf-cluster node modifies the ensemble emission, quenching it. Moreover, the presence of a distribution of sizes is another factor to consider when dealing with solid



state materials. Fig. 4.16 depicts the steady-state scintillation (radioluminescence) spectra of Hf-DPA MOFs powder under soft X-rays in comparison to the commercial plastic scintillator EJ-276. The radioluminescence profile of MOFs powder resembles the photoluminescence spectrum. Notably, despite the fact that the density of Hf-DPA MOFs is lower than that of EJ-276 ($0.6\text{--}0.7\text{ g cm}^{-3}$), the scintillation generated by MOFs is more than one order of magnitude stronger. This is due to the fact that the inclusion of heavy hafnium ions ($Z = 72$) enhances the interaction with ionizing radiation¹⁶ as seen in Chapter 1. The complete description of the scintillation phenomenon in Hf-DPA MOFs is also illustrated in Fig. 4.16. The high energy photon interact primarily with the heavy cluster of hafnium oxide due to their high Z and, thus, their higher interaction cross section. This event makes possible the ionization process inside Hf-DPA MOFs, generating high energy electrons and holes cascades. This shower of free charges is able to diffuse in the material until they thermalize and get collected by DPA molecules that represent the favourite de-excitation pathway. The charges thermalize once more when localized on the DPAs, giving rise to the visible emission.

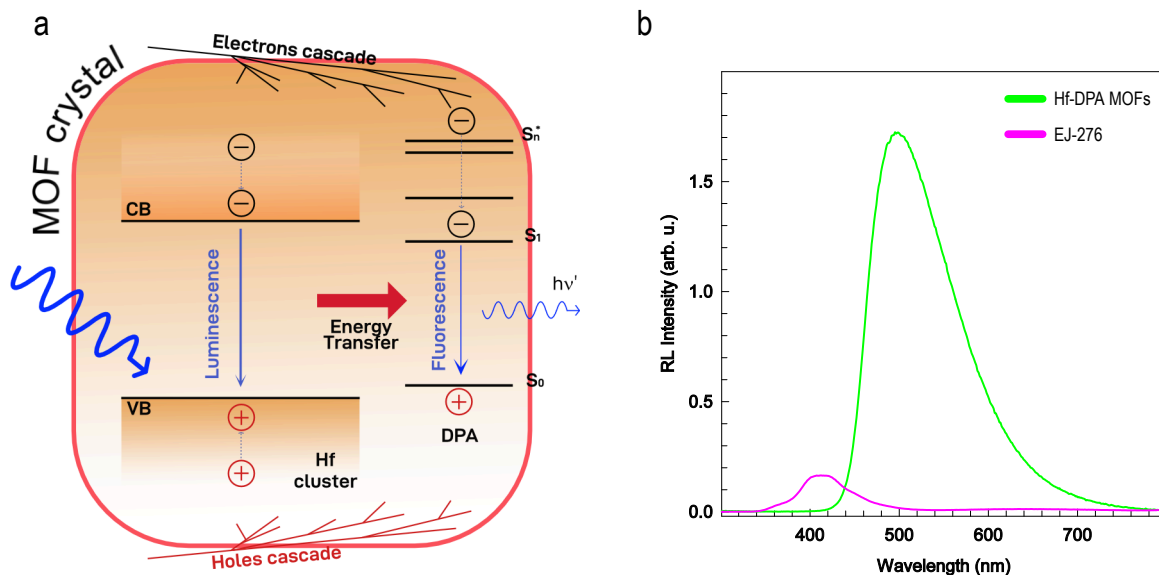


Fig. 4.16: a, Outline of the scintillation process. Free charges are generated by interaction of the ionizing radiation with the polymer and MOF nanocrystals. They recombine generating emissive singlets on the DPA molecules, where the fluorescence can be detected by a photon counter. The resonance between the X-ray-activated luminescence of the clusters and the DPA absorption enables the sensitization of singlets by radiative and non-radiative energy transfer from excited clusters. b, Radioluminescence (RL) spectrum of Hf-MOFs and plastic EJ-276 scintillator powders under soft X-rays.



Furthermore, Hf-DPA MOFs generate a quick scintillation light pulse with a sub-nanosecond rise time and a 3 ns average decay duration, which is consistent with photoluminescence decay dynamics. This demonstrates that the MOF emission characteristics are not altered by X-ray excitation. Hf-DPA MOFs photoluminescence and radioluminescence have been measured in relation to temperature. The MOF powder normalized photoluminescence spectra recorded cooling from 300 K to 10 K are shown in Fig. 4.18. Because band narrowing reduces self-absorption, the emission maximum wavelength moves to 480 nm at low temperatures. The inset shows the photoluminescence intensity increasing by +40% at temperatures below 100 K, corresponding to a quantum yield increase of up to 0.60. This improvement is more than predicted, given the commensurate increase in emission lifetime.

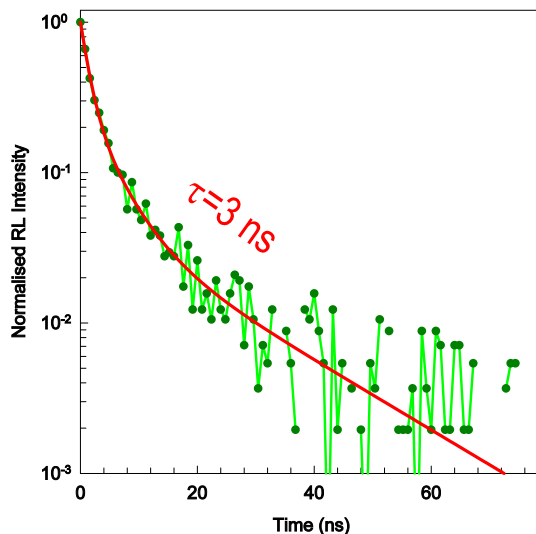


Fig. 4.17: scintillation decay signal of Hf-DPA MOFs excited through pulsed soft x-rays.

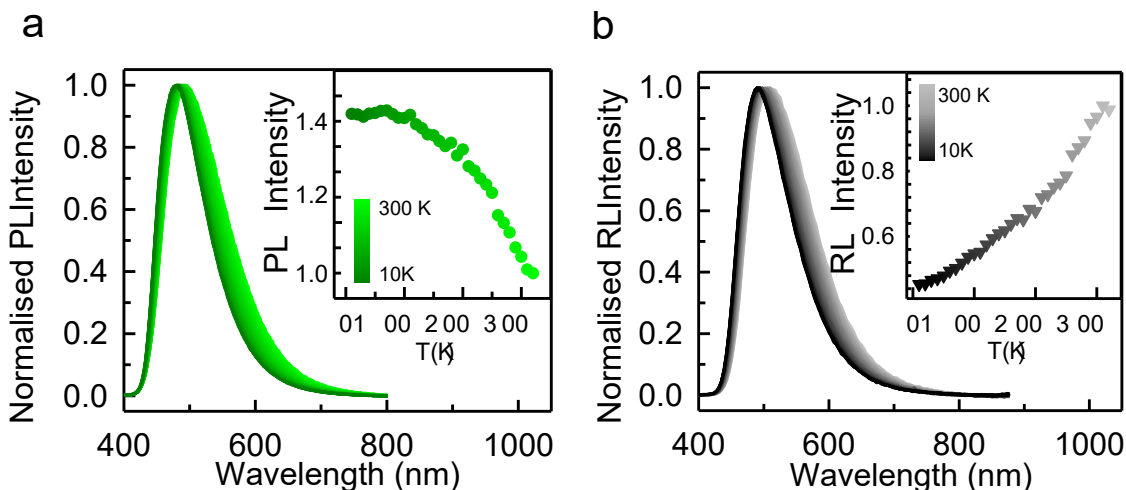
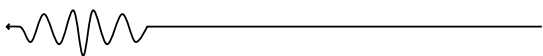


Fig. 4.18: Normalized PL (a) and RL spectra (b) of Hf-DPA powders as a function of temperature. The inset in b depicts the radioluminescence intensity normalized to the PL intensity variation shown in the inset of a, as a function of the temperature.



These findings imply that the partial emission quenching involves additional temperature-dependent ultrafast quenching mechanisms of diffusing charges or molecular excitons¹⁷. Variable-temperature radioluminescence investigations indicate the occurrence of traps. The photoluminescence spectrum affects the radioluminescence spectrum. The radioluminescence intensity, on the other hand, is lowered by a factor two at 10 K after being adjusted by the photoluminescence behaviour to highlight the intrinsic luminescence dependency on temperature. This is a signature of trapping sites, which compete with the recombination of diffusing free charges on emissive ligands. Thermal energy can release stored charges and allow them to be recovered for light production when temperatures approach a thermal equilibrium¹⁸, but at low temperatures they are lost with a fall in emission intensity. The role of the trap in scintillation is studied using wavelength-resolved thermally stimulated luminescence (TSL) measurements^{19,20}. The smooth TSL glow curve (obtained by integrating the wavelength-resolved TSL spectra across the entire emission region) demonstrates the presence of a wide range of trap sites with varying energy depths, which have no significant effect on the scintillation yield of the MOFs.

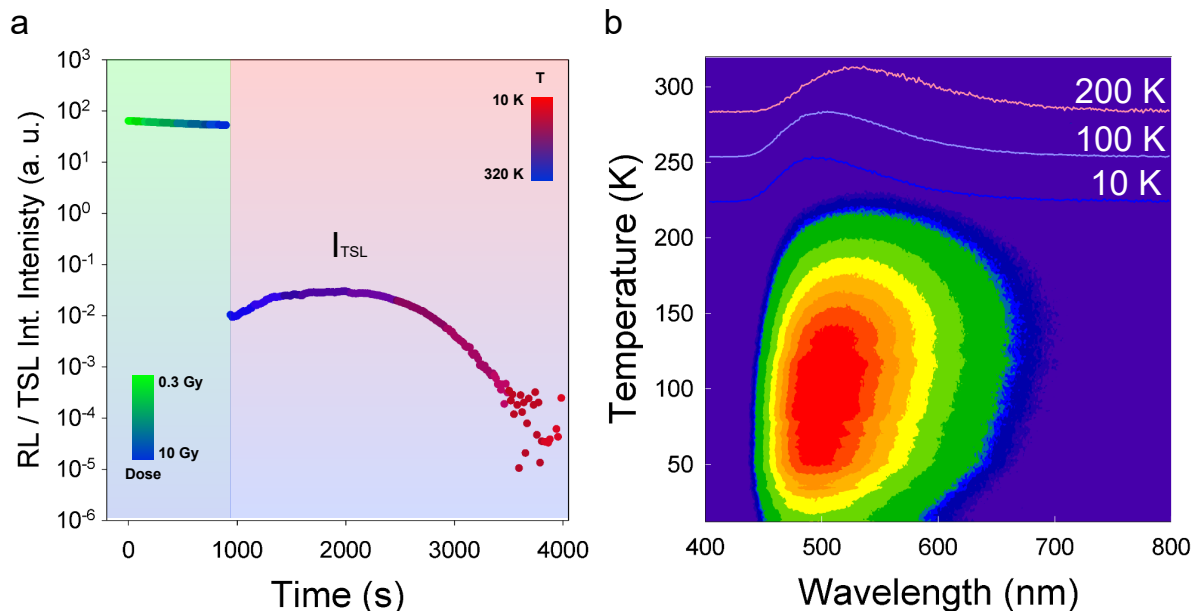


Fig. 4.19: a, RL intensity as a function of cumulated dose (green to blue dots) delivered in 900 s and TSL intensity (blue to red dots). b, Contour plot of wavelength-resolved TSL intensity.



To fill trap sites and minimize spontaneous depletion due to thermal energy, the MOFs are subjected to ionizing radiation up to roughly 10 Gy at 10 K²⁰. Following irradiation, the temperature of the sample is raised at a linear heating rate while the luminescence produced is monitored. This experiment demonstrates the role of de-trapped charges in the generation of scintillation light at ambient temperature. The form of the TSL signal vs. temperature, known as the material's glow curve, is determined by the type of the traps that are thermally releasing charge carriers. To separate the trap contribution to emission from the other processes involved in scintillation, the TSL intensity data have been adjusted for the fluctuation in radioluminescence emission intensity vs. temperature. The glow curve is broad and smooth, with no discernible signal peak, and rises at roughly 100 K. This featureless shape, free of any narrow peak structure indicating a specific energy, suggests the presence of a broad energy distribution of trap states^{21,22} which is consistent with the smooth radioluminescence and photoluminescence spectra, which reflect the presence of many different local environments and quenching pathways for the MOFs emitting ligands (Fig. 4.19). By computing $T\% = I_{TSL} / (I_{RL} + I_{TSL})$ it is possible to estimate the amount of light originating from the thermal release of trapped carriers and not contributing to the prompt scintillation response and for Hf-DPA MOFs is calculated to be 2.5%.

4.4 Radioactive gas detection by Hf-DPA MOFs

The synthetic pathway, the gas adsorption capabilities as well as the photoluminescence and scintillation properties of Hf-DPA MOFs have been explored in the last paragraphs. All these studies have been performed to understand the material in detail and to profile it for its final application: the detection of harmful radioactive gases. To do so, the micro-TDCR device analysed in Chapter 3 have been used. The micro-TDCR is a detector built with three photomultipliers working in coincidence that was primarily used for liquid scintillation counting and that now is a fundamental brick of the SPARTE project. The analysis on Hf-DPA MOFs were performed on a custom-made test bench at CEA (Fig. 4.20). Here an air sample mixed with radioactive gas is placed in the circuit. The gas concentration is known and so is the activity. A pump transports the mix inside the TDCR chamber. Here the Hf-DPA MOFs are placed inside a vial like the one in Fig. 4.20 at the centre of the device. The gas gets pumped in the measurement vial, and it

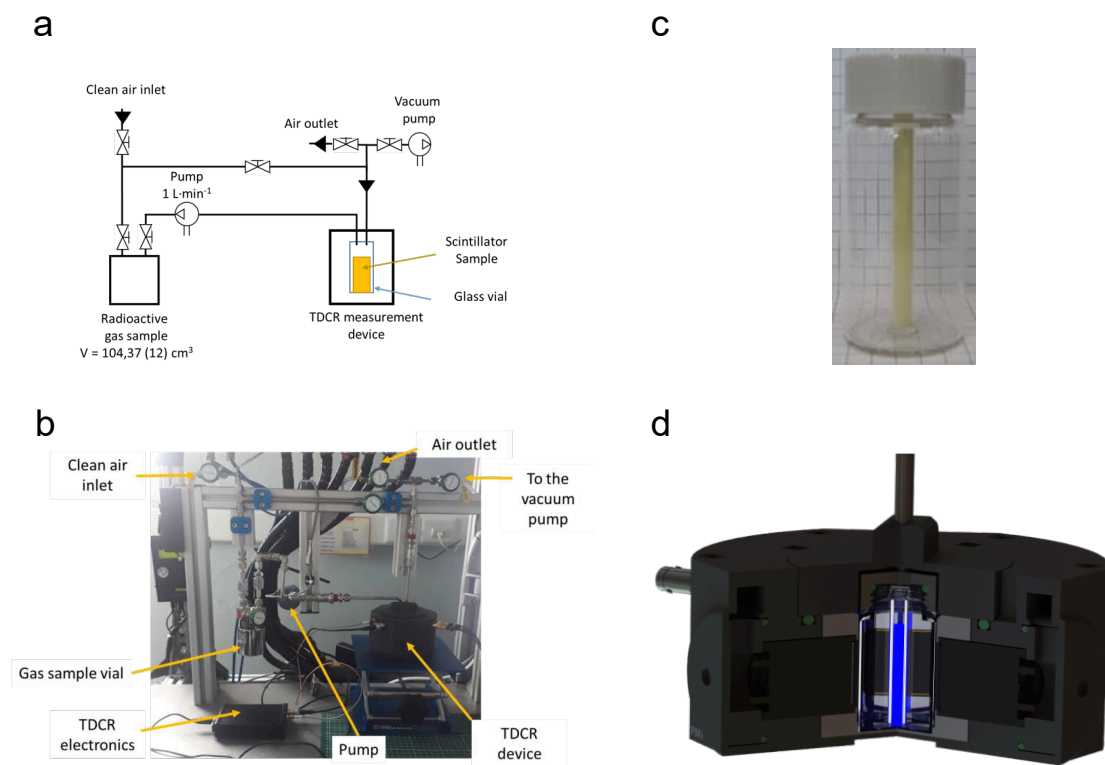
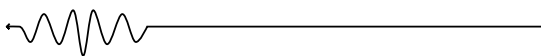


Fig: 4.20: a,b, custom-made set up for radioactive gas detection. c, d, vial used for Hf-DPA MOFs analysis and its placement inside the microTDCR.

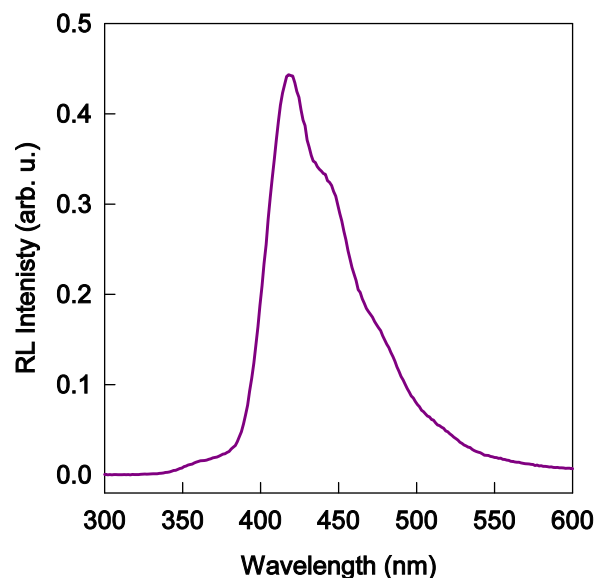


Fig. 4.21: RL of dye-doped PS microspheres.

gets adsorbed by the material as seen in the paragraph 4.2. Once the atoms follow their decay path, the energy release by the β decay is deposited inside the material and the whole phenomenon of scintillation takes place. The gas used for this kind of analysis and available at CEA are: ^3H , ^{85}Kr , ^{222}Rn . The gas detection measurements were performed in relation with dye-doped polystyrene (a well-known scintillator in the field of plastics) microspheres²³. Since, currently, there is not a real standard in the field of porous scintillation, this

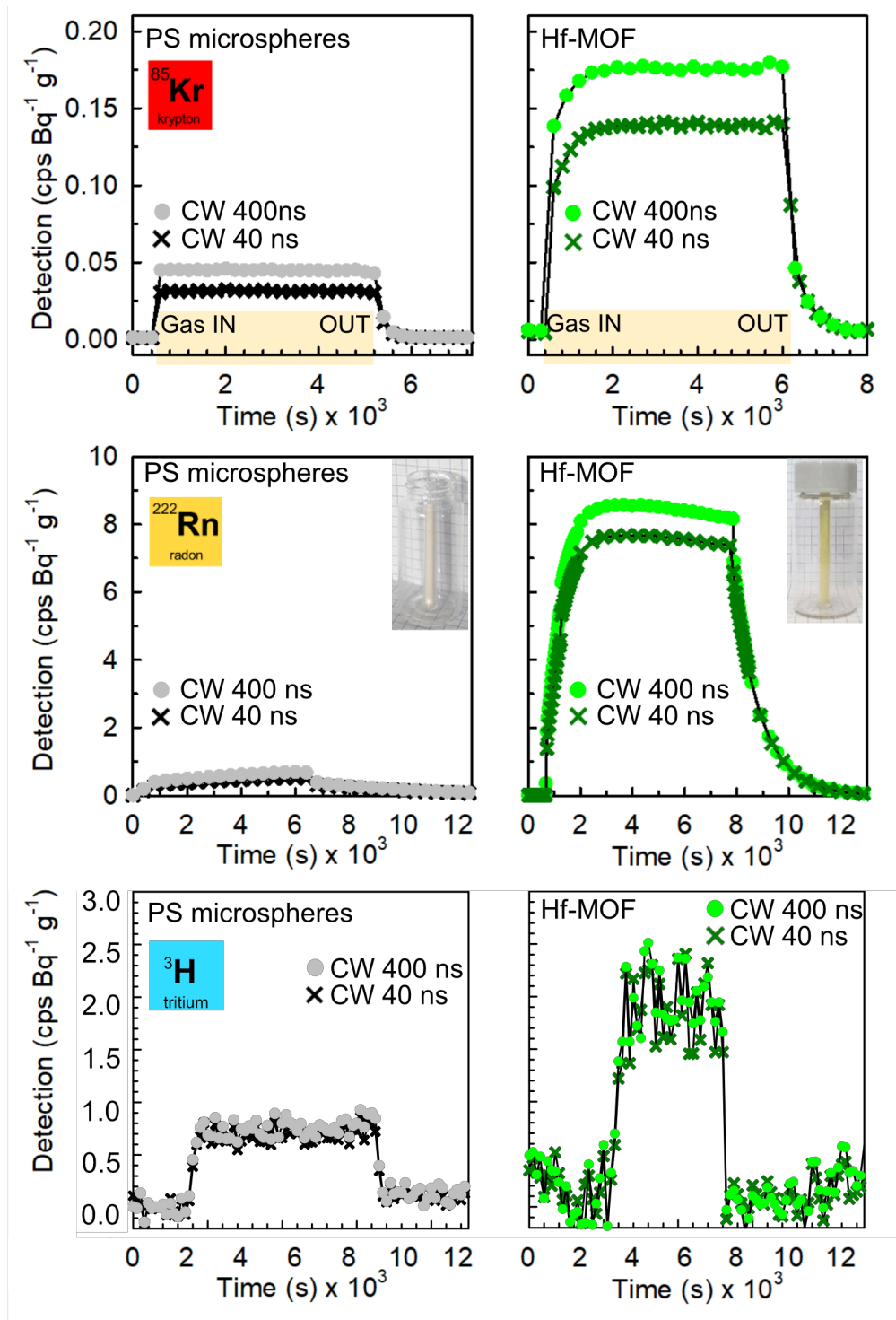
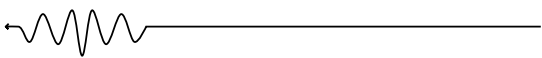


Fig. 4.22: Coincidence detection of ^{85}Kr (top), ^{222}Rn (middle) and ^3H (bottom) by polystyrene microspheres powder and Hf-DPA MOFs powder using two different coincidence windows (CWs) for detection (40 ns and 400 ns). The labels on the x-axis indicate when the radioactive gas has been injected into the detection device (gas in) and then washed out by a flux of clean air (gas out). cps, counts per second.



material represents the only way to understand the Hf-DPA MOFs capabilities. The RL feature of these microspheres is represented in Fig. 4.21. The Hf-DPA has been tested using a radioactive isotope of krypton (^{85}Kr). The electrons produced by the β -decay of ^{85}Kr have an average energy of 251.4 keV and a maximum emission energy of 687.1 keV. To adjust the activity of the gas sample, different concentrations of the radionuclide can be blended in the air. The TDCR technique can be applied using different coincidence windows to maximize the device's sensitivity^{24,25}. The coincidence windows used with Hf-DPA MOFs are 40 ns (as used with liquid scintillators) and 400 ns. The results for detecting ^{85}Kr utilizing 175 mm diameter dye-doped polystyrene microspheres and Hf-DPA are shown in Fig. 4.22. The statistics show that porous crystals behave efficiently. First, for coincidence windows with 40 ns and 400 ns, respectively, Hf-DPA produces scintillation intensities that are approximately 4.6 and 3.9 times higher than those of microspheres. This shows that Hf-DPA is an effective scintillator despite having a lower intrinsic density than polystyrene (0.65 g cm^{-3} vs 1.02 g cm^{-3}). Notably, the reproducibility of gas detection is quite good (1.3% for

40 ns and 2.5% for 400 ns coincidence windows, respectively). Moreover, the polystyrene emission peaked at 420 nm, wherein the PMTs detection efficiency (0.43) is higher than for the 490 nm MOF emission (0.25). A further improvement of the detection efficiency can therefore be envisaged by matching the scintillator and photodetector properties. Second, compared to polystyrene, the predicted increment utilizing a longer coincidence window is less pronounced for Hf-DPA (+50% vs +25%, respectively). This suggests that MOFs perform better as

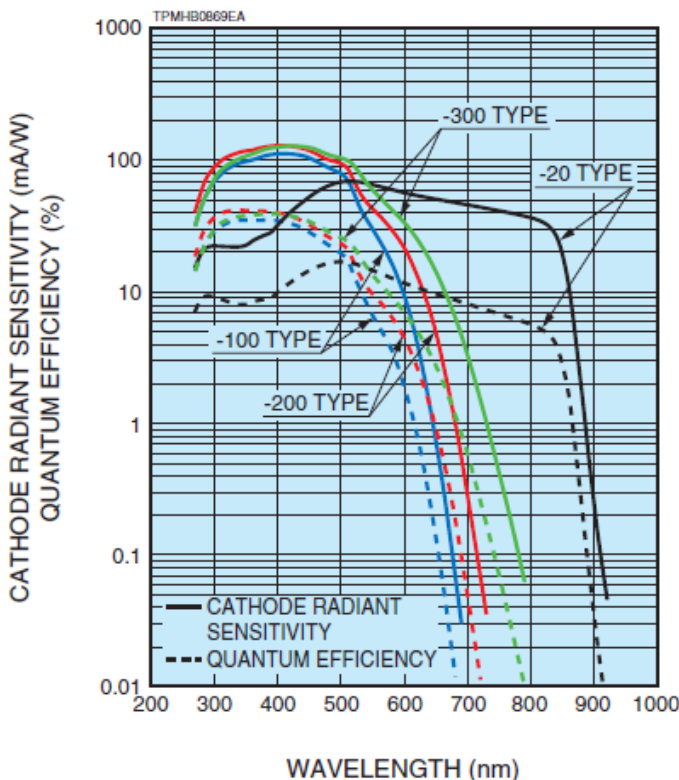
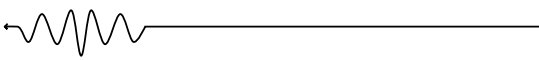


Fig. 4.23: micro-TDCR PMTs quantum efficiency, via HAMAMATSU.



fast scintillators with a small contribution from slow emission, providing a response that is closer to the desired time-independent behaviour. Third, MOFs have slower kinetics than polystyrene when it comes to reaching the maximal scintillation signal. The signal rise time for Hf-DPA is about 600 s compared to 100 s for microspheres, which is measured as the amount of time needed to reach 90% of the maximum plateau. When the radionuclides are removed from the sample by purging with clean air, a similar effect is shown. While it takes the polystyrene microspheres half as long, the scintillation stops in 800 s for MOFs. These results suggest that the radionuclides are adsorbed within the MOF pores, in agreement with the experimental and simulated adsorption tests, in addition to the fast, automatic filling of interparticle space within packed microspheres, thereby promoting the interaction of the β -radiation with the scintillator that leads to improved performance. Testing Hf-DPA MOFs crystals as detectors with other interesting radionuclides, such as ^3H and ^{222}Rn (with its four equilibrium decay products, which are low- and high-energy emitters), showed the adaptability of this method. Given the greater radon capture in the pores, the output of the scintillation should increase in comparison to krypton. In comparison to polystyrene, the detection efficiency has been increased twentyfold. The MOF powder exhibits superior sensitivity in the detection counting rate, which is double that of polystyrene, even for the elusive tritium. Given that ^3H is one of the most challenging gas atoms to detect and that its typical β -radiation energy is only a few keV, this result is crucial. With regard to krypton, we further examined the device in relation to the sample's activity since a steadily increasing number of sensitive detectors is needed. Figure 4.24 illustrates how Hf-DPA MOFs were able to detect ^{85}Kr from an initial activity of 21 kBq m^{-3} down to 0.3 kBq m^{-3} , which is two orders of magnitude less. Since the instrumental response is linear with the sample activity, it is possible to calibrate equipment to extremely low activity levels with great accuracy. Due to the porous scintillator's capacity to adsorb the gas, the MOFs crystals were able to successfully detect an activity below the minimum value declared for commercial ^{85}Kr detectors in a device that was much smaller in size, with less monitored gas, and using acquisition times that were one order of magnitude shorter^{26,27}. These astonishing results emphasize the potential technological advantage of adopting compact, user-friendly, and less expensive devices by demonstrating that the prototype device shown here, although being in its embryonic condition, exhibits better sensitivity than cutting-edge equipment. This work strongly encourages the



development of radioactive gas detectors based on porous MOF crystals as scintillators in order to get around current technological constraints, especially in light of the good stability of Hf-DPA that does not require any critical storage protocol.

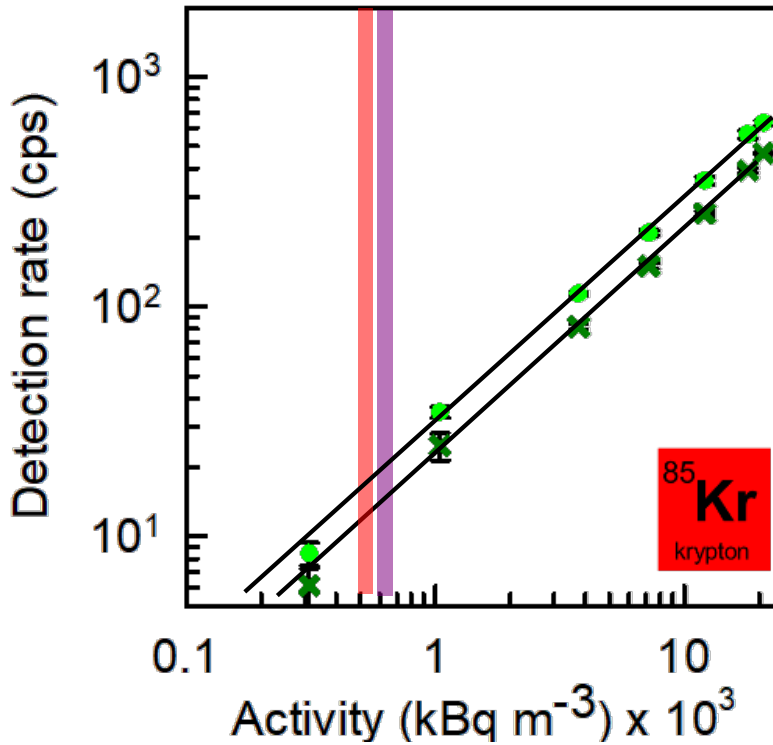


Fig. 4.24: Double coincidence detection rate of ^{85}Kr by the Hf-DPA powder as a function of the sample activity using different coincidence windows. The vertical lines mark the detection limit of a commercial device employed for detecting noble gas radionuclides (red and violet line, respectively ^{26,27}). The solid lines are the fit of data with linear functions. Error bars depict the residual values of the fit.



4.5 Methods

Nuclear magnetic resonance (NMR) spectroscopy

^1H -NMR spectra were recorded on a AVANCE NEO Bruker instrument (400 MHz).

Powder X-ray diffraction

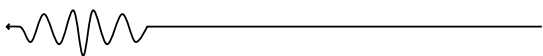
PXRD measurements of Hf-DPA-x were collected with a Rigaku Smartlab powder diffractometer over a range for 2θ of $3.0 - 50.0^\circ$ with a step size of 0.02° and a scan speed of $1.0^\circ \text{ min}^{-1}$ using Cu-K α radiation, 40 kV and 30 mA. PXRD measurements of Hf-DPA, Hf-DPA-a, Hf-DPA-b, Hf-DPA-c were collected over a range for 2θ of $2.0 - 80.0^\circ$ with a step size of 0.02° and a scan speed of $0.3^\circ \text{ min}^{-1}$ using Cu-K α radiation, 40 kV, 30 mA. The activated powder samples were deposited on a zero-background silicon sample holder.

Scanning electron microscopy (SEM) and energy-dispersive spectroscopic analysis (EDS).

Scanning electron microscopy (SEM) images were collected using a Zeiss Gemini 500 microscope, operating at 5 KV and a working distance of 4.7 mm. The sample was deposited on a silicon slide from 2-propanol dispersion, dried under high vacuum and sputtered with gold before the analysis (10 nm, nominal thickness). Particle size distributions were measured from SEM images using ImageJ software. The linear dimensions of nanocrystals have been evaluated over more than 100 particles to determine the particle size distribution. Energy-dispersive spectroscopy (EDS) was performed using a Bruker XFlash 6-30 detector accessory. MOF nanocrystals were dispersed in 2-propanol and deposited on a graphite stab, dried under high vacuum, and coated with graphite before the analysis.

Gas adsorption properties

N_2 and Ar adsorption isotherms at 77 K were collected up to 1 bar using a Micromeritics analyser ASAP2020 HD. Kr adsorption isotherms at 77 K and 298 K up to 1 bar were collected on a Micromeritics Triflex instrument. Samples were previously outgassed overnight at 130° C under high vacuum (10^{-3} mmHg) to remove the adsorbed species. N_2 , Ar and Kr adsorption isotherms at 77 K were fitted using Langmuir and BET models and surface



areas were calculated in the range from 0.015 to 0.08 p/p° (radii of N₂ = 0.162 nm, Ar = 0.1940 nm and Kr = 0.207 nm). Pore size distributions (PSD) were calculated according to Non-Local Density Functional Theory (NLDFT) model.

Hyperpolarized ¹²⁹Xe NMR experiments

The laser-assisted technique is based on the excitation transfer from the optically pumped rubidium vapours to the ¹²⁹Xe atoms, increasing the polarization by hundreds of times with respect to the NMR signal of Xe nuclei under thermal equilibrium conditions. Thus, signals can be recorded with high sensitivity even at low Xe concentrations. Importantly, the hyperpolarized ¹²⁹Xe gas is diluted at 2% in a mixture of N₂ (4%) and He (94%), demonstrating the effective uptake of Xe even in competition with other gaseous species and under flow conditions. The ¹²⁹Xe mixture flows into the main magnetic field and immediately diffuses in the MOF pores, reporting information on the preferred adsorption sites of the open framework. The remarkable downfield signal, compared to that of the free gas, is diagnostic of the restricted space explored by the noble gas. It is worth noting that the noble gas Xe possesses a van der Waals radius of 2.16 Å which is intermediate and comparable to those of Kr and Rn (2.02 Å and 2.2 Å, respectively), thus hyperpolarized ¹²⁹Xe NMR is a suitable technique to demonstrate the accessibility of radionuclides of interest in the Hf-DPA pores of under low pressure and flow conditions. At room temperature, an isotropic signal was detected at $\sigma = 97.7$ ppm within 200 ms from Xe delivery to Hf-DPA MOFs, proving the fast diffusion of Xe atoms through the pores into the confining cavities. On lowering temperature, the resonances move to even higher chemical shifts due to the longer residence time close to the pore walls. It is worth noting that the noble gas Xe possesses a van der Waals radius of 2.16 Å which is intermediate and comparable to those of Kr and Rn (2.02 Å and 2.2 Å, respectively), unveiling the accessibility of radionuclides of interest in the Hf-DPA MOFs pores of under low pressure and flow conditions.



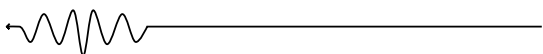
Grand Canonical Monte Carlo simulations

GCMC simulations were performed using the cubic unit cell for Hf-DPA (32.79x32.79x32.79 Å) which contains 4 octahedral and 8 tetrahedral spaces. We used our modified dreiding forcefield that were empirically adjusted to reproduce the experimental sorption data and adsorbed gas densities. Dispersion interactions cutoff was set at 12.5 Å and the simulations were performed using 106 production steps and 105 equilibration steps to ensure that the Monte Carlo has equilibrated at each step. GCMC simulations for Ar and Kr at 77 K for comparison to the experimental adsorption data. Then then Xe and Rn were calculated at 195 K since this xenon sorption cannot be performed at 77K (the pressure required is extremely low). Sorption simulations for all 4 noble gasses studied here were also performed at 298 K up to 1 bar. Fixed pressure GCMC calculation were performed at 5 kPa (0.05 bar) and 298 K to determine and visualize the density distribution of the 4 noble gasses within the cubic cell of Hf-DPA.

Photoluminescence studies

Absorption spectra were recorded using a Cary Lambda 900 spectrophotometer at normal incidence with Suprasil quartz cuvettes with a 0.1 cm optical path length and an integrating sphere to eliminate scattering effects. Steady-state photoluminescence spectra were acquired using a Varian Eclipse fluorimeter (bandwidth 1 nm) using quartz cuvettes of 0.1 cm optical path length. Time-resolved photoluminescence spectra of the MOFs dispersions were recorded by monitoring the emission decay of the samples at 435 nm. The MOFs were excited with a pulsed light-emitting diode at 340 nm (3.65 eV, pulse width 80 ps; EP-LED 340, Edinburgh Instruments). Photoluminescence decay times were measured at the maximum of the emission spectrum. The time resolved photoluminescence (PL) spectra and scintillation data discussed in the main text show in general a complex behaviour. The signal decay has been reproduced with an analytical multi-exponential function:

$$I_H(t) \propto \sum A_i e^{-\left(\frac{t}{\tau_i}\right)}$$



The parameters used for the fitting procedure are reported in Table 1. The characteristic emission lifetime τ_{avg} has been calculated as the weighted average of the characteristic decay time for each i-exponential function by:

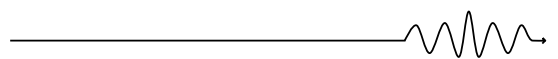
$$\tau_{avg} = \frac{\sum_i A_i * \tau_i}{\sum_i A_i}$$

@max PL	τ_1 (ns)	A ₁	τ_2 (ns)	A ₂	τ_3 (ns)	A ₃	τ_{avg} (ns)
Hf-MOF							
THF 300 K	2.5	0.97	8.8	0.03	-	-	2.8
THF 77 K	1.3	0.19	3.2	0.53	4.9	0.28	3.3
powder 300 K	0.6	0.23	2.3	0.66	6.6	0.11	2.4
powder 77 K	1.7	0.43	5.0	0.57	-	-	3.6
@max scint							
powder	1.4	0.69	4.6	0.26	18.7	0.05	3.0

Tab 1: Fit parameters employed to analyze the time resolved photoluminescence intensity decay spectra recorded on Hf-MOFs dispersions in THF and bare powders.

Radioluminescence and scintillation studies

The samples were excited by unfiltered X-ray irradiation using a Philips PW2274 X-ray tube, with a tungsten target, equipped with a beryllium window and operated at 20 kV. At this operating voltage, X-rays are produced by the Bremsstrahlung mechanism, superimposed to the L and M transition lines of tungsten due to the impact of electrons generated through a thermionic effect and accelerated onto the tungsten target. Cryogenic radioluminescence measurements are performed in the 10–370 K interval. Radioluminescence has been recorded on powder samples of 1 mm thickness in an aluminium sample holder. For comparison the radioluminescence spectra has been normalized by the mass of the investigated powder. Scintillation has been recorded under pulsed X-rays with energies up to 25 keV generated with a repetition rate of 1 MHz by a picosecond diode laser at 405 nm (Delta diode from Horiba) focused on an X-ray tube (model N5084 from Hamamatsu). The resulting photons were collected by Kymera spectrograph (ANDOR) and detected by a hybrid PMT 140-C from Becker and Hickl GmbH. For decay-time measurements, the photons were histogrammed using a PicoHarp300 time-correlated single-



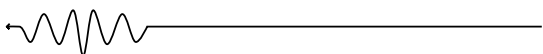
photon counting (32 ps time per bin) and for the time resolved spectra a MCS6A multiple-channel time analyzer was used (800 ps time per bin). Subnanosecond scintillation emission kinetics of the samples were measured with a time-correlated single-photon counting set-up.

Thermally stimulated luminescence measurements

Wavelength-resolved TSL at cryogenic temperatures is performed by using the same detection system as for radioluminescence measurements. Cryogenic TSL measurements are performed in the 10–320 K interval, with a linear heating rate of 0.1 K s^{-1} , after X-ray irradiation up to around 10 Gy. The dose values for X-ray irradiations were calibrated with an ionization chamber in air.

Radioactive gas detection experiments

The experiments are performed using a unique gas bench developed at the CEA, Paris-Saclay, and by allowing the production of radioactive gas atmospheres using high activity standards. Different sampling and dilution steps allow for precise control of the injected activity, and precise knowledge of the volumetric activity of each gas: at best, the relative standard uncertainty on the activity concentration is 0.4%, 0.6% and 0.8% for ^{222}Rn , ^{85}Kr and ^3H , respectively. For each experiment, the same type of three step sequence is performed. First, the measurement of the blank, by circulating clean air without additional radioactivity. Second, the measurement of scintillation by circulating the radioactive gas sample into the vial (4 mm diameter and 50 mm height, 0,1086 g for Hf-DPA and 0.3640 for polystyrene microspheres, activity 10 kBq). Third, circulation of clean air into the device to remove the radioactive gas. The light photons produced by scintillation are measured using a metrological device developed to exploit the triple-to-double coincidence ratio, with a specific connection cap adapted to the radioactive gas flow in the scintillator.

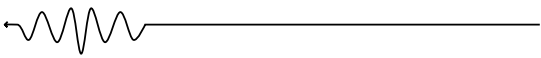


4.6 References

1. Zhou, H. C., Long, J. R. & Yaghi, O. M. Introduction to metal-organic frameworks. *Chemical Reviews* vol. 112 673–674 Preprint at <https://doi.org/10.1021/cr300014x> (2012).
2. Batten, S. R. et al. Terminology of metal-organic frameworks and coordination polymers (IUPAC recommendations 2013). *Pure and Applied Chemistry* **85**, 1715–1724 (2013).
3. Allendorf, M. D., Bauer, C. A., Bhakta, R. K. & Houk, R. J. T. Luminescent metal-organic frameworks. *Chem Soc Rev* **38**, 1330–1352 (2009).
4. Bauer, C. A. et al. Influence of connectivity and porosity on ligand-based luminescence in zinc metal-organic frameworks. *J Am Chem Soc* **129**, 7136–7144 (2007).
5. Allendorf, M. D., Houk, R. J. T., Bhakta, R., Nielsen, I. M. B. & Doty, F. P. Scintillating Metal Organic Frameworks: A New Class of Radiation Detection Materials. (2009).
6. Perego, J. et al. Composite fast scintillators based on high-Z fluorescent metal-organic framework nanocrystals. *Nat Photonics* **15**, 393–400 (2021).
7. Perego, J. et al. Highly luminescent scintillating hetero-ligand MOF nanocrystals with engineered Stokes shift for photonic applications. *Nat Commun* **13**, (2022).
8. Orfano, M. et al. Efficient radioactive gas detection by scintillating porous metal-organic frameworks. *Nat Photonics* **17**, 672–678 (2023).
9. Mallick, A. et al. Unprecedented Ultralow Detection Limit of Amines using a Thiadiazole-Functionalized Zr(IV)-Based Metal-Organic Framework. *J Am Chem Soc* **141**, 7245–7249 (2019).
10. Monguzzi, A. et al. Highly Fluorescent Metal-Organic-Framework Nanocomposites for Photonic Applications. *Nano Lett* **18**, 528–534 (2018).
11. Comotti, A. et al. Fluorinated porous organic frameworks for improved CO₂ and CH₄ capture. *Chemical Communications* **55**, 8999–9002 (2019).



12. Bassanetti, I. et al. Flexible porous molecular materials responsive to CO₂, CH₄ and Xe stimuli. *J Mater Chem A Mater* **6**, 14231–14239 (2018).
13. Comotti, A., Bracco, S., Valsesia, P., Ferretti, L. & Sozzani, P. 2D multinuclear NMR, hyperpolarized xenon and gas storage in organosilica nanochannels with crystalline order in the walls. *J Am Chem Soc* **129**, 8566–8576 (2007).
14. Sozzani, P. et al. Nanoporosity of an organo-clay shown by hyperpolarized xenon and 2D NMR spectroscopy. *Chemical Communications* 1921–1923 (2006) doi:10.1039/b602040b.
15. Van Loef, E. V., Mukhopadhyay, S., Zaitseva, N., Payne, S. & Shah, K. S. Crystal growth and characterization of 9,10-diphenylanthracene. in *Journal of Crystal Growth* vol. 352 103–105 (2012).
16. Lustig, W. P. et al. Metal-organic frameworks: Functional luminescent and photonic materials for sensing applications. *Chemical Society Reviews* vol. 46 3242–3285 Preprint at <https://doi.org/10.1039/c6cs00930a> (2017).
17. Ding, T. X., Olshansky, J. H., Leone, S. R. & Alivisatos, A. P. Efficiency of hole transfer from photoexcited quantum dots to covalently linked molecular species. *J Am Chem Soc* **137**, 2021–2029 (2015).
18. Guerassimova, N., Garnier, N., Dujardin, C., Petrosyan, A. G. & Pedrini, C. X-ray excited charge transfer luminescence of ytterbium-containing aluminium garnets. www.elsevier.nl/locate/cplett.
19. Buryi, M. et al. Trapping and Recombination Centers in Cesium Hafnium Chloride Single Crystals: EPR and TSL Study. *Journal of Physical Chemistry C* **123**, 19402–19411 (2019).
20. Vedda, A. et al. Trap-center recombination processes by rare earth activators in YAlO₃ single crystal host. *Phys Rev B Condens Matter Mater Phys* **80**, (2009).
21. Cova, F., Moretti, F., Dujardin, C., Chiodini, N. & Vedda, A. Trapping Mechanisms and Delayed Recombination Processes in Scintillating Ce-Doped Sol-Gel Silica Fibers. *Journal of Physical Chemistry C* **125**, 11489–11498 (2021).
22. Liu, S. et al. Towards Bright and Fast Lu₃Al₅O₁₂: Ce,Mg Optical Ceramics Scintillators. *Adv Opt Mater* **4**, 731–739 (2016).

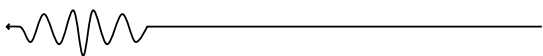


23. Santiago, L. M., Bagán, H., Tarancón, A. & Garcia, J. F. Synthesis of plastic scintillation microspheres: Evaluation of scintillators. *Nucl Instrum Methods Phys Res A* **698**, 106–116 (2013).
24. Dutsov, C., Cassette, P., Mitev, K. & Sabot, B. In quest of the optimal coincidence resolving time in TDCR LSC. *Nucl Instrum Methods Phys Res A* **987**, (2021).
25. Dutsov, C., Cassette, P., Sabot, B. & Mitev, K. Evaluation of the accidental coincidence counting rates in TDCR counting. *Nucl Instrum Methods Phys Res A* **977**, (2020).
26. FHT 59 E Noble Gas Monitor (Thermo Scientific, 2022).
27. XPR80 (Mirion Technologies, 2022).



HETERO-LIGAND MOFs: A PATH TO LIGHT OUTPUT OPTIMIZATION

The following chapter will be dedicated to the study of the properties of hetero-ligand MOFs, a new MOFs architecture that, through doping with precise amounts of a secondary fluorophore to enable the occurring of the energy transfer mechanisms, could lead to a re-absorption free emission. Moreover, the use of this system could be surely beneficial to better match the blue-peaked quantum efficiency of common PMTs leading to an enhancement of the response. In UNIMIB, this strategy was already realised but with a different acceptor ligand¹ and with a different aim, not included in the radioactive gas detection field. Indeed, MOFs with terphenyl (Tp) as donor, a fast UV organic emitter, and DPA as acceptor were synthesized and studied. In this case, ZrO₂ clusters were selected as heavy nodes. Indeed, Zr is a lighter element than Hf, but for source availability and cost, the choice was forced. Thus, it is not possible to compare Hf-DPA MOFs with this new system. On the other hand, the comparison can be fruitful by comparing Zr-Tp-DPA MOFs with Zr-DPA MOFs, i.e. MOFs without the terphenyl ligand, that is an available system well explored in a previous publication by Perego J., et al². The reader should keep in mind that this research is in its very early



stages, thus not all the characterization are available at the moment of the writing of this manuscript.

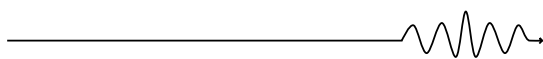
One of the widely occurring energy transfer mechanism in fluorescent dyad systems is surely the Förster Resonance Energy Transfer (FRET). This is a process occurring between two chromophores, one called donor and the other one called acceptor. The donor initially in its excited state may transfer its energy to the acceptor through dipolar interaction. This kind of interaction is not included in phenomenon of emission and reabsorption and so it is intended as a non-radiative process. In any case, the energies involved must be commensurable. Therefore, the fundamental properties for a dyes couple is the overlap between the emission of the donor and the absorption feature of the acceptor³. Being a dipole coupling process, the efficiency of FRET is strictly related to the inverse of the sixth power of the distance between donor and acceptor. Thus, a characteristic radius R_{FS} has been defined, which is the distance at which the FRET efficiency reaches the 50%:

$$R_{FS} = \left(\frac{9000(\ln 10)\kappa^2 Q_D}{128\pi^5 N n^4} \int_0^\infty \frac{F_D(\lambda)\varepsilon_A(\lambda)\lambda^4 d\lambda}{F_D(\lambda)d\lambda} \right)^{1/6} = \left(\frac{9000(\ln 10)\kappa^2 Q_D}{128\pi^5 N n^4} J \right)^{1/6}$$

where κ^2 is a factor describing the relative orientation in space of the transition dipoles of the donor and acceptor, Q_D is the quantum yield of the donor in absence of the acceptor, n is the refractive index of the medium, N is the Avogadro's number, $F_D(\lambda)$ is the corrected fluorescence intensity of the donor and $\varepsilon_A(\lambda)$ is the extinction coefficient of the acceptor at λ , which is typically in units of $(M^{-1} \text{ cm}^{-1})^3$. The integral term J is then describing the overlap between the features of donor and acceptor. The term related to the dipole orientation can be expressed as:

$$\kappa^2 = (\cos\theta_T - 3\cos\theta_D\cos\theta_A)^2$$

where r is the distance between the donor and acceptor, k_D is the radiative



time constant of the donor and k_{FRET} is the rate of the energy transfer that can be expressed as

$$k_{FRET} = \left(\frac{R_{FS}}{r}\right)^6 k_D$$

where τ_D is the donor emission lifetime in absence of acceptor. What is possible to observe experimentally when dealing with FRET is the donor fluorescence quenching both in continuous wave experiments and in time resolved measurements. By looking at the previous expressions, it is possible to underline that, being this process strictly dependent on the distance between the two species, the higher the acceptor concentration, the higher the rate of the energy transfer process. The efficiency of FRET can also be computed as

$$\phi_{FRET} = 1 - \frac{\tau_{D-A}}{\tau_D} = 1 - \frac{I_{D-A}}{I_D}$$

Where τ_{D-A} is the donor emission lifetime in presence of acceptor, τ_D is the donor emission lifetime in absence of acceptor, I_{D-A} is the donor emission intensity in presence of the acceptor and I_D is the donor emission intensity in absence of the acceptor. The result is a sigmoidal curve that represents the change in the FRET efficiency upon the increasing of the acceptor concentration. There is one simple case in which the donor decay times are very long so that diffusive motions of the donors result in their sampling of the entire available space. This is called the rapid diffusion limit^{3,4}.

This approach will be the starting point for the study of the interaction between the Tp and DPA moieties and then for the conceptualization of Zr-Tp-DPA MOFs crystals.

5.1 Synthesis and analysis of zirconium-based hetero-ligand MOFs

Briefly, ligands 2',5'-dimethyl-[1,1':4',1''-Terphenyl]-4,4''-dicarboxylic acid (Tp) and 9,10-bis(4-carboxyphenyl)anthracene (DPA) were synthesized with high purity using Suzuki coupling from commercial precursor. Zr-based heteroligand MOFs (Zr-Tp:DPA x %) were co-assembled under solvothermal conditions using benzoic acid as an effective modulator to control the growth of microcrystalline powder with well-defined octahedral crystal shape. 9,10-bis(4-carboxyphenyl)anthracene (DPA) was synthesized using a Suzuki coupling according to literature procedure, as shown in Chapter 4.

5.1.1 2',5'-dimethyl-[1,1':4',1''-Terphenyl]-4,4''-dicarboxylic acid (TP)

2',5'-dimethyl-[1,1':4',1''-Terphenyl]-4,4''-dicarboxylic acid (Tp) was prepared according to literature procedure with slight modification^{5,6}. 4-(methoxycarbonyl)phenylboronic acid (2.065 g, 11.47 mmol) and 1,4-dibromo-2,5-dimethylbenzene (1.0086 g, 3.82 mmol) were dissolved in a 2:2:1 toluene:dioxane:water mixture in a 100 mL Schlenk tube under nitrogen atmosphere. Nitrogen was bubbled for 1 hour to remove the oxygen from the reaction vessel. Potassium carbonate (3.244 g, 24.54 mmol) and bis(triphenylphosphine)palladium(II) dichloride (0.245 g, 0.35 mmol) were added to the solution and the reaction was heated at 90° C for 96 hours under vigorous stirring in a nitrogen atmosphere. After the synthesis, the reaction was cooled down to room temperature and the dioxane was rotary dried under vacuum. The product was extracted with chloroform, washed with brine (twice) and deionized water (twice), dried over anhydrous sodium sulphate, filtered and rotary dried under vacuum. The crude product (small yellow-whitish crystals) was dried under vacuum and purified by column chromatography using pure chloroform as eluent. The fractions with the product were collected and the solvent was rotary dried, resulting in a white microcrystalline solid. The white powder was

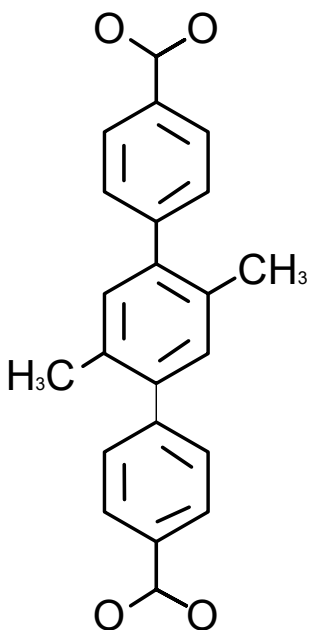


Fig. 5.1: Tp molecule.

vacuum and purified by column chromatography using pure chloroform as eluent. The fractions with the product were collected and the solvent was rotary dried, resulting in a white microcrystalline solid. The white powder was



dissolved in a mixture of deionized water (40 mL), EtOH (30 mL) and THF (110 mL) and potassium hydroxide (4.71 g; 30.48 mmol) was added to the solution. The mixture was heated to 66° C for 24 hours under stirring and then cooled to room temperature. The mixture was filtered through a paper membrane and hydrochloric acid (HCl) was added until pH = 1. The THF was removed by rotary evaporation and the white solid was filtered and washed with water to remove inorganic byproducts. The product was dried under vacuum at RT producing a white powder.

5.1.2 Hetero-ligand Zr-Tp-DPA MOFs

2',5'-dimethyl-[1,1':4',1''-Terphenyl]-4,4''-dicarboxylic acid (TP), 9,10-bis(4-carboxyphenyl) anthracene (DPA), benzoic acid (BA) and $\text{ZrOCl}_2 \cdot 8\text{H}_2\text{O}$ were weighted and inserted in a 8 mL glass vial. Dry DMF (2.5 mL) was inserted in each vial. The vials were closed with Teflon-lined caps and sonicated for about 1 minute. The vials were inserted in a pre-heated oven at 120° C for 14 hours to produce micrometre- sized crystals; then, they were removed from the oven and cooled down to room temperature. The microcrystalline powders were centrifuged, and the supernatant solutions removed. The samples were washed three times with DMF and three times with CHCl_3 before drying under high vacuum ($p < 2 \cdot 10^{-2}$ mmHg) at 100° C for 1 hour. By precise weighting it was possible to obtain hetero-ligand samples with a DPA % wt ranging from 0.01% wt to 20% wt. Moreover, pure terphenyl based Zr-MOFs and DPA based Zr-MOFs were synthesised in order to estimate the possible structural changes. Powder X-ray diffraction analysis demonstrated the generation of highly crystalline MOFs with different molar ratio of DPA ligand (Fig. 5.2). The diffraction pattern of all MOFs displayed features compatible with a cubic structure with similar cell parameters, thus proving the generation of a family of iso-reticular structures (Fig. 5.2). The analysis of the powder X-ray diffraction patterns of sample Zr-Tp and Zr-Tp-DPA 20 % collected with synchrotron radiation (Fig. 5.3) allowed the refinement of the crystal structure. The hetero-ligand Zr-Tp-DPA x % MOF microcrystals exhibited cubic crystal structure (Space group $\text{Fm}\bar{3}\text{m}$) with *fcu* topology, which corresponds to that of parent Zr-Tp and Zr-DPA MOFs. Each oxo-hydroxy zirconium-based node presented twelve-fold coordination,

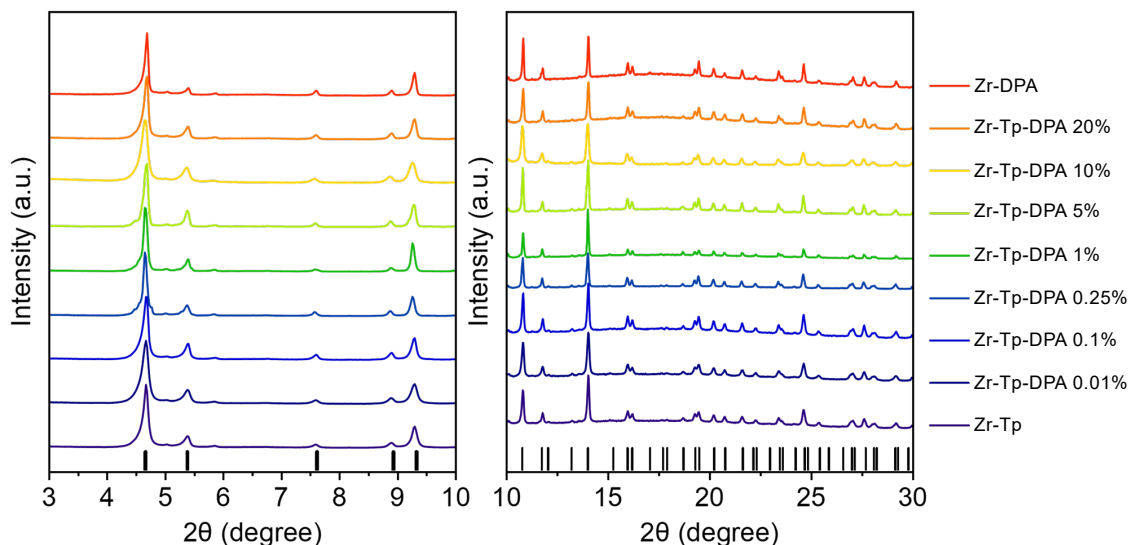
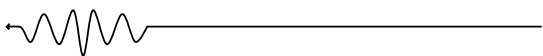


Fig. 5.2: powder X-ray diffraction (PXRD) patterns of sample Zr-Tp:DPA-x%.

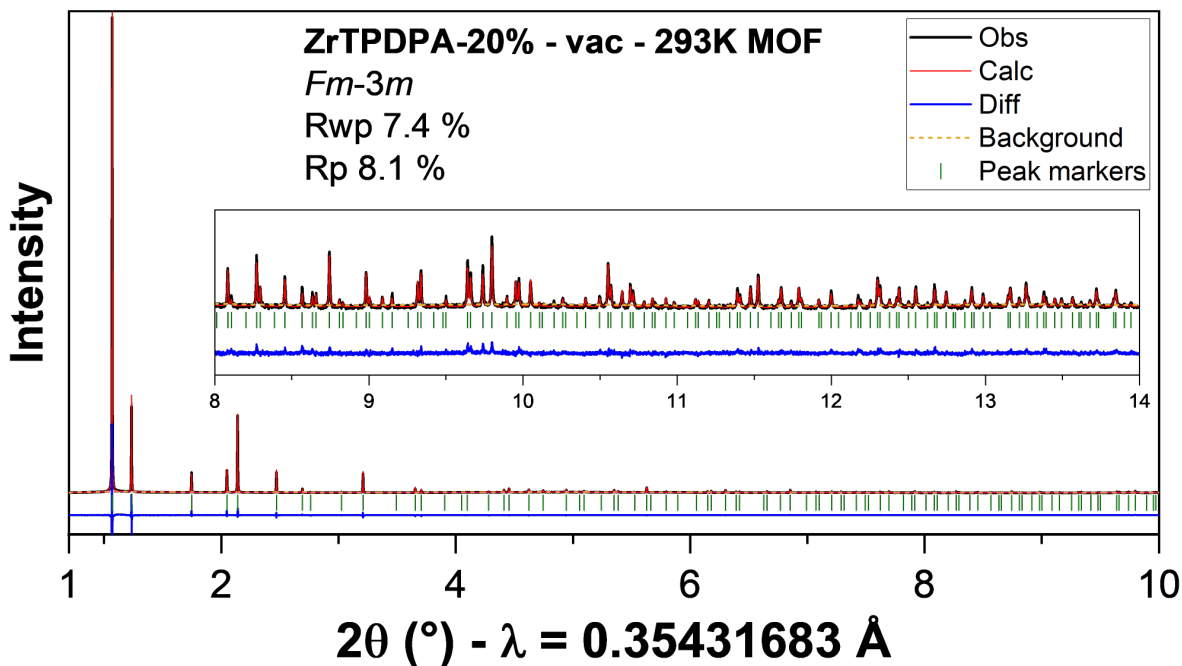


Fig. 5.3: Rietveld refinement of powder X-ray diffraction pattern of Zr-TP:DPA 20 % collected at synchrotron facility (ESRF, Grenoble) between 1° and 10° 2θ degree ($\lambda = 0.35431683 \text{ \AA}$) under dynamic vacuum.

generating a framework endowed with octahedral and tetrahedral cavities interconnected via triangular windows. The nearest neighbour ligands are arranged in an orderly fashion with center-to-center distance of 11.6 \AA and

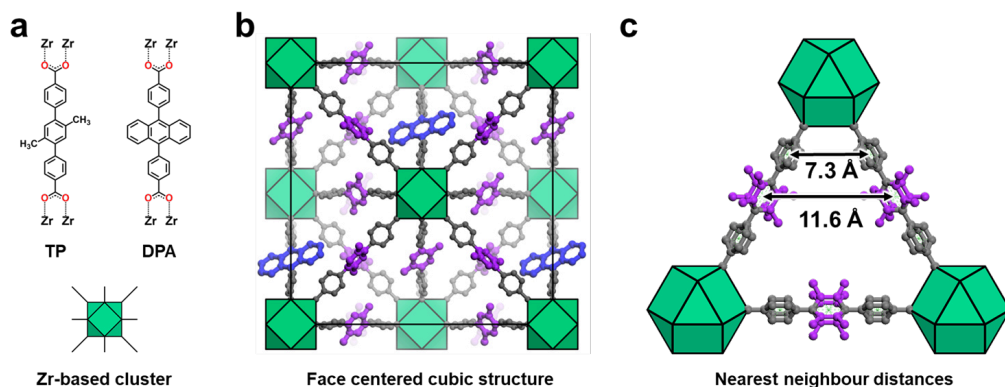
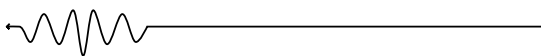


Fig. 5.4: a, Tp and DPA ligands and schematic representation of the zirconium-based oxo-hydroxy cluster. b, Face centered cubic crystal structure of Zr-Tp-DPA x % MOFs. c, Triangular window showing three nearest neighbour ligands with center-to-center distance of 11.6 Å and phenyl-phenyl distance of 7.3 Å.

a close phenyl-phenyl distance of 7.3 Å. The obtained structure is shown in Fig. 5.4. ^1H liquid NMR spectra showed in Fig. 5.5 distinct and well-separated resonances for Tp molecules (δ (ppm) = 8.02), DPA molecules (δ (ppm) = 8.23) and benzoic acid (δ (ppm) = 7.94). The integration of the three signals allowed for the determination of the molar ratio of the different ligands inside MOF structures and for the quantification of benzoic acid (the modulator of the reaction) which is still included inside the structure as benzoate moiety. Optical and electron microscopy techniques revealed highly homogeneous materials composed of microcrystals with well-defined octahedral morphology. A representative example is shown in Fig. 5.5.

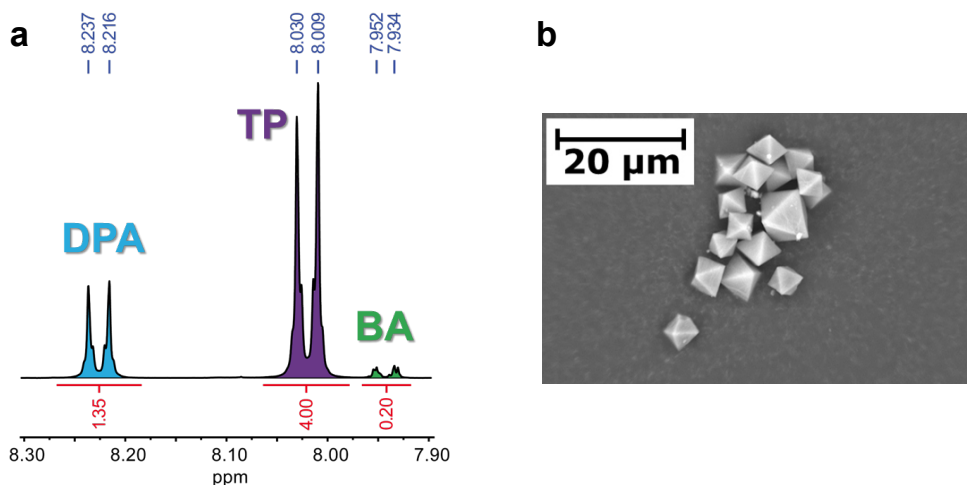


Fig. 5.5: a, ^1H liquid NMR spectrum of Zr-Tp-DPA 20 % and b, SEM images of Zr-Tp-DPA MOFs.

5.2 N₂ adsorption isotherm

Nitrogen adsorption analysis at 77 K (Fig. 5.6) demonstrated the permanent porosity of sample Zr-Tp-DPA-1 %. The adsorption isotherm displayed Langmuir (type I) shape with high uptake at low relative pressures, while it reached a well-defined plateau at higher loadings. The behaviour is consistent with the highly microporous nature of the MOF. The accessible surface area was calculated according to the BET and Langmuir model as high as 3788 m² g⁻¹ and 4172 m² g⁻¹. The pore size distribution calculated according to NLDFT theory and HS-2D-NLDFT Carbon at N₂ 77 K model clearly highlighted two different cavities with sizes of 11.9 Å and 14.8 Å, in very good agreement with the structural information.

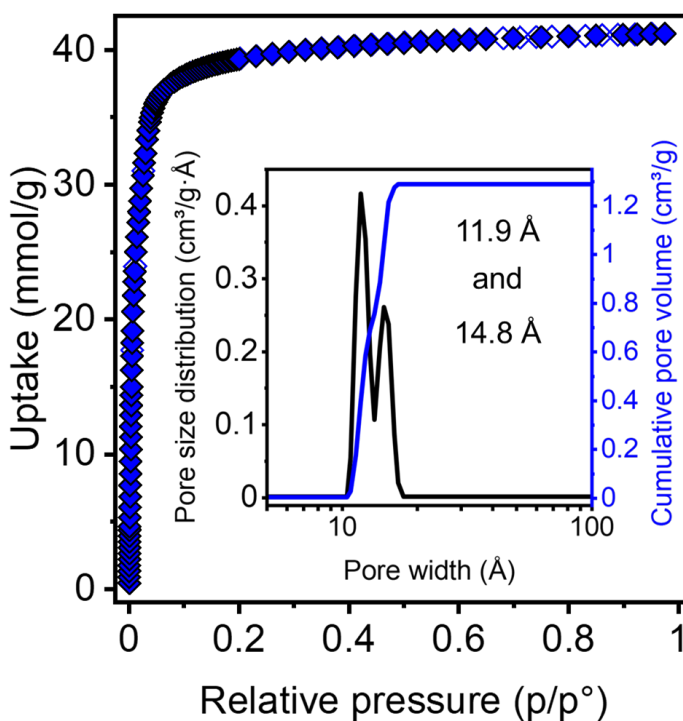


Fig. 5.6: Nitrogen adsorption isotherm of sample Zr-TP:DPA 1 % collected at 77 K. Inset: differential pore size distribution (black line) and cumulative pore size distribution (blue line) calculated according to NLDFT theory and N₂ on carbon slit pore model.



5.3 Zr-Tp-DPA MOFs photoluminescence and scintillation properties

The first properties to be analysed, as for the case of Hf-DPA MOFs, are the properties of the ligands alone. For DPA photoluminescence properties in solution, see paragraph 4.3 of Chapter 4. Here are presented the continuous wave photoluminescence (CW-PL), the absorption profile (ABS) and time resolved photoluminescence (TR-PL) signals of the terphenyl (Tp) molecule excited at 250 nm and collected at 360 nm in a tetrahydrofuran (THF) solution. In Fig. 5.7 it is appreciable, like in the case of DPA, how the time resolved signal of the moieties resembles a full mono-exponential decay with a characteristic lifetime of 1 ns. The quantum yield of Tp has been estimated to be $QY=0.5$, measured relative to a UV emitting standard, the PPO.

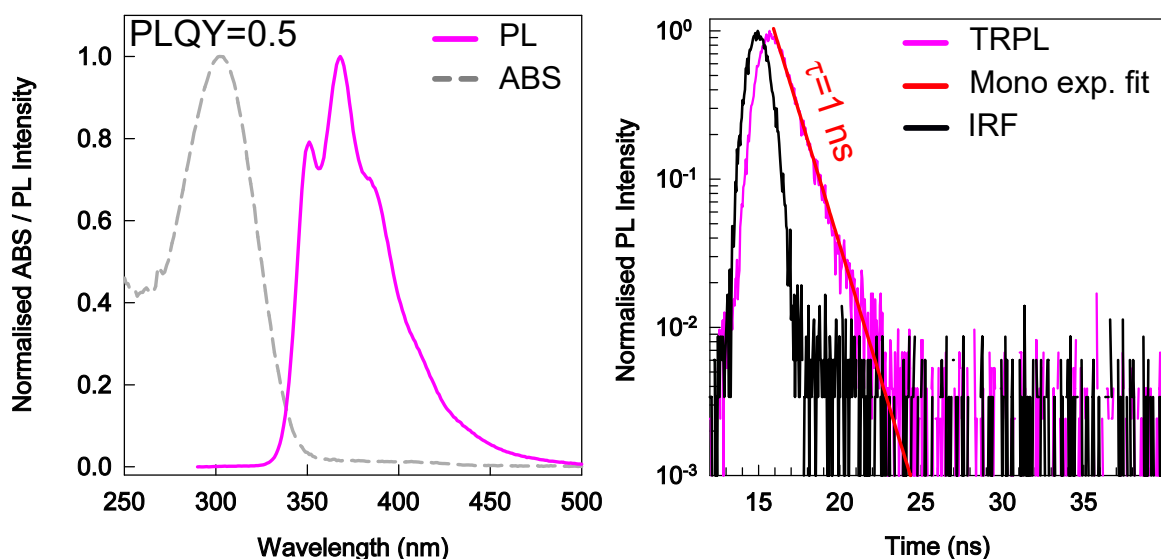
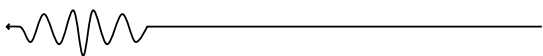


Fig. 5.7: optical properties of Tp dyes in THF solution. The left figure shows the normalised absorption and photoluminescence of the Tp dye while the right figure depicts its characteristic lifetime of 1 ns (excited at 340 nm, collected at 380 nm).

The study of the single molecule properties is essential for the estimation of the final performances in the MOFs architecture. Since the hetero-ligand system has been formulated for the occurrence of the Förster Resonance Energy Transfer (FRET), the first step to better understand this mechanism



in MOFs is to study it in solution, considering the DPA and Tp optical properties. For the occurring of an efficient FRET, the most crucial factor is

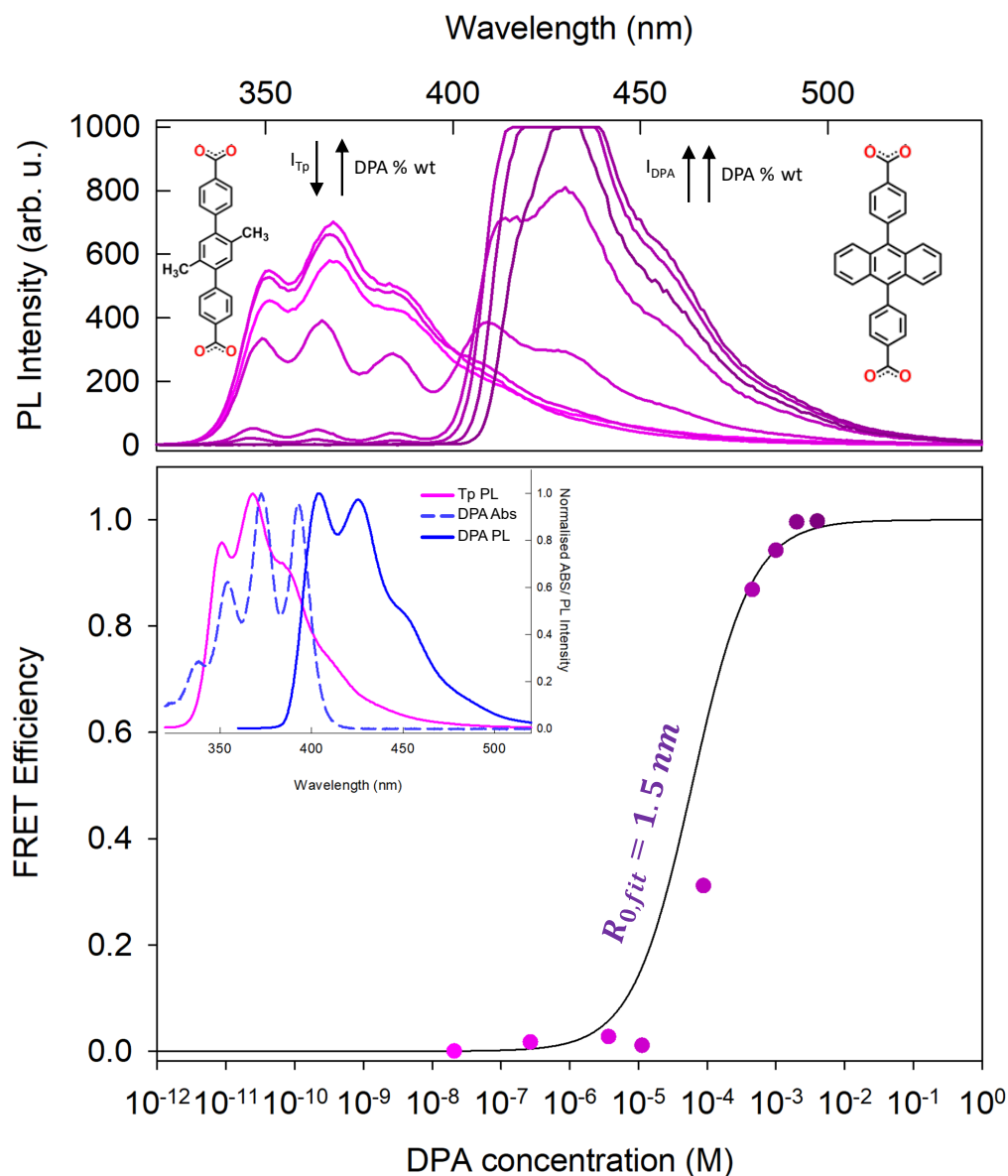


Fig. 5.8: The top panel represents the CW-PL measurements performed on different solution containing the same amount of Tp dye (10^{-4} M) but with different DPA concentrations (from 2×10^{-8} M to 10^{-3} M). Here the way in which the DPA presence increasingly quenched the Tp photoluminescence with the increasing of the DPA concentration is appreciable. The bottom panel shows the efficiency of the resonance energy transfer mechanism at the different DPA concentrations (purple dots) and the sigmoidal fit function (black line) from which it was possible to calculate the resonance radius. The inset shows the optical properties of the two molecules in consideration: the emission of Tp (purple solid line) highly overlapped with the absorption feature of DPA (dashed light blue line) resulting then in the quenching of the first in favour of DPA emission (blue solid line).

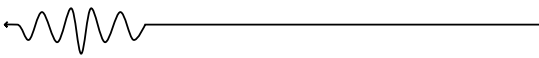


the overlap between the emission of the donor molecule (Tp) and the absorption feature of the acceptor molecule (DPA)³. As seen in previously, FRET is a non-radiative process that belongs to the dipolar interactions field. It is worth noting that it is not a matter of emission and absorption phenomena, but this mechanism is related to the quenching of donors PL in favour of the one of the acceptors by Columbian forces. Thus, FRET is strictly related to the acceptor concentration. The optical features in case of the Tp-DPA couple are represented in the inset in Fig. 5.8. To estimate the Förster interaction radius and the FRET efficiency, the donor PL has been monitored in function of the acceptor concentration ranging from 10⁻⁸ M to 10⁻³ M. Fig. 5.8 shows the CW-PL feature of the solutions containing Tp-DPA dyes excited at 250 nm. By computing

$$\phi_{FRET} = 1 - \frac{I_{D-A}}{I_{D_0}}$$

the efficiency of the transfer mechanism can be calculated, where I_{D-A} is the donor PL intensity at every acceptor concentration and I_{D_0} is the donor PL intensity in absence of acceptor. At the maximum DPA concentration employed (10⁻³ M) the FRET efficiency is 100% with a characteristic Förster radius of 1.5 nm. The study of the dyes properties in solution gives deeper insight and hints on the synthesis of the Zr-Tp-DPA MOFs. Hypothesizing being in the rapid diffusion limit is possible to model how the excitation diffuses in the crystal. Indeed, the exciton moves from a Tp molecule to another until it reaches a surrounding DPA molecule. It is thus essential to calculate the diffusivity of the exciton inside the crystal in order to estimate the DPA doping level necessary to obtain the $\phi_{FRET}=1$ also in solid form. The random diffusion of Tp singlet exciton within the MOF nanocrystals has been modelled as hopping-mediated process occurring between isoenergetic centers, i.e. the framed Tp ligands. Dealing with a 3D isotropic structure, the singlet diffusivity can be calculated as

$$D = m k_{hop}^{Tp-Tp} a^2$$



where $a = 1.2$ nm is the center-to-center Tps distance, K_{hop}^{Tp-Tp} is the rate of the hopping process between a ligands pair and m is the number of equivalent nearest neighbour sites surrounding the exciton. Given the dipole permitted electronic transition involved and considering the short intermolecular distances involved, it is assumed that the hopping is ruled by Förster ET between Tp molecules. By computing

$$R_{FS}^{Tp-Tp} = \left(\frac{9000(\ln 10)\kappa^2 Q_D}{128\pi^5 N n^4} \int_0^\infty \frac{F_D(\lambda)\varepsilon_A(\lambda)\lambda^4 d\lambda}{F_D(\lambda)d\lambda} \right)^{1/6}$$

the Förster radius between Tp molecules is $R_{FS} = 2$ nm. The total hopping rate calculated with $m=6$ and a singlet lifetime $\tau_{Tp} = 1$ ns is then

$$k_{hop}^{Tp-Tp} = 6k_{FRET}^{Tp-Tp} = 6 \frac{1}{\tau_{Tp}} \left(\frac{a}{R_{FS}^{Tp-Tp}} \right)^{-6} = 232 \text{ GHz}$$

This term makes possible to estimate the singlet diffusivity $D = 2.8 \times 10^{-3} \text{ cm}^2 \text{ s}^{-1}$ that leads to a diffusion sphere of radius $L = (6 D \tau_{Tp})^{1/2} = 40$ nm. Interestingly, the Tp singlet exciton is able to reach the DPA in the crystal. The rapid diffusion limit hypothesis is thus sufficient to estimate the amount of acceptor needed for an efficient doping inside the MOF system. On the other hand, it is possible to estimate this percentage by computing the FRET efficiency between Tp-DPA in the solid state and in non-rapid diffusion limit as formulated by Hinokuti H, et al.⁷ :

$$\phi_{FRET} = 1 - \sqrt{\pi} x e^{x^2} (1 - \text{erf}(x))$$
$$x = \frac{1}{2} \sqrt{\pi} \frac{C}{C_0}$$

where C_0 is the critical concentration at which the energy transfer efficiency is equal to 76% that is equal to

$$C_0 = \frac{3}{4\pi R_{FS}^3}$$

Thus, using $R_{FS}=1.5$ nm, the DPA concentration at which the FRET efficiency is at its maximum is $C_{DPA}=2 \times 10^{-4}$ M that it is translated in a DPA

doping level of 17% wt. With this information, Zr-Tp-DPA MOFs have been synthesised by solvothermal synthesis with different DPA concentration, as seen in the previous paragraph, in order to verify the above calculations.

The DPA concentrations employed ranges from 0% (pure Zr-Tp MOFs) wt to 20% wt, as seen in paragraph 5.1. In Fig. 5.10 are presented the photoluminescence measurements performed on the MOFs series with a 250 nm excitation. Interestingly, the energy transfer between Tp and DPA molecules reached the

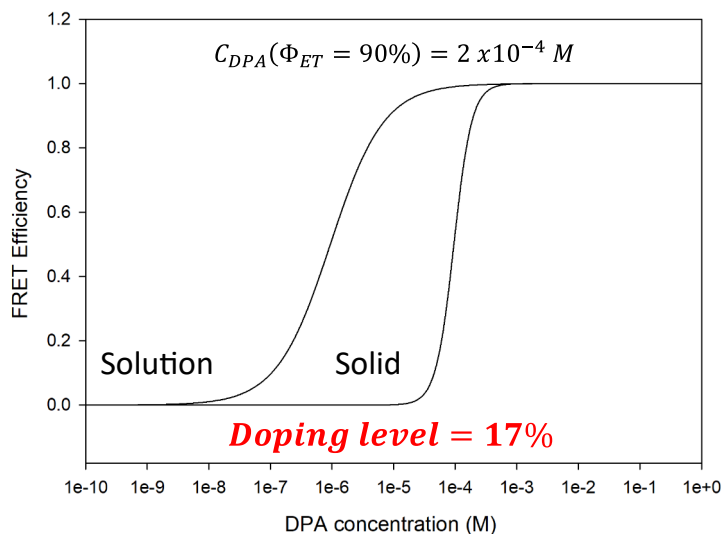


Fig. 5.9: FRET efficiency in function of DPA concentration in the case of the rapid diffusion model and solid state model.

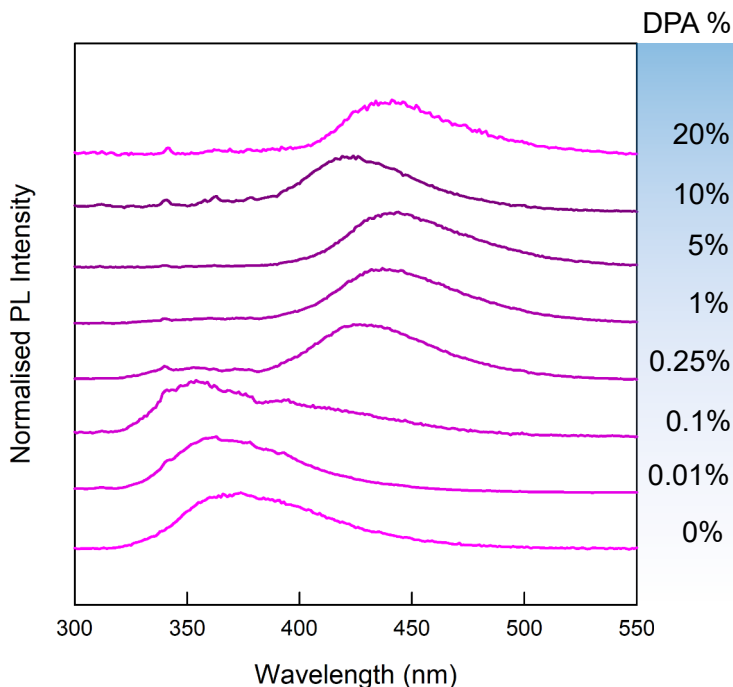


Fig. 5.10: normalised CW-PL spectra of Zr-Tp-DPA MOFs at the different DPA concentrations studied. These measurements were performed by exciting the materials at 250 nm.

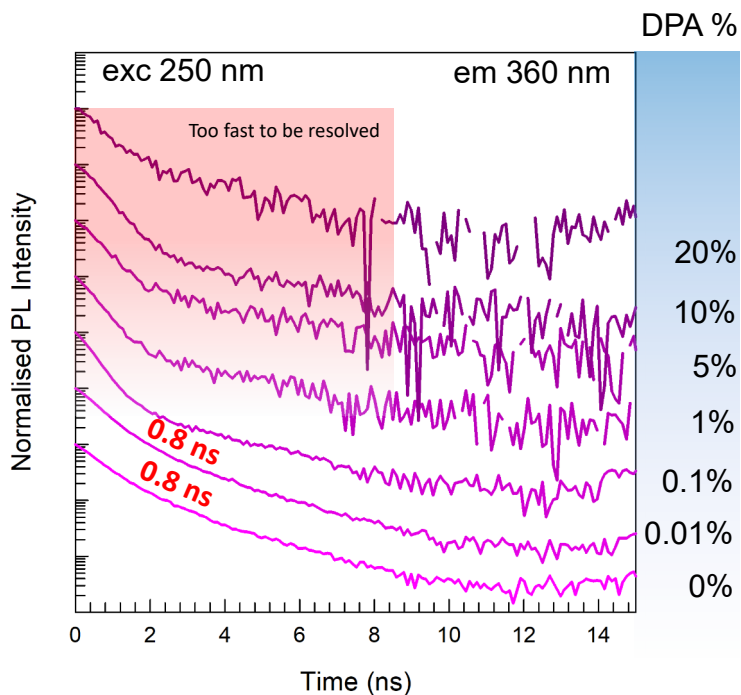
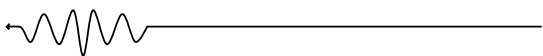


Fig. 5.11: time resolved photoluminescence of Zr-Tp-DPA MOFs at the various acceptor concentrations. The experiments were carried out by exciting the materials at 250 nm and collecting light at 360nm.

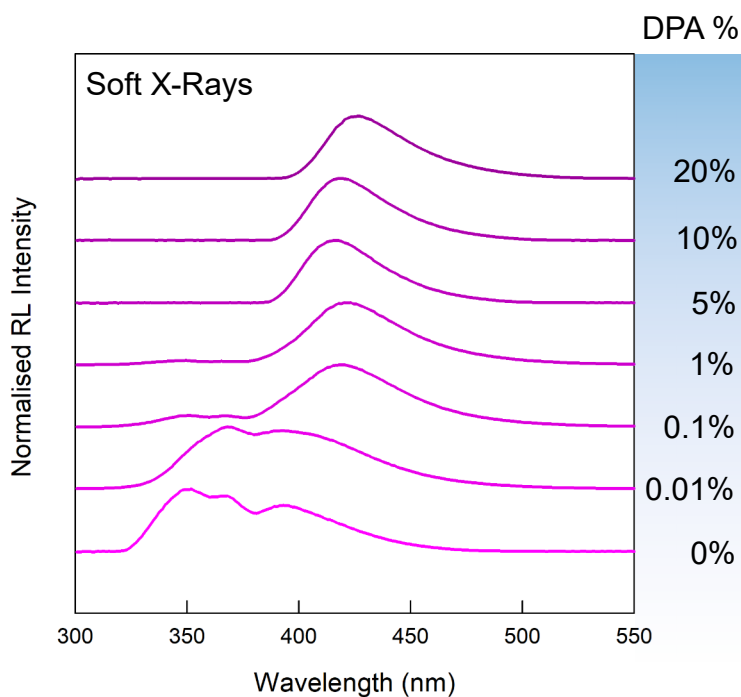


Fig. 5.12: continuous wave RL spectra of Zr-Tp-DPA MOFs samples acquired with 20 kV x-rays.

full efficiency at 1% wt DPA doping, a level that is more than 10 times lower than expected, leaving no trace of the donor emission. This finding is supported by time resolved experiments performed on the materials. Indeed, by monitoring the emission at the T_p maximum (monitored at 360 nm, Fig. 5.11) it is observed a decreasing of the decay time of the molecule that resulted to be quenched at a level that is not possible to be resolved by the instrument. The same can be found by looking at the radioluminescence spectra acquired with soft X-rays (Fig. 5.12). The answer at this problem can be found by modelling the excited state of Tp donor molecules from the absorption features. Indeed, as shown in Fig. 5.14, the orbitals of the excited Tp molecules are strongly delocalized on their long axis. This feature is translated in a shorter effective distance experimented by the molecules in their excited

state making the homo-species energy transfer (i.e. energy transfer between different Tp molecules) more efficient than expected. Indeed, with this kind of delocalization, Tp molecules can be modelled as “closer” one another in comparison with their physical distances enabling the occurring of a rarer energy transfer mechanism, which is the exchange one, also called Dexter energy transfer. This is a fluorescence quenching mechanism that is enabled by the transfer of an excited state electron of a donor to an acceptor^{8,9}. The typical distance of interaction is below 1 nm thus making it very difficult to occur and also to study⁹.

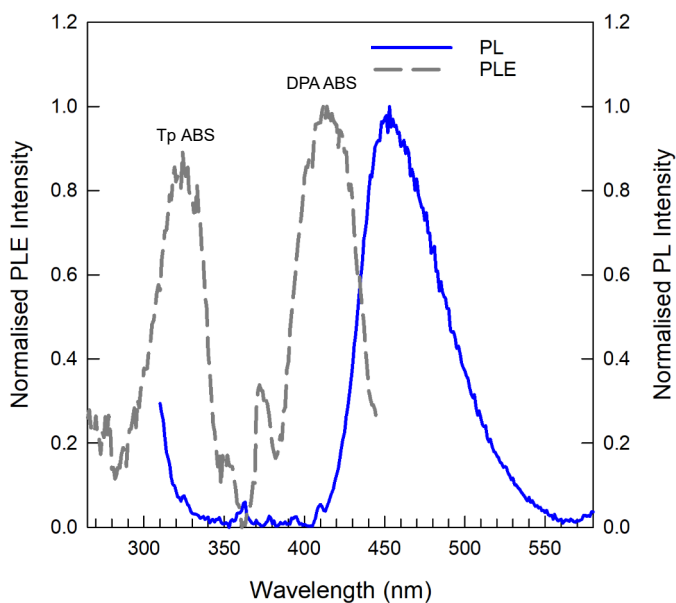


Fig. 5.13: PLE spectra (dashed grey line) and PL spectra (blue solid line) of Zr-Tp-DPA MOFs 1%. The PL profile was acquired by exciting at 300 nm while the PLE spectra was acquired by collecting light at the maximum of emission. Notably, to further prove the presence of the efficient FRET phenomenon, the PLE spectra shows both the contribution of Tp and DPA to the final emission.

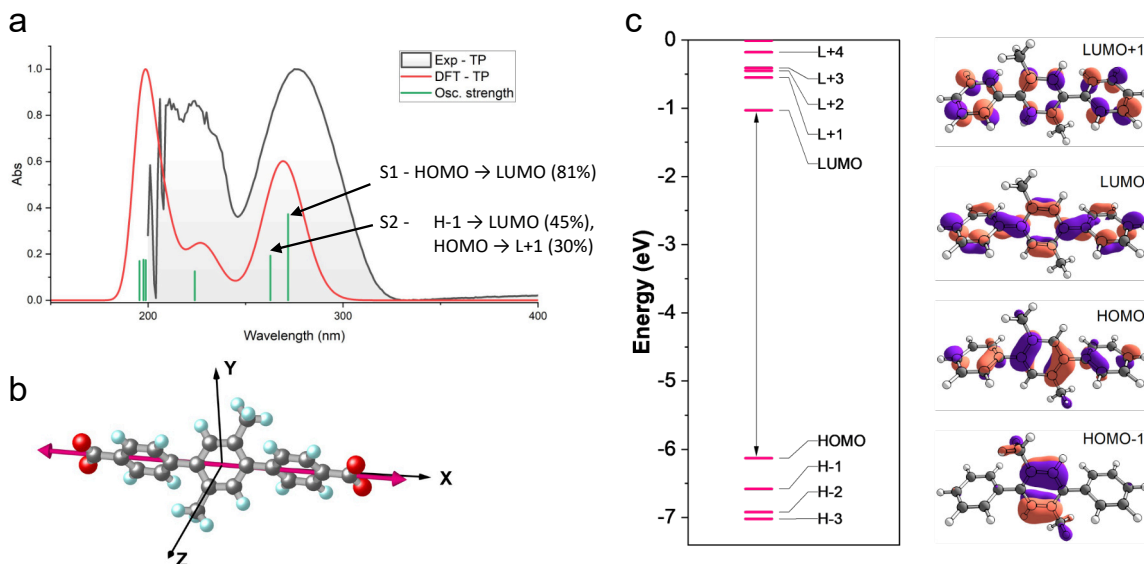
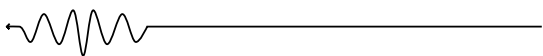


Fig. 5.14: a, study of the Tp energy levels involved in the first transition upon light absorption. b, model of a Tp molecule with the orientation of the transition dipole indicated by a purple arrow. c, modelling of the evolution of the energetic orbitals of Tp molecule upon excitation from the HOMO level to the LUMO level. It is possible to notice that at the LUMO level the electronic density is fully delocalized on the whole molecule.



It is thus supposed to occur in the Zr-Tp-DPA MOFs given the strong delocalization of the Tp excited molecules that can be modelled has a quasi-continuum excited state then enhancing the possibility that the singlet Tp exciton diffuses inside the material reaching a DPA molecule, thus explaining the mismatch between calculation and experiments. At the moment of the writing of this manuscript, experiments are on going in order to demonstrate the occurring of this mechanism . On the other hand, by analysing the RL spectra of Zr-Tp-DPA MOFs relative to the BGO standard, it was possible to extract the light yield data of the crystals. In optimum agreement with the previous analysis, the MOFs crystal containing 1% wt and 5 % DPA reached a light yield close to 4000 ph/MeV (Fig. 5.15), that is striking if it is considered that the density of these materials is well below 1 g cm^{-3} (vs 7.13 g cm^{-3} of the BGO). It is worth noting the excellent agreement between Zr-Tp-DPA MOFs light yield and the lifetime of the materials excited at 250 and monitored at the DPA emission. The longest lifetime corresponds to the highest light yield. To be underlined is the fact that there's no Zr-Tp-DPA x% MOFs configuration in which the lifetime ascribed to the DPA emission is close to the one of the DPA single molecule. This could be due to a most probable concentration quenching mechanism that affects the DPA emission and also to a size distribution effect as seen in Chapter 4 when dealing with Hf-DPA MOFs.

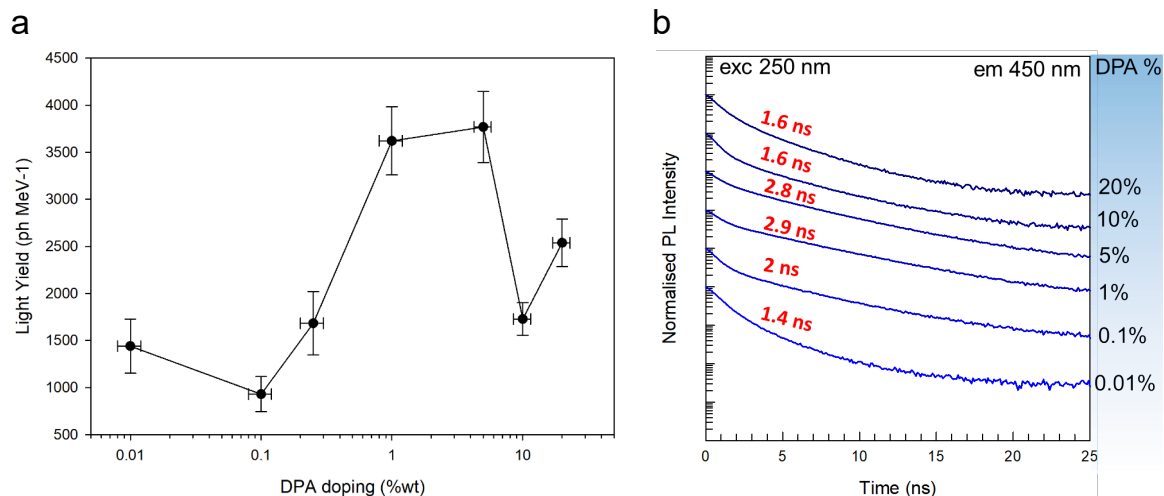


Fig. 5.15: a, light yield measurements of Zr-Tp-DPA MOFs at the various concentration of DPA. The maximum values are reached with 1% wt and 5%wt of DPA. b, Lifetime of Zr-Tp-DPA MOFs collected at the maximum emission and excited at 250 nm.



5.4 Radioactive gas detection by Zr-Tp-DPA MOFs

As for the case of Hf-DPA MOFs studied in Chapter 4, the Zr-Tp-DPA 1% MOFs have been tested with the micro-TDCR device for radioactive gas detection. Unfortunately, the comparison with Hf-DPA MOFs will not be fruitful due to the difference in the atomic number between Zr ($Z=40$) and Hf ($Z=72$). Allowing this comparison will represent an obvious increment in terms of detected photons, due to the higher interaction cross section of hafnium, without giving any chance to understand if the energy transfer strategy employed in Zr-Tp-DPA is beneficial in terms of avoiding self-absorption and matching detector quantum efficiency peak. In this case, a previously studied Zr-DPA MOFs² system has been used to better compare the performances of the hetero-ligand architecture.

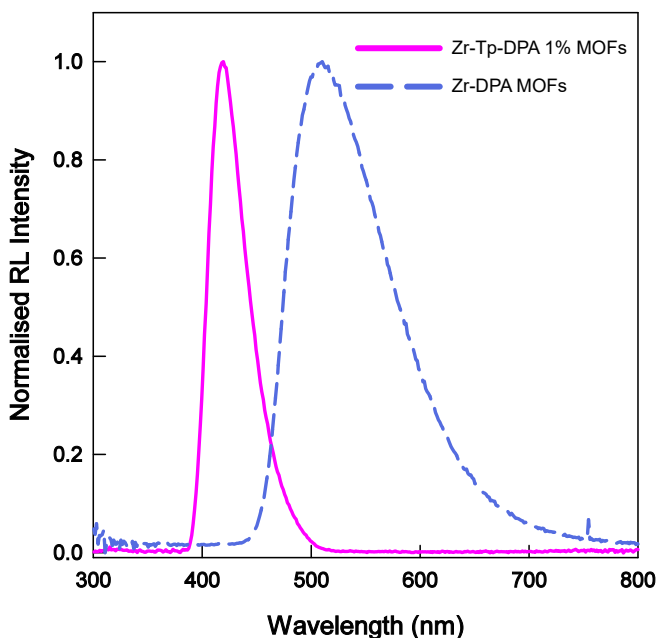
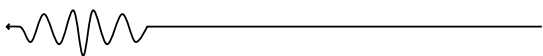


Fig. 5.16: Normalised RL spectra of Zr-DPA MOFs (light blue dotted line) and Zr-Tp-DPA MOFs (purple solid line).

This MOFs has been synthesized following the same procedure seen in paragraph 5.1 but without any donor Tp moieties. The two system presents very similar characteristics from the structural point of view and for what concerns the gas adsorption capabilities. The difference lies in their optical properties. Fig. 5.16 depicts the continuous wave radioluminescence spectra



acquired with soft x-rays. The difference between the two spectra is striking. While from the Zr-DPA MOFs side the RL profile is wide and red shifted in comparison with the pure DPA molecule (symptoms of strong self-absorption and, moreover, of a size distribution suffering), the Zr-Tp-DPA 1% MOFs one better match the PL profile of the ligand, thus confirming the DPA doping procedure as successful strategy to achieve self-absorption free systems. At the moment of the writing of this manuscript, radioactive gas detection measurements were performed utilizing only ^{85}Kr as radioactive isotope. Still, the result confirmed the hypothesis behind the hetero-ligand strategy. Fig. 5.17 depicts the detection counting rate for Zr-DPA and Zr-Tp-DPA 1% MOFs. The increment in detection rate for Zr-Tp-DPA 1% MOFs with the respect to Zr-DPA MOFs is appreciable, leading to a solid +20% of detected photons. Moreover, both in the ascending and descending part of the curves it is possible to observe the same slow dynamics observed in the Hf-DPA MOFs sample. As the previous case, this finding proven another time the microporosity of the system as well as the diffusion of gaseous species like ^{85}Kr within the framework also demonstrating the efficiency of the synthetic pathway in generating nano- and microcrystals with similar properties and behaviour.

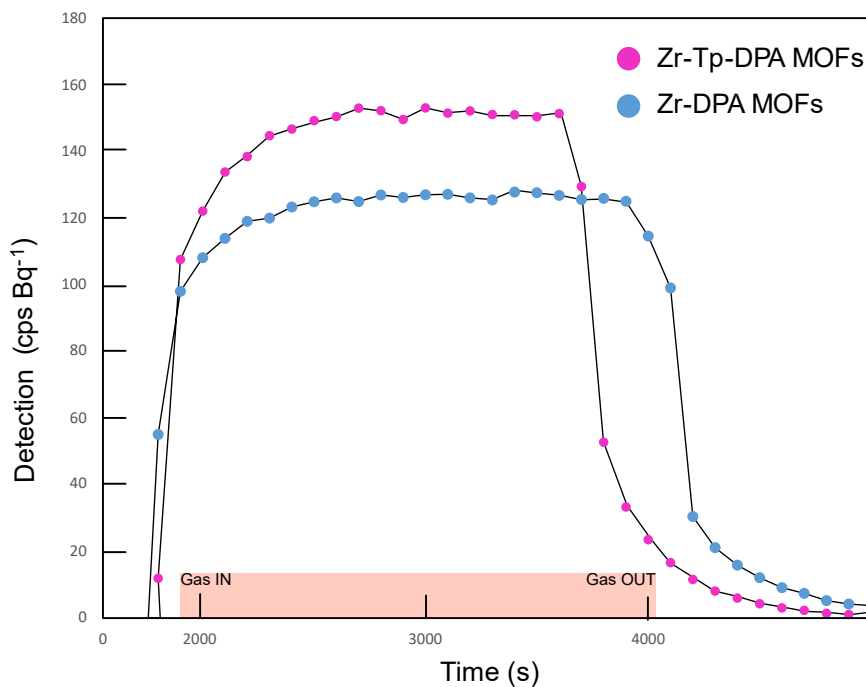
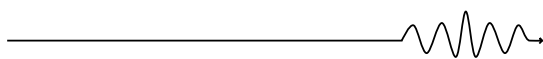


Fig. 5.17: Coincidence detection of ^{85}Kr by Zr-DPA MOFs (blue dots) and by Zr-Tp-DPA MOFs (purple dots).



These findings, together with the CW-PL, TR-PL and scintillation properties, strongly support the use of hetero-ligands system as self-absorption free materials and lay the foundation for a new generation of solid porous scintillators to be employed in environmental safeguarding and human-related safety issues.

5.5 Methods

Nuclear magnetic resonance (NMR) spectroscopy

^1H -NMR spectra were recorded on a AVANCE NEO Bruker instrument (400 MHz).

Powder X-ray diffraction

PXRD measurements of Zr-Tp-DPA-x% MOFs were collected with a Rigaku Smartlab powder diffractometer over a range for 2θ of $3.0 - 50.0^\circ$ with a step size of 0.02° and a scan speed of $1.0^\circ \text{ min}^{-1}$ using Cu-K α radiation, 40 kV and 30 mA.

Synchrotron radiation PXRD experimental conditions

Samples were prepared and sealed in 0.5 mm Lindeman capillaries for XRD experiments at the ESRF ID22 beam line using a 0.354 Å wavelength. PXRD measurements were collected over a range of $0.0 - 32.0^\circ$ with a data collection interval of 0.002° and data collection was done over 12 detectors simultaneously. The scan speed may vary depending on sample degradation. Data were collected on various spots along the capillary and multiple times on the same spot. Any scans which showed signs of degradation were excluded from the final merged and binned data set. For experiments under gas pressure, the capillaries were connected to pressure cell that is connected to a gas manifold for which the pressure could be precisely controlled. Two spots on a particular capillary were collected first under vacuum after in-situ activation to confirm the activated structure before loading the capillary with 1 bar of xenon gas at 293 K. The pressure was monitored throughout the experiment.

General Computational Details for Materials Studio Software Suite.

The Zr-TP model for the Rietveld refinement was generated from our previously published Zr-DPA structure, replacing the anthracene organic centre with a dimethyl-phenyl ring. The unit-cell dimensions and all atomic coordinates were optimized as part of a periodic system in R-3 using the CASTEP module of the Materials Studio software suite. The R-3 space group is the smallest unit-cell with the highest symmetry that could produce the Zr-TP MOF structure without any disorder. The optimizations were



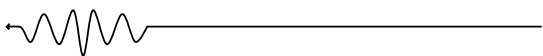
performed using the GGA PBE functional with Grimme's DFT-D dispersion correction, and thresholds for geometry optimization and SCF convergence were chosen as 2×10^{-6} eV. For the Rietveld refinement, the structure was converted to a disordered cubic system in the Fm-3m space group while maintaining the molecular geometries. Single point energy calculations were performed using the GGA PBE functional, and threshold for SCF convergence were chosen as 1×10^{-6} eV. The calculated Milliken charges were applied to the model for molecular mechanics (MM) calculations.

PW-DFT structural resolution and Rietveld Refinement

Rietveld structural refinements of the X-ray data were performed using the TOPAS-Academic64 V6 software package. For the final Rietveld refinement, the structure was modelled as a disordered system with a space group Fm-3m. The background was fitted and refined using a Chebyshev polynomial with 20 coefficients in the PXRD trace range from 0.5° to 20° 2-theta with baseline shift refinement. The "Simple_Axial_Model" was used to account for the asymmetry in the peaks, especially at low 2-theta values, which are a result of the geometry of the XRD setup of the ID22 beamline at the ESRF. The peaks were fitted using a PearsonVII " PVII " function.

General Computational Details for GASSIAN16

All calculations were performed using Gaussian16 on the GALILEO100 HPC system at CINECA in Bologna, Italy. Calculation were performed at B3LYP/6-31+(d,p) level of theory with Grimme-D3 empirical dispersion correction. The calculation was run with the SCF=XQC which adds an extra quadratically convergent SCF procedure to aid in the SCF convergence. All calculations were performed using the TP moiety without the carboxylates. Full geometry optimization of the was followed by frequency calculations to ensure the absence of imaginary frequencies and that a true minimum has been reached then the frontier orbitals were extracted and visualized. UV-Vis calculations were performed using TD-B3LYP/6-31+(d,p) level of theory with Grimme-D3 empirical dispersion correction for the first 40 excited states. The calculated UV-Vis spectrum was generated using gaussian peak functions fitted to the oscillator strength for the electronic transitions. The output also gives the orbitals involved for each transition as well as the



electronic transition dipole moments for each transition. This analysis shows the relevant frontier orbitals, that participate in the absorption region of interest, to be visualized.

Scanning electron microscopy (SEM) and energy-dispersive spectroscopic analysis (EDS).

Scanning electron microscopy (SEM) images were collected using a Zeiss Gemini 500 microscope, operating at 5 KV and a working distance of 4.7 mm. The sample was deposited on a silicon slide from 2-propanol dispersion, dried under high vacuum and sputtered with gold before the analysis (10 nm, nominal thickness). Particle size distributions were measured from SEM images using ImageJ software. The linear dimensions of nanocrystals have been evaluated over more than 100 particles to determine the particle size distribution.

Gas adsorption properties

N₂ and Ar adsorption isotherms at 77 K were collected up to 1 bar using a Micromeritics analyser ASAP2020 HD. N₂ isotherms at 77 K were fitted using Langmuir and BET models and surface areas were calculated in the range from 0.015 to 0.08 p/p° (radii of N₂ = 0.162 nm, Ar = 0.1940 nm and Kr = 0.207 nm). Pore size distributions (PSD) were calculated according to Non-Local Density Functional Theory (NLDFT) model.

Photoluminescence studies

Absorption spectra were recorded using a Cary Lambda 900 spectrophotometer at normal incidence with Suprasil quartz cuvettes with a 0.1 cm optical path length and an integrating sphere to eliminate scattering effects. Steady-state photoluminescence spectra were acquired using a Varian Eclipse fluorimeter (bandwidth 1 nm) using quartz cuvettes of 0.1 cm optical path length. Time-resolved photoluminescence spectra of the MOFs dispersions were recorded monitoring the emission decay of the samples at 360 nm and 450nm. The MOFs were excited with a pulsed light-emitting laser diode at 250 nm (3.65 eV, pulse width 80 ps; EP-LED 250, Edinburgh Instruments). Photoluminescence decay times were measured at the maximum of the emission spectrum. The time resolved photoluminescence (PL) spectra and scintillation data discussed in the main text show in general



a complex behaviour. The signal decay has been reproduced with an analytical multi-exponential function:

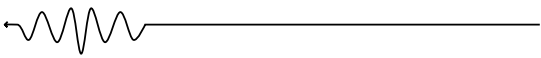
$$I_{\text{RL}}(t) \propto \sum A_i e^{-\left(\frac{t}{\tau_i}\right)}$$

The characteristic emission lifetime τ_{avg} has been calculated as the weighted average of the characteristic decay time for each i -exponential function by:

$$\tau_{\text{avg}} = \frac{\sum_i A_i * \tau_i}{\sum_i A_i}$$

Radioluminescence and scintillation studies

The samples were excited by unfiltered X-ray irradiation using a Philips PW2274 X-ray tube, with a tungsten target, equipped with a beryllium window and operated at 20 kV. At this operating voltage, X-rays are produced by the Bremsstrahlung mechanism, superimposed to the L and M transition lines of tungsten due to the impact of electrons generated through a thermionic effect and accelerated onto the tungsten target. Cryogenic radioluminescence measurements are performed in the 10–370 K interval. Radioluminescence has been recorded on powder samples of 1 mm thickness in an aluminium sample holder. For comparison the radioluminescence spectra has been normalized by the mass of the investigated powder. Scintillation has been recorded under pulsed X-rays with energies up to 25 keV generated with a repetition rate of 1 MHz by a picosecond diode laser at 405 nm (Delta diode from Horiba) focused on an X-ray tube (model N5084 from Hamamatsu). The resulting photons were collected by Kymera spectrograph (ANDOR) and detected by a hybrid PMT 140-C from Becker and Hickl GmbH. For decay-time measurements, the photons were histogrammed using a PicoHarp300 time-correlated single-photon counting (32 ps time per bin) and for the time resolved spectra a MCS6A multiple-channel time analyzer was used (800 ps time per bin). Subnanosecond scintillation emission kinetics of the samples were measured with a time-correlated single-photon counting set-up.



Radioactive gas detection experiments

The experiments are performed using a unique gas bench developed at the CEA, Paris-Saclay, and by allowing the production of radioactive gas atmospheres using high activity standards. Different sampling and dilution steps allow for precise control of the injected activity, and precise knowledge of the volumetric activity of each gas: at best, the relative standard uncertainty on the activity concentration is 0.4%, 0.6% and 0.8% for ^{222}Rn , ^{85}Kr and ^3H , respectively. For each experiment, the same type of three step sequence is performed. First, the measurement of the blank, by circulating clean air without additional radioactivity. Second, the measurement of scintillation by circulating the radioactive gas sample into the vial (4 mm diameter and 50 mm height, 0,1086 g for Hf-DPA and 0.3640 for polystyrene microspheres, activity 10 kBq). Third, circulation of clean air into the device to remove the radioactive gas. The light photons produced by scintillation are measured using a metrological device developed to exploit the triple-to-double coincidence ratio, with a specific connection cap adapted to the radioactive gas flow in the scintillator.



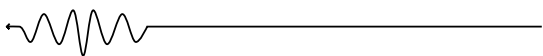
5.6 References

1. Perego, J. et al. Highly luminescent scintillating hetero-ligand MOF nanocrystals with engineered Stokes shift for photonic applications. *Nat Commun* **13**, (2022).
2. Perego, J. et al. Composite fast scintillators based on high-Z fluorescent metal–organic framework nanocrystals. *Nat Photonics* **15**, 393–400 (2021).
3. Lakowicz, J. R. Principles of fluorescence spectroscopy. (Springer, 2006).
4. Thomas, D. D., Carlsen, W. F. & Stryer, L. Chemistry Fluorescence energy transfer in the rapid-diffusion limit (Forster transfer/spectroscopic rulers/terbium/membrane vesicles). vol. 75 (1978).
5. Grosjean, S., Hassan, Z., Wöll, C. & Bräse, S. Diverse Multi-Functionalized Oligoarenes and Heteroarenes for Porous Crystalline Materials. *European J Org Chem* **2019**, 1446–1460 (2019).
6. Jiang, H. L., Feng, D., Liu, T. F., Li, J. R. & Zhou, H. C. Pore surface engineering with controlled loadings of functional groups via click chemistry in highly stable metal-organic frameworks. *J Am Chem Soc* **134**, 14690–14693 (2012).
7. Inokuti, M. & Hirayama, F. Influence of energy transfer by the exchange mechanism on donor luminescence. *J Chem Phys* **43**, 1978–1989 (1965).
8. Skourtis, S. S., Liu, C., Antoniou, P., Virshup, A. M. & Beratan, D. N. Dexter Energy transfer pathways. *Proc Natl Acad Sci U S A* **113**, 8115–8120 (2016).
9. Dexter, D. L. A theory of sensitized luminescence in solids. *J Chem Phys* **21**, 836–850 (1953).



CONCLUSIONS

In summary, specific scintillating porous MOF crystals to detect radioactive noble gases were designed and fabricated. To achieve the goals fixed by the SPARTE project (Chapter 2), two strategies were followed. The first one was the use of hafnium-based MOF crystals exploiting the fast luminescence of the DPA organic ligand. Their good luminescence and scintillation properties—combined with their characteristic porosity allowed to realize a fully operative prototype detector. An intensive study on a broad range of critical β -emitting radioactive gases was performed, namely, the low-energy β -emitter ^3H , the high-energy β -emitter ^{85}Kr , and the β/α -emitter ^{222}Rn . The MOF crystals exhibited improved performance compared with commercial powder-like materials currently tested. Moreover, ^{85}Kr can be detected with excellent sensitivity down to radioactivity values below the limit of commercial systems. The second strategy concerned the engineering of the composition of co-assembled hetero-ligand MOF nanocrystals obtaining efficient and fast emitters with a large Stokes shift. Thanks to the high-rate energy transfer mechanisms (both dipolar and exchange-related) occurring in the highly ordered crystalline framework between the different species of fluorescent ligands, a significant Stokes shift as large as 130 nm was achieved. Therefore, zirconium-based MOFs were synthesized exploiting the particularly matching spectral characteristics of terphenyl dye (donor) and diphenyl anthracene chromophore (acceptor). This makes these new emitters ideal candidates for reabsorption-free photonic applications that require fast timing response. An excellent light yield close to 4000 ph/MeV was observed directly related to the success of the synthetic strategy employed to couple complementary, fluorescent acene-based building blocks in a MOF architecture. From the radioactive gas detection side, ^{85}Kr



was successfully detected with a 20% improvement of the material response if compared to Zr-DPA MOFs crystals, which were synthesised in absence of the donor terphenyl dye. The obtained results are therefore stimulating not only from the scientific point of view, as radionuclide detection using porous scintillators has been demonstrated here for the first time, but also from the technological perspective, hinting at a potential breakthrough by developing conceptually new optimized universal devices that allow detecting all the gas radionuclides species of interest. In this regard, it is worth pointing out that MOFs powders cannot easily be used in the present form due to the practical problems of handling, especially from the perspective of industrial production. The future work is then centred on the realization of a hierarchical porous architecture in which porous MOFs are homogeneously distributed in a porous polymeric host endowed with mesopores and macropores suitable for gas diffusion. In such a configuration, the MOFs will be employed to further concentrate and detect the radionuclides, thus realizing the first example of composite bulk porous scintillators for radioactive gas detection. Moreover, in order to push forward the response in mixed systems like Zr-Tp-DPA MOFs, a natural evolution will be to replace the zirconium cluster with the much heavier hafnium, in order to benefit of both the enhancement due to the higher interaction cross section and the one due to the high Stokes shift. Similarly, the instrumental design will be improved to get a more functional device. A possible evolution can be the use of a cylindrical shape container for the porous scintillator with aerosol filters as the entrance and exit face, in which the gas flow would circulate freely through the whole porous material, placed vertically between two photomultipliers. In such a configuration, the gas flow will be orthogonal to the detection line while diffusing through the whole scintillator, thus maximizing the radionuclide accumulation and the scintillation detection yield. The combination of easy-to-handle hierarchical porous scintillators and excellent detection properties of porous MOFs with an optimized instrumental design will provide a pivotal step forward in the fabrication of high-tech ultrasensitive and reusable detectors, especially for low-energetic radionuclides such as tritium produced in nuclear plants.

This page was intentionally left blank.

This page was intentionally left blank.



TDCR PRINCIPLE

The following paragraph has the intention of briefly explain the basics behind the Triple-to-Double Coincidence technique and it is taken by the article of R. Broda (“A review of the triple-to-double coincidence ratio (TDCR) method for standardizing radionuclides”, 2003, [https://doi.org/10.1016/S0969-8043\(03\)00056-3](https://doi.org/10.1016/S0969-8043(03)00056-3)). Specifically, he was one of the first to theorize and apply this technique to liquid scintillation counting. Above the logic system behind the TDCR technique is resented:

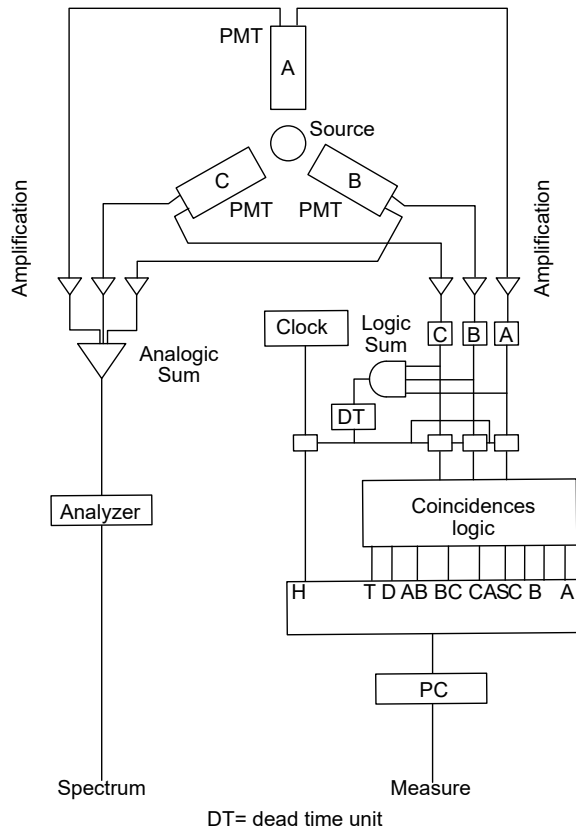


Fig. A1: schematics of a general TDCR system.

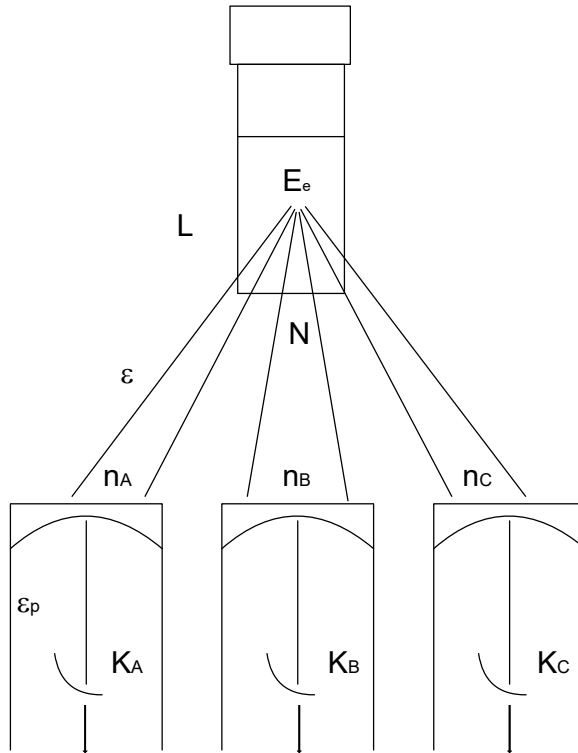
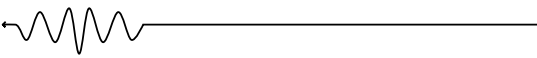


Fig. A2: dynamics of TDCR system.

Fig. A2 shows the dynamics of the detection of photons in a triple coincidence system. Here is presented the generation of $N = LF(E_e) E_e/h\nu$ photons; the total number of electrons reaching the PMTs is $m = n_a + n_b + n_c$ and is given by a Poisson distribution $d_1 = p(m; N\xi)$ where ξ is the light collection efficiency. Photons reach each PMT with a probability of appearance of a definite set of number $(n_a n_b n_c)$ given by a trinomial distribution $d_2 = m!/(n_a! n_b! n_c! 3^m)$ with probability 1/3. The probability that n photons cause the emission of k photoelectrons is given by a binomial distribution $d_3 = b(k; n, \epsilon_p)$ where $b(k; n, \epsilon_p)$ is the efficiency of the PMT and the parameter of the distribution. $b(0; n, \epsilon_p)$ is assumed to be the non-detection probability so, $p_b(n) = 1 - b(0; n, \epsilon_p) = 1 - (1 - \epsilon_p)^n$ is the detection probability. The probability of the formation of an output pulse is $p_x = f[p_b(n_a), p_b(n_b), p_b(n_c)]$. Finally, the counting probability is

$$P_E = \sum_m \sum_{n_a} \sum_{n_b} d_1 d_2 p_x.$$



Assuming that the light yield follows the Birks law: non linearity of scintillation response due to different phenomena like ionization quenching and local density energy distribution:

$$m(E) = \int_0^E \frac{A dE}{1 + kB \frac{dE}{dx}}$$

where A is the activity of the sample. Since the frequencies of triple and double coincidences are observed experimentally and considering that, for a large sample, the ratio of frequencies converges to the ratio of probabilities, the calculation algorithm consists in finding the free parameter A, such that :

$$TDCR = \frac{\# \text{ Triple coincident events}}{\# \text{ Double coincident events}}$$



Hf-DPA MOFs SIZE MODULATION

Here are presented the SEM images of Hf-DPA MOFs samples obtained with different sizes with an increasing amount of formic acid, used as modulator. Moreover, Table A represents the average size for every sample with indicated the monitored quantum yield.

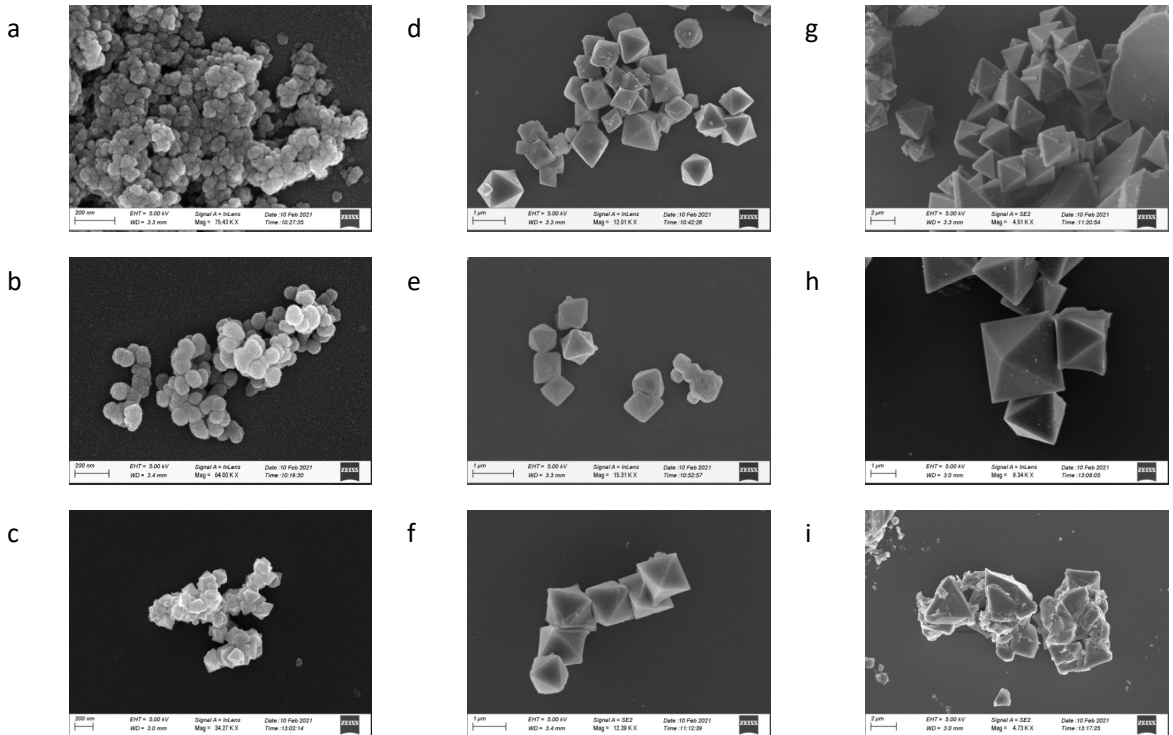
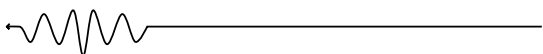


Fig. B1: SEM images of Hf-DPA MOFs with different size. The size increase from a to i with this order: a, b, c, d, e, f, g, h, i.



sample	size	surface/volume (nm ⁻¹)	simmetry	QY
a	60 ± 8 nm	0.0158	spherical	0.6956
b	95 ± 17 nm	0.0241	spherical	0.3511
c	175 ± 25 nm	0.0565	octahedral	0.4053
d	1025 ± 200 nm	8.4111e-3	octahedral	0.4612
e	930 ± 110 nm	0.0108	octahedral	0.3552
f	870 ± 90 nm	0.0204	octahedral	0.4138
g	4200 ± 600 nm	4.2543e-3	octahedral	0.4338
h	3500 ± 400 nm	5.1020e-3	octahedral	0.4738
i	5200 ± 690 nm	3.4201e-3	xxxxxx	0.6244

Table A: from left to right, the first column after the sample name represents the MOFs increasing sizes, then surface to volume ratio for every sample is presented as well as the symmetry. The last column represent the value of QY recorder for each samples, measured relative with DPA.

This page was intentionally left blank.








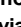



Efficient radioactive gas detection by scintillating porous metal–organic frameworks

Received: 15 November 2022

Accepted: 7 April 2023

Published online: 18 May 2023

 Check for updates

Matteo Orfano ^{1,5}, Jacopo Perego^{1,5}, Francesca Cova ¹,
Charl X. Bezuidenhout ¹, Sergio Piva ¹, Christophe Dujardin ²,
Benoit Sabot ³, Sylvie Pierre³, Pavlo Mai², Christophe Daniel ⁴,
Silvia Bracco ¹, Anna Vedda ¹✉, Angiolina Comotti ¹✉ &
Angelo Monguzzi ¹✉

Natural and anthropogenic gas radionuclides such as radon, xenon, hydrogen and krypton isotopes must be monitored to be managed as pathogenic agents, radioactive diagnostic agents or nuclear activity indicators. State-of-the-art detectors based on liquid scintillators suffer from laborious preparation and limited solubility for gases, which affect the accuracy of the measurements. The actual challenge is to find solid scintillating materials simultaneously capable of concentrating radioactive gases and efficiently producing visible light revealed with high sensitivity. The high porosity, combined with the use of scintillating building blocks in metal–organic frameworks (MOFs), offers the possibility to satisfy these requisites. We demonstrate the capability of a hafnium-based MOF incorporating dicarboxy-9,10-diphenylanthracene as a scintillating conjugated ligand to detect gas radionuclides. Metal–organic frameworks show fast scintillation, a fluorescence yield of ~40%, and accessible porosity suitable for hosting noble gas atoms and ions. Adsorption and detection of ⁸⁵Kr, ²²²Rn and ³H radionuclides are explored through a newly developed device that is based on a time-coincidence technique. Metal–organic framework crystalline powder demonstrated an improved sensitivity, showing a linear response down to a radioactivity value below 1 kBq m⁻³ for ⁸⁵Kr, which outperforms commercial devices. These results support the possible use of scintillating porous MOFs to fabricate sensitive detectors of natural and anthropogenic radionuclides.

Natural radioactive gases such as the isotopes of radon (²²²Rn and ²²⁰Rn), and the anthropogenic radionuclides coming from fission (¹³³Xe and ⁸⁵Kr) and activation (³H and ³⁷Ar) products, need to be carefully monitored. Isotopes such as ⁸⁵Kr and ³H, which originate from nuclear

power plants, reprocessing plants and nuclear waste treatments^{1–5}, are critical to detect for monitoring nuclear activity and uncovering illegal reprocessing to produce plutonium for weapons⁶. ¹³³Xe and ³⁷Ar are of key interest, as they can be used to detect covert activities to

¹Dipartimento di Scienza dei Materiali, Università degli Studi Milano-Bicocca, Milan, Italy. ²Institut Lumière Matière, Université Claude Bernard Lyon, Lyon, France. ³Université Paris-Saclay, CEA, LIST, Laboratoire National Henri Becquerel (LNE-LNHB), Palaiseau, France. ⁴Nano Active Film SRL, Dipartimento di Chimica e Biologia, Università degli Studi di Salerno, Fisciano, Italy. ⁵These authors contributed equally: Matteo Orfano, Jacopo Perego. ✉ e-mail: anna.vedda@unimib.it; angiolina.comotti@unimib.it; angelo.monguzzi@unimib.it

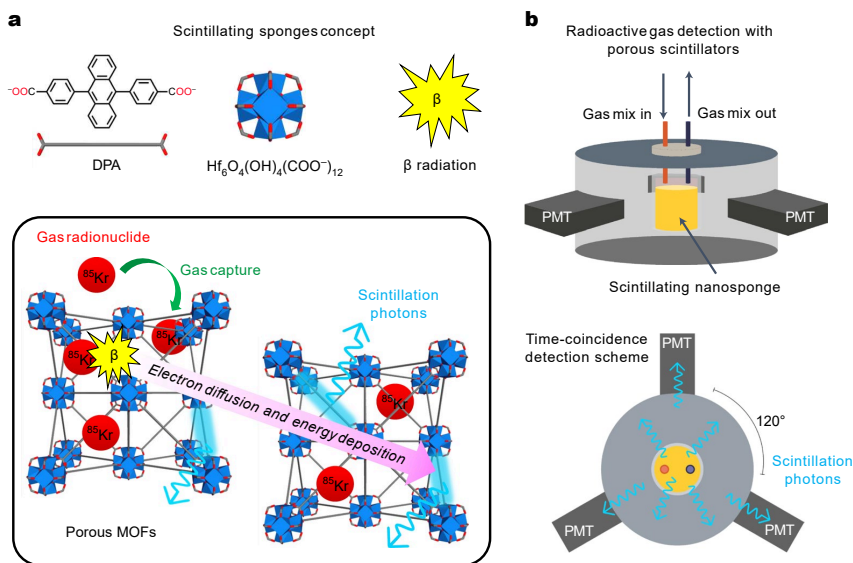


Fig. 1 | Time-coincidence-based detector for radionuclide gases exploiting porous scintillators. a, Schematic representation of the scintillation mechanism inside a porous hafnium-based MOF. The porous framework can uptake radioactive gaseous species through physical adsorption and concentrate them inside the pores. The decay process produces β -particles that can effectively interact with the porous particles during their diffusion and thermalization, triggering gas sensitized scintillation process. The ligand and metal node that constitutes Hf-DPA, as well as the β -radiation emitted by radionuclides, are

shown at the top. **b**, Sketch of the triple-coincidence system designed to reveal radioactive gases by exploiting a porous scintillator. The porous material is placed in the central chamber where it adsorbs the flowing gas molecules, whose β -decay produces high-energy electrons in the pores. The interactions of electrons with the walls of the pores generate the light pulses to be recorded by three symmetric PMTs employed to have a low-noise, time-coincidence detection.

verify compliance with the Comprehensive Nuclear-Test-Ban Treaty⁷. On the other hand, gases from granite-rich areas (^{222}Rn and ^{220}Rn)^{8–10} are pathogenic agents that must be quantified to mitigate the exposure risk, whereas xenon isotopes are useful as radioactive diagnostic contrast agents to evaluate pulmonary function, lung imaging and cerebral blood flow by inhalation^{11–13}. The detection and radioactivity metrology of gases is thus a crucial aspect in a modern, technologically advanced and sustainable society, as demonstrated by the recurrent updates of regulations that ask for increasingly more sensitive and accurate detectors^{14,15}.

All of the listed radionuclides decay by emitting β -particles (and α -particles in the case of radon); that is, electrons that are difficult to detect due to their short-range path in matter, especially for ^3H (ref. 16). In this case, the liquid scintillation counting technique is the gold standard to measure radioactivity, but it requires a long and complex procedure to mix ^3H -labelled water with the scintillator¹⁷. This hinders *in situ* online measurements and produces liquid radioactive waste that must be carefully managed. Moreover, it cannot be applied to other gas radionuclides, which are highly insoluble. In this case the only option is to use gas meters that require large volumes and counting gases to increase the detection efficiency, resulting in very impractical instrumentation (see Supplementary Section 11).

A key solution to bypass these issues is to use solid porous scintillators: the adsorption and accumulation in the pores would concentrate the radionuclide, while simultaneously enhancing the probability of the scintillators interacting with the generated ionizing radiation, thus increasing the device sensitivity. Porous scintillators would allow the use of low detection volumes, thus enabling the realization of practical small instruments for *in situ* operation. Importantly,

the porous systems can also be cleaned from radioactive species and reused, thus enabling a sustainable technology that reduces risks and costs. Porous scintillators are therefore proposed as a new class of scintillating materials for the development of highly responsive and universal radioactive gas detectors based on time-coincidence techniques (Fig. 1a)¹⁸.

Scintillating metal–organic frameworks (MOFs) endowed with high porosity are excellent candidates. The controlled self-assembly of inorganic nodes and organic ligands produces tailored architectures with well-defined porosity for gas capture, separation and storage^{19–22}. Metal–organic frameworks have also been used as sorbents for the sequestration of noble gases²³ and, in some cases, ion radionuclides²⁴. Luminescent chromophores, included as ligands or guests, can be integrated to build emissive materials with unique photophysical and scintillating properties^{25–28}. However, despite recent MOF developments as colorimetric- and fluorescence-sensing platforms²⁹ and scintillators, their potential application for the detection of gas radioactivity has not yet been reported. Indeed, luminescent MOFs have been used to detect the presence of a few radioactive analytes in solution, but without any correlation to their radioactive properties³⁰.

Here we demonstrate the capability of porous hafnium-based MOFs containing the dicarboxy-9,10-diphenylanthracene (DPA) as a scintillating ligand for gas-radioactivity detection (Fig. 1). The crystalline MOF shows a highly accessible porosity suitable for hosting radioactive gases, which transfer their ionizing radiation to the framework, producing fast scintillation appropriate for time-coincidence detection techniques and a good fluorescence quantum yield of ~40%. The heavy hafnium improves the interaction with ionizing radiation and enables a good light intensity output, that is, one order of magnitude larger than a commercial scintillator. These excellent properties prompt us to test

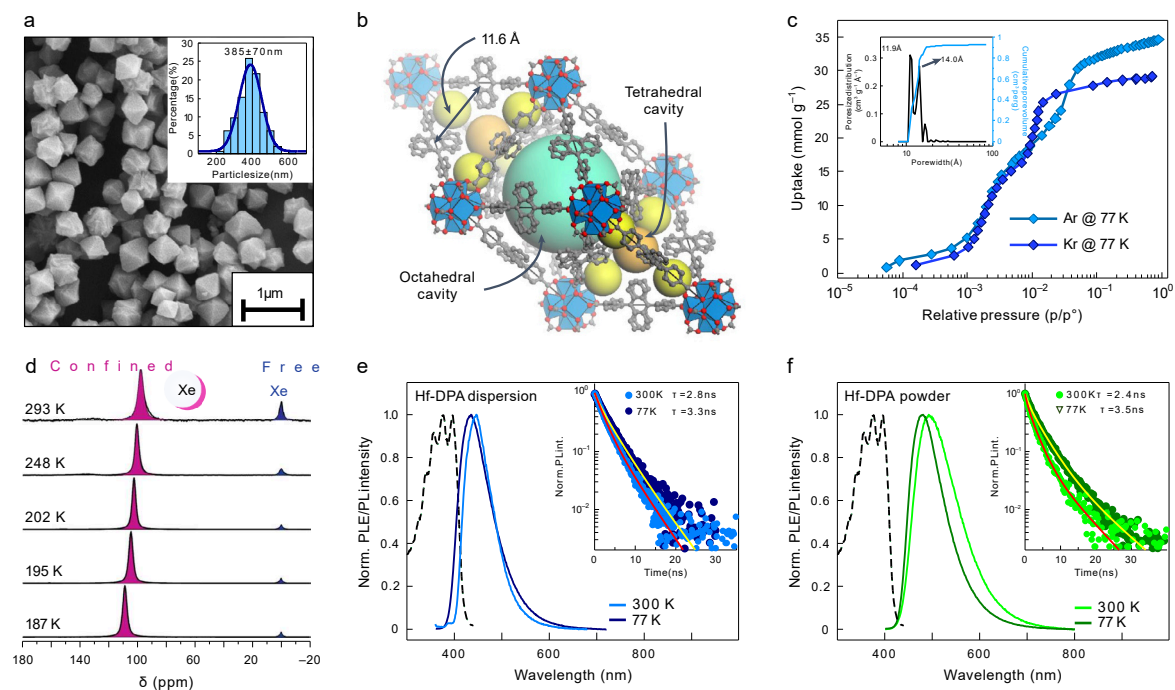


Fig. 2 | Structural, gas adsorption and photoluminescence properties of fluorescent porous MOFs. **a**, Scanning electron microscopy image of Hf-DPAMOFs. The inset depicts the MOF size distribution obtained by SEM image analysis. **b**, Crystal structure of Hf-DPA highlighting the octahedral and tetrahedral cavities. The triangular pore window and centre-to-centre distance between DPA molecules are highlighted. **c**, Argon (light blue) and krypton (dark blue) adsorption isotherms collected at 77 K. Inset: pore size distribution calculated from argon adsorption isotherm using the non-local density functional theory method. **d**, Hyperpolarized ^{129}Xe NMR spectra of Hf-DPA at

variable temperature. 2% xenon in a mixture with nitrogen and helium. **e**, **f**, The excitation photoluminescence (PLE, dashed line) and photoluminescence (PL) emission spectra of MOF crystals dispersed in THF ($5 \times 10^{-8} \text{ M}$) (**e**) or as bare powder (**f**). The photoluminescence was recorded at 300 K (solid line) and 77 K (dotted line). The excitation wavelength is 355 nm. The inset shows the photoluminescence intensity (PLint.) decay as a function of time recorded at the photoluminescence maximum emission wavelength under 340 nm pulsed excitation. The solid lines represent the fit of data with multi-exponential decay function that results in the average emission lifetime values reported.

the sorption and detection of ^{85}Kr , ^{222}Rn and ^3H radionuclides in a newly developed device that exploits the scintillating MOF powder as a gas harvester and concentrator (Fig. 1a). Metal–organic frameworks show an improved sensitivity with respect to reference powders currently tested for gas detection, as well as an excellent linear response down to an activity value of below 1 kBq m^{-3} for ^{85}Kr , thus outperforming commercial detectors in a compact, cost-effective and easy-to-handle architecture. The combination of porosity, good quantum yield and fast scintillation strongly support the possible use of scintillating porous MOFs as active components to fabricate technologically superior sensors for detecting natural and anthropogenic radioactive gases at ultralow concentrations.

Results

Gas adsorption and photoluminescence properties of Hf-based MOFs

Hafnium-based MOFs comprising luminescent DPA ligands (Hf-DPA) were obtained through solvothermal synthesis (see Methods and Supplementary Figs. 1–7)^{27,28}, which has been optimized to produce octahedral crystals with a cubic crystal structure 385 nm in diameter (Fig. 2a,b)—at which size the emission properties are best—in highly reproducible batches from few tens of milligrams up to ~200 mg (Supplementary Table 1 and Supplementary Figs. 8–20). Low-temperature gas adsorption isotherms demonstrate the microporous nature of Hf-DPA, and the adsorption of noble gases such as argon

and krypton (Fig. 2c and Supplementary Fig. 30). The argon and krypton adsorption isotherms were also measured at room temperature, demonstrating the gas diffusion inside the cavities under pressure and temperature conditions comparable to the operational scenario of radioactive gas detection (Supplementary Fig. 31). In this regard, we provided direct detection of noble gas diffusion into the pores of the Hf-DPA by hyperpolarized ^{129}Xe NMR experiments, even in competition with other gaseous species and under flow conditions (Fig. 2d, Methods, Supplementary Table 5 and Supplementary Fig. 28)^{28,31–35}. The detection of the signal at $\delta = 97.7 \text{ ppm}$ within 200 ms demonstrates the fast diffusion in the restricted pores.

Figure 2e shows the steady-state photoluminescence and excitation photoluminescence (PLE) spectra of Hf-DPA dispersed in tetrahydrofuran (see Methods). Under ultraviolet excitation, the dispersion exhibits a blue fluorescence peak at 450 nm, with a characteristic average decay time of 2.8 ns and a photoluminescence quantum yield of 0.41 ± 0.06 (Supplementary Section 7). The broad spectrum mirrors the presence of a distribution of local environments and quenching pathways for the emitting ligands^{25,26,35}. The excitation photoluminescence profile recorded at 450 nm matches the vibronic structure of DPA molecules³⁵. Low-temperature measurements show a blueshift of the photoluminescence maximum to 440 nm, ascribed to the band narrowing at cryogenic temperatures that reduces self-absorption, and an increased decay time of 3.3 ns, which indicates an emission yield increment to $0.41 \times \frac{3.3 \text{ ns}}{2.8 \text{ ns}} = 0.48$ (+18%).

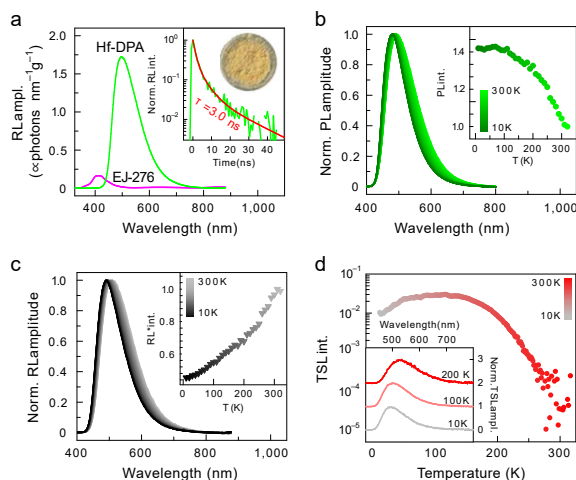


Fig. 3 | Scintillation properties of Hf-DPAMOF powder. **a**, Radioluminescence (RL) spectrum of Hf-MOFs and plastic EJ-276 scintillator powders under soft X-rays. The inset shows the scintillation pulse recorded for Hf-DPA with a picture of the MOF powder. The solid line represents the fit with a multi-exponential decay function. **b, c**, Normalized PL (**b**) and RL spectra (**c**) of Hf-DPA powder as a function of temperature. The inset in **c** depicts the radioluminescence intensity (RL*) normalized to the PL intensity variations shown in the inset of **b**, as a function of the temperature. **d**, Thermally stimulated luminescence intensity of Hf-DPA crystals powder as a function of the temperature, that is, the glow curve, obtained by integrating wavelength-resolved measurements in the whole emission region. The inset depicts representative TSL spectra recorded at 10 K, 100 K and 200 K.

This confirms the absence of substantial thermal quenching in Hf-DPA by intramolecular vibrational mechanisms^{25,26,35}. Figure 2f reports the photoluminescence properties of the Hf-DPA powder that will be used to detect the gas radionuclides. The emission at room temperature is red shifted to 490 nm due to the larger inner filter effect of self-absorption in the powder, whereas the PLE profile matches that of MOF in THF. The emission lifetime of 2.4 ns is basically unchanged. At 77 K, the emission maximum slightly blueshifted to 480 nm with a lifetime increment to 3.5 ns, confirming that the excited state electronic properties of the MOF powder are consistent with those of single crystals in diluted dispersion.

Scintillation properties of Hf-DPA

Figure 3a shows the steady-state scintillation (radioluminescence) spectrum of Hf-DPA powder compared with the commercial plastic scintillator EJ-276 (Methods) under soft X-rays. The MOF powder radioluminescence matches the photoluminescence profile (Fig. 2f). Notably, despite the Hf-DPA density of 0.6–0.7 g cm⁻³ being lower than the 1.1 g cm⁻³ of EJ-276, the scintillation generated by MOFs is more than one order of magnitude intense (Fig. 3a). This is ascribed to the presence of heavy hafnium ions (Z = 72) enhancing the interaction with ionizing radiation, which allows the scintillation efficiency of the Hf-DPA to double with respect to the parent zirconium-based MOF (Supplementary Fig. 32)²⁵. Hf-DPA produces a fast scintillation light pulse (Fig. 3a, inset) with a subnanosecond rise time and averaged decay time of 3 ns, which matches the photoluminescence decay dynamics. This confirms that the MOF emission properties are preserved under X-ray excitation.

The photoluminescence and radioluminescence of Hf-DPA have been monitored against temperature. Figure 3b shows the MOF powder normalized photoluminescence spectra recorded cooling

from 300 K to 10 K. At low temperature, the emission maximum wavelength shifts to 480 nm due to the mitigation of self-absorption by the band narrowing (Supplementary Table 7). The inset shows the photoluminescence intensity increasing by 40% at below 100 K, which corresponds to an increment of the quantum yield up to ~0.60. This enhancement is larger than that expected considering the corresponding increment of the emission lifetime (Fig. 3b, inset). These findings suggest that additional temperature-dependent ultrafast quenching pathways of diffusing charges or molecular excitons are involved in the partial emission quenching³⁶. The presence of traps is supported by the variable-temperature radioluminescence experiments. The radioluminescence spectrum changes in accordance with the photoluminescence (Fig. 3c and Supplementary Table 7). On the other hand, the radioluminescence intensity—corrected by the photoluminescence behaviour (inset of Fig. 3b) to point out the intrinsic luminescence dependence on the temperature—is progressively reduced by a factor of two at 10 K. This is a fingerprint of the presence of trapping sites, which compete with the recombination of diffusing free charges on emissive ligands. Thermal energy can free the trapped charges to be recovered for light generation reaching a thermal equilibrium (Supplementary Fig. 33)^{37,38}, but at low temperatures they are lost with a reduction of the emission intensity. The trap role in scintillation is investigated by wavelength-resolved thermally stimulated luminescence (TSL) measurements (Methods)^{39–41}. The smooth TSL glow curve—obtained by integrating the wavelength-resolved TSL spectra in the whole emission region—demonstrates the existence of a broad distribution of trap sites with different energy depths (Fig. 3d), which do not seriously affect the scintillation yield of the MOFs (Supplementary Fig. 34).

Radioactive gas detection with MOF powders

The capability of porous Hf-DPA to adsorb argon, krypton, xenon and radon at room temperature and concentrate their radioactive isotopes for detection was demonstrated by combined experimental and simulated approaches. Figure 4a shows the adsorption isotherms calculated by Grand Canonical Monte Carlo (GCMC) simulations (Methods and Supplementary Section 6). They successfully reproduce the experimental isotherms for argon and krypton, demonstrating the validity of the developed modelling as a predictive tool (Supplementary Figs. 35 and 36). The simulated adsorption at given pressures shows a correlation between the amount of gas adsorbed and the atomic mass, with a preference for the heavier radon. The smaller gas species such as krypton are more homogeneously distributed in all of the available space (Fig. 4b, left), whereas the larger radon atoms are preferably hosted in the smaller tetrahedral cavities of the MOF (Fig. 4b, right), due to the more effective interactions between the gas molecules and the framework walls. The gas–matrix interaction energies (Supplementary Figs. 37 and 38) give insight into the affinity and retention capability of the framework towards the exploring gases (Fig. 4c), and have relevance for selectivity and detection applications in air. The gas diffusion modelled in the presence of air at room temperature indicates that krypton atoms pervade the entire MOF crystals within tens of microseconds, demonstrating that noble gas radionuclides could be rapidly adsorbed into the pores in standard working conditions (Supplementary Figs. 39 and 40).

The Hf-DPA has been tested using a radioactive krypton isotope (⁸⁵Kr) in an acustom-made prototype device (Supplementary Fig. 41). The β-decay of ⁸⁵Kr produces electrons with a maximum emission energy of 687.1 keV and an average energy of 251.4 keV (ref. 42). The radionuclide can be mixed in air at different concentrations to tune the activity of the sample. The scintillation is detected by employing a time-coincidence measurement technique based on the simultaneous use of two photomultiplier tubes (PMTs) (Fig. 1b, see Methods, Supplementary Section 11 and Supplementary Fig. 41)¹⁸. The technique can be applied using different coincidence windows to maximize the device's sensitivity^{43–45}. Here we tested a coincidence window of 40 ns (as used with liquid scintillators) and 400 ns. Figure 4d

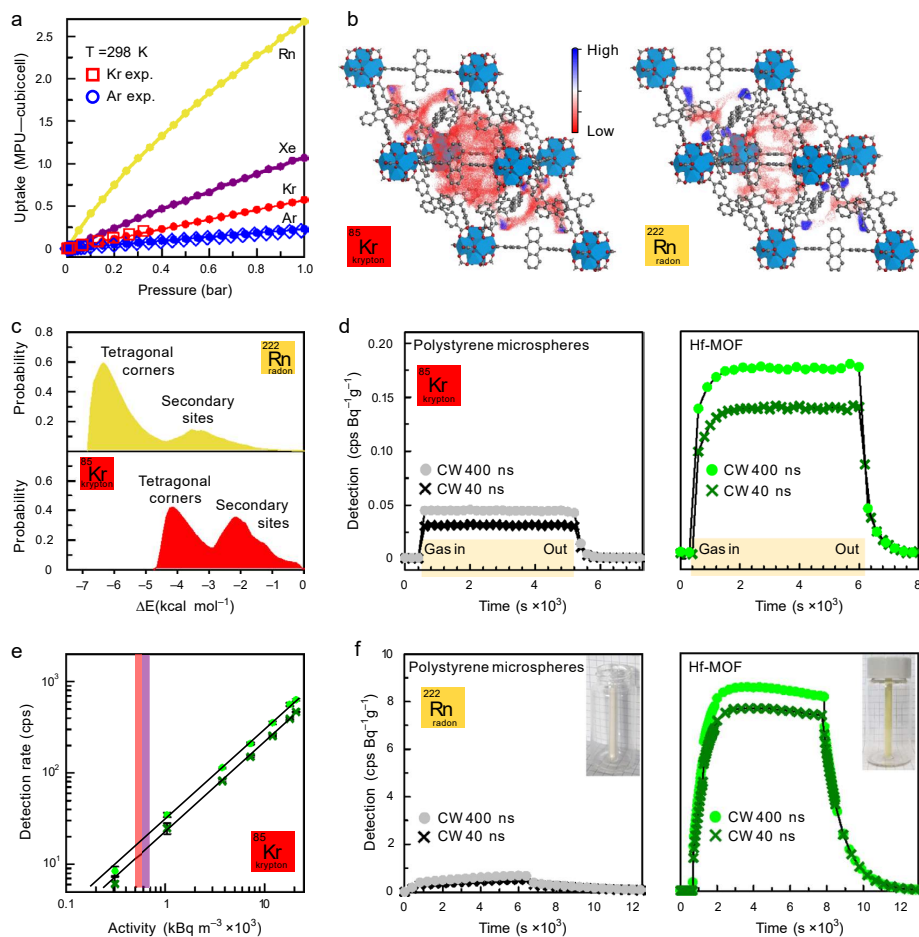


Fig. 4 | Radioactive gas adsorption and detection by porous scintillating Hf-DPA crystalline powder. **a**, Experimental argon and krypton isotherms and GCMC simulated adsorption isotherms of argon, krypton, xenon and radon for a cubic unit-cell of Hf-DPA ($32.79 \times 32.79 \times 32.79 \text{ \AA}^3$) at 298 K. The uptake is expressed in molecules per unit-cell (MPU). **b**, Gas density distributions calculated at room temperature at constant pressure of 0.5 mbar by GCMC adsorption simulations for krypton and radon. Blue and red colours indicate the highest and lowest gas density in the pores, respectively. **c**, Gas–matrix interaction energy distribution probability calculated at a constant pressure of 0.5 mbar and room temperature for krypton, xenon and radon. **d**, Double coincidence detection of ^{85}Kr by polystyrene microspheres powder and Hf-DPA

powder using two different coincidence windows (CWs) for detection (40 ns and 400 ns). The labels on the x-axis indicate when the radioactive gas has been injected into the detection device (gas in) and then washed out by a flux of clean air (gas out). cps, counts per second. **e**, Double coincidence detection rate of ^{85}Kr by the Hf-DPA powder as a function of the sample activity using different coincidence windows. The vertical lines mark the detection limit of a commercial device employed for detecting noble gas radionuclides (refs. 46, 47, red and violet line, respectively). The solid lines are the fit of data with linear functions. Error bars depict the residual values of the fit. **f**, Double coincidence detection of ^{222}Rn by polystyrene microspheres powder and Hf-DPA powder using different coincidence windows.

shows the results obtained for detecting ^{85}Kr using a standard scintillating powder—that is, dye-doped polystyrene microspheres with diameters of $175 \pm 75 \text{ \mu m}$ (ref. 46)—and Hf-DPA. The data highlights an improved behaviour for porous crystals. First, Hf-DPA generates a scintillation intensity ~ 4.6 - and 3.9 -times higher than microspheres for 40 ns and 400 ns coincidence windows, respectively. This demonstrates the efficiency of Hf-DPA as a scintillator despite its intrinsic lower density ($\sim 0.65 \text{ g cm}^{-3}$) compared with polystyrene (1.02 g cm^{-3}). Notably, gas detection can be performed with extremely high reproducibility ($\pm 1.3\%$ for 40 ns and $\pm 2.5\%$ for 400 ns coincidence windows, respectively). Moreover, the polystyrene emission peaked at 420 nm (Supplementary Fig. 31), where in the PMT detection efficiency (0.43)

is higher than for the 490 nm MOF emission (0.25)⁴⁷. A further improvement of the detection efficiency can therefore be envisaged by matching the scintillator and photodetector properties. Second, the expected increment using a longer coincidence window is less pronounced for Hf-DPA (around +25%) than for the polystyrene (around +50%). This indicates that MOFs work better as fast scintillators with a negligible slow emission contribution, giving a response closer to the ideal time-independent behaviour.

Third, the maximum scintillation signal is reached with slower kinetics for MOF than polystyrene. The signal rise time—calculated as the time employed to reach 90% of the maximum plateau—is $\sim 600 \text{ s}$ for Hf-DPA versus $\sim 100 \text{ s}$ for microspheres. A similar effect is observed

when removing the radionuclides from the sample by purging with clean air. The scintillation switches off in 800 s for MOFs, whereas it takes half of the time for the polystyrene microspheres. These findings suggest that, in addition to the fast, automatic filling of interparticle space within packed microspheres, the radionuclides are adsorbed within the MOF pores, in agreement with the experimental and simulated adsorption tests, thus promoting the interaction of the β -radiation with the scintillator that results in a better performance.

The versatility of our approach was demonstrated by testing Hf-DPA crystals as detectors with other radionuclides of interest, namely ^{222}Rn (with its four decay daughters at equilibrium, which are α - and high-energy β -emitters) and ^3H (Supplementary Figs. 41 and 42). Considering the larger capture of radon in the pores, the scintillation output should be improved with respect to krypton. Indeed, the detection efficiency is enhanced twentyfold with respect to polystyrene (Fig. 4f). Even for the elusive tritium, the MOF powder shows a better sensitivity in the detection counting rate—double that of polystyrene (Supplementary Fig. 43). This is a very important result as ^3H is one of the most difficult gases to detect, given the relatively low energy of the β -radiation emitted with an average value of 5.7 keV (ref. 42). Regarding krypton, we further tested the device as a function of the activity of the sample, as a progressively greater number of sensitive detectors is required. As shown in Fig. 4e, we detected ^{85}Kr from an initial activity of 21 kBq m^{-3} , down to 0.3 kBq m^{-3} —two orders of magnitude lower. The instrumental response is linear with the sample activity, suggesting the possibility of setting highly accurate calibrations of devices to detect ultralow activity levels. Notably, we successfully detected an activity below the minimum value declared for commercial ^{85}Kr detectors (vertical lines in Fig. 4e), in a device much smaller in size, with less volume of monitored gas and using one-order-of-magnitude shorter acquisition times (Methods and Supplementary Section 11), owing to the porous scintillator's ability to adsorb the gas^{48,49}. These remarkable results demonstrate that the prototype device presented here, although in its embryonic form, displays better sensitivity than state-of-the-art devices and highlights the technological advantage of potentially using compact, easy-to-handle and cheaper devices. Considering the good stability of Hf-DPA that does not imply any critical storage protocol (Supplementary Table 9 and Supplementary Fig. 45), this work strongly supports the development of radioactive gas detectors based on porous MOF crystals as scintillators that can overcome current technological limitations.

Discussion

In summary, we designed and fabricated specific scintillating porous MOF crystals to detect radioactive noble gases. Their good luminescence and scintillation properties—combined with their characteristic porosity—allowed us to realize a fully operative prototype detector. An intensive study on a broad range of critical β -emitting radioactive gases was performed, namely, the low-energy β -emitter ^3H , the high-energy β -emitter ^{85}Kr , and the β/α -emitter ^{222}Rn . The MOF crystals exhibited improved performance compared with commercial powder-like materials currently tested, and we found that ^{85}Kr can be detected with excellent sensitivity down to radioactivity values below the limit of commercial systems. The obtained results are therefore stimulating not only from the scientific point of view, as radionuclide detection using porous scintillators has been demonstrated here for the first time, but also from the technological perspective, hinting at a potential breakthrough by developing conceptually new optimized universal devices that allow detecting all the gas radionuclide species of interest. In this regard, it is worth pointing out that MOF powders cannot easily be used in the present form due to the practical problems of handling, especially from the perspective of industrial production. We are thus working on the realization of a hierarchical porous architecture in which porous MOFs are homogeneously distributed in a porous polymeric host endowed with

mesopores and macropores suitable for gas diffusion. In such a configuration, the MOFs will be employed to further concentrate and detect the radionuclides, thus realizing the first example of composite bulk porous scintillators for radioactive gas detection. Similarly, the instrumental design will be improved to get a more functional device. A possible evolution can be the use of a cylindrical shape container for the porous scintillator with aerosol filters as the entrance and exit face, in which the gas flow would circulate freely through the whole porous material, placed vertically between two photomultipliers. In such a configuration, the gas flow will be orthogonal to the detection line while diffusing through the whole scintillator, thus maximizing the radionuclide accumulation and the scintillation detection yield. The combination of easy-to-handle hierarchical porous scintillators and excellent detection properties of porous MOFs with an optimized instrumental design will provide a pivotal step forward in the fabrication of high-tech ultrasensitive and reusable detectors, especially for low-energy gas radionuclides such as tritium produced in nuclear plants.

Online content

Any methods, additional references, Nature Portfolio reporting summaries, source data, extended data, supplementary information, acknowledgements, peer review information; details of author contributions and competing interests; and statements of data and code availability are available at <https://doi.org/10.1038/s41566-023-01211-2>.

References

- Bollhöfer, A. et al. Half a century of Krypton-85 activity concentration measured in air over Central Europe: trends and relevance for dating young groundwater. *J. Environ. Radioact.* **205–206**, 7–16 (2019).
- Zeng, J. et al. Development of a well-type phoswich detector for low concentration krypton-85 measurement. *Nucl. Instrum. Methods Phys. Res. A* **1013**, 165634 (2021).
- Huang, Y.-J. et al. Automated separation and analysis of krypton-85 from low-volume gaseous effluent of nuclear power plant. *J. Radioanal. Nucl. Chem.* **323**, 213–222 (2020).
- Aoyama, M. Long-term behavior of ^{137}Cs and ^3H activities from TEPCO Fukushima NPP1 accident in the coastal region off Fukushima, Japan. *J. Radioanal. Nucl. Chem.* **316**, 1243–1252 (2018).
- Cao, Y. et al. Long-term investigation of environmental radioactivity levels and public health around the Qinshan Nuclear Power Plant, China. *Sci. Rep.* **12**, 4945 (2022).
- Schoeppner, M. & Glaser, A. Present and future potential of krypton-85 for the detection of clandestine reprocessing plants for treaty verification. *J. Environ. Radioact.* **162–163**, 300–309 (2016).
- Comprehensive Nuclear-Test-Ban Treaty Organization* (CTBTO, 2022); <https://www.ctbto.org/>
- Ćujić, M. et al. Radon-222: environmental behavior and impact to (human and non-human) biota. *Int. J. Biometeorol.* **65**, 69–83 (2021).
- Abd Elkader, M. M., Shinonaga, T. & Sherif, M. M. Radiological hazard assessments of radionuclides in building materials, soils and sands from the Gaza Strip and the north of Sinai Peninsula. *Sci. Rep.* **11**, 23251 (2021).
- Rudin, C. M., Brambilla, E., Faivre-Finn, C. & Sage, J. Small-cell lung cancer. *Nat. Rev. Dis. Primers* **7**, 3 (2021).
- Kissane, J., Neutze, J. A. & Singh, H. *Radiology Fundamentals: Introduction to Imaging and Technology* (Springer, 2020).
- Camfferman, F. A. et al. Diagnostic and predictive value of Doppler ultrasound for evaluation of the brain circulation in preterm infants: a systematic review. *Pediatr. Res.* **87**, 50–58 (2020).

13. Nichols, A. L. Status of the decay data for medical radionuclides: existing and potential diagnostic γ emitters, diagnostic β^- emitters and therapeutic radioisotopes. *Radiochim. Acta* **110**, 609–644 (2022).
14. *European Union EURATOM Directive 59/2013 'Basic Safety Standards'* (European Union, 2013); <https://eur-lex.europa.eu/eli/dir/2013/59/oj>
15. *Legislative Decree of 31 July 2020, no. 101 of Implementation of the Directive 2013/59/EURATOM of the European Council* (Ispettorato Nazionale per la Sicurezza Nucleare e la Radioprotezione, 2020); <https://www.isinucleare.it/en/radiation-protection-and-environmental-radioactivity>
16. Aprile, E., Bolotnikov, A. E., Bolozdynya, A. I. & Doke, T. *Noble Gas Detectors* (John Wiley and Sons, 2006).
17. Li, X. et al. Simultaneous determination of gross alpha/beta activities in water by liquid scintillation counting and its applications in the environmental monitoring. *Sci. Rep.* **12**, 8281 (2022).
18. Sabot, B., Dutsov, C., Cassette, P. & Mitev, K. Performance of portable TDCR systems developed at LNE-LNHB. *Nucl. Instrum. Methods Phys. Res. A* **1034**, 166721 (2022).
19. Eddaoudi, M., Li, H. & Yaghi, O. Highly porous and stable metal-organic frameworks: structure design and sorption properties. *J. Am. Chem. Soc.* **122**, 1391–1397 (2000).
20. Kitagawa, S., Kitaura, R. & Noro, S. I. Functional porous coordination polymers. *Angew. Chem. Int. Ed.* **43**, 2334–2375 (2004).
21. Férey, G. Hybrid porous solids: past, present, future. *Chem. Soc. Rev.* **37**, 191–214 (2008).
22. Mezenov, Y. A., Krasilin, A. A., Dzyuba, V. P., Nominé, A. & Milichko, V. A. Metal-organic frameworks in modern physics: highlights and perspectives. *Adv. Sci.* **6**, 1900506 (2019).
23. Elsaidi, S. K. et al. Radiation-resistant metal-organic framework enables efficient separation of krypton fission gas from spent nuclear fuel. *Nat. Commun.* **11**, 3103 (2020).
24. Jin, K., Lee, B. & Park, J. Metal-organic frameworks as a versatile platform for radionuclide management. *Coord. Chem. Rev.* **427**, 213473 (2021).
25. Lustig, W. P. et al. Metal-organic frameworks: functional luminescent and photonic materials for sensing applications. *Chem. Soc. Rev.* **46**, 3242–3285 (2017).
26. Doty, F., Bauer, C., Skulan, A., Grant, P. & Allendorf, M. Scintillating metal-organic frameworks: a new class of radiation detection materials. *Adv. Mater.* **21**, 95–101 (2009).
27. Perego, J. et al. Composite fast scintillators based on high-Z fluorescent metal-organic framework nanocrystals. *Nat. Photon.* **15**, 393–400 (2021).
28. Perego, J. et al. Highly luminescent scintillating hetero-ligand MOF nanocrystals with engineered Stokes shift for photonic applications. *Nat. Commun.* **13**, 3504 (2022).
29. Shi, W. et al. Advances of metal organic frameworks in analytical applications. *Mater. Today Adv.* **15**, 100273 (2022).
30. Yang, G. L., Jiang, X. L., Xu, H. & Zhao, B. Applications of MOFs as luminescent sensors for environmental pollutants. *Small* **17**, 2005327 (2021).
31. Sozzani, P. et al. Nanoporosity of an organo-clay shown by hyperpolarized xenon and 2D NMR spectroscopy. *Chem. Commun.* 1921–1923 (2006).
32. Comotti, A., Bracco, S., Valsesia, P., Ferretti, L. & Sozzani, P. 2D Multinuclear NMR, hyperpolarized xenon and gas storage in organosilica nanochannels with crystalline order in the walls. *J. Am. Chem. Soc.* **129**, 8566–8576 (2007).
33. Bassanetti, I. et al. Flexible porous molecular materials responsive to CO₂, CH₄ and Xestimuli. *J. Mater. Chem. A* **6**, 14231–14239 (2018).
34. Comotti, A. et al. Fluorinated porous organic frameworks for improved CO₂ and CH₄ capture. *Chem. Commun.* **55**, 8999–9002 (2019).
35. Monguzzi, A. et al. Highly fluorescent metal-organic-framework nanocomposites for photonic applications. *Nano Lett.* **18**, 528–534 (2018).
36. Ding, T. X., Olshansky, J. H., Leone, S. R. & Alivisatos, A. P. Efficiency of hole transfer from photoexcited quantum dots to covalently linked molecular species. *J. Am. Chem. Soc.* **137**, 2021–2029 (2015).
37. Korzhik, M., Tamulaitis, G. & Vasil'ev, A. N. *Physics of Fast Processes in Scintillators*. Vol. 262 (Springer, 2020).
38. Guerassimova, N., Garnier, N., Dujardin, C., Petrosyan, A. & Pedrini, C. X-ray excited charge transfer luminescence of ytterbium-containing aluminium garnets. *Chem. Phys. Lett.* **339**, 197–202 (2001).
39. McKeever, S. W. S. *Thermoluminescence of Solids* (Cambridge Univ. Press, Cambridge 1985).
40. Vedda, A. et al. Trap-center recombination processes by rare earth activators in YAlO₃ single crystal host. *Phys. Rev. B* **80**, 045113 (2009).
41. Buryi, M. et al. Trapping and recombination centers in cesium hafnium chloride single crystals: EPR and TSL study. *J. Phys. Chem. C* **123**, 19402–19411 (2019).
42. Bé, M.-M. et al. *Table of Radionuclides (Vol. 3 – A = 3 to 244)* (International Bureau of Weights and Measures, 2006).
43. Dutsov, C., Cassette, P., Mitev, K. & Sabot, B. In quest of the optimal coincidence resolving time in TDCR LSC. *Nucl. Instrum. Methods Phys. Res. A* **987**, 164846 (2021).
44. Dutsov, C., Cassette, P., Sabot, B. & Mitev, K. Evaluation of the accidental coincidence counting rates in TDCR counting. *Nucl. Instrum. Methods Phys. Res. A* **977**, 164292 (2020).
45. Dutsov, C., Sabot, B., Cassette, P. & Mitev, K. Significance of the corrections for accidental coincidences in liquid scintillation counting measurements. *J. Radioanal. Nucl. Chem.* **331**, 3303–3311 (2022).
46. Santiago, L. M., Bagán, H., Tarancón, A. & Garcia, J. F. Synthesis of plastic scintillation microspheres: evaluation of scintillators. *Nucl. Instrum. Methods Phys. Res. A* **698**, 106–116 (2013).
47. *R7600U PMT* (Hamamatsu Photonics, 2022).
48. *FHT59 ENoble Gas Monitor* (Thermo Scientific, 2022).
49. *XPR80* (Mirion Technologies, 2022).

Publisher's note Springer Nature remains neutral with regard to jurisdictional claims in published maps and institutional affiliations.

Open Access This article is licensed under a Creative Commons Attribution 4.0 International License, which permits use, sharing, adaptation, distribution and reproduction in any medium or format, as long as you give appropriate credit to the original author(s) and the source, provide a link to the Creative Commons license, and indicate if changes were made. The images or other third party material in this article are included in the article's Creative Commons license, unless indicated otherwise in a credit line to the material. If material is not included in the article's Creative Commons license and your intended use is not permitted by statutory regulation or exceeds the permitted use, you will need to obtain permission directly from the copyright holder. To view a copy of this license, visit <http://creativecommons.org/licenses/by/4.0/>.

© The Author(s) 2023

Methods

Synthesis of Hf-DPA crystals

Hf-DPA crystals were synthesized using modulated solvothermal condition. Briefly, 9,10-bis(4-carboxyphenyl)anthracene (209.0 mg; 0.5 mmol) and HfCl_4 (160.0 mg; 0.5 mmol) were added to a 100 ml pyrex bottle with cleavable teflon-lined cap. Dry DMF (50 ml) and 400 μl of formic acid were added and the bottle was closed and sonicated for 60 s to obtain a well-dispersed mixture. The mixture was heated at 120 °C for 22 h in a preheated oven. The glass bottle was then removed from the oven and cooled to room temperature. The yellowish solid was collected by filtration on a 0.2 μm PTFE membrane and washed with DMF (3 \times 100 ml) and then CHCl_3 (3 \times 100 ml). The powder was recovered and dried at 120 °C under high vacuum before further analysis. Yield: 178 mg (58%) (see the Supplementary Information for further details on ligand and MOF preparation).

Hf-DPA analysis and characterizations

Powder X-ray diffraction patterns were collected on a Rigaku Smartlab using Cu-K α radiation, whereas synchrotron radiation powder X-ray diffraction was performed at the ESRF ID22 beamline using a wavelength of 0.354 Å. The crystal structure was refined by the Rietveld method combined with molecular mechanics and plane-wave density functional theory calculations (Supplementary Section 5). The structure data are available at the Cambridge Crystallographic Data Centre repository, deposition no. 2218565. The composition of Hf-DPA was studied by means of NMR spectroscopy in solution, solid-state NMR spectroscopy, Fourier-transform infrared spectroscopy, thermogravimetric analysis, scanning electron microscopy and EDS analysis. The gas sorption properties were investigated by collecting nitrogen, argon and krypton adsorption isotherms at 77 K up to saturation pressure and argon and krypton at 298 K; hyperpolarized ^{129}Xe NMR experiments were performed by a home-built apparatus with a continuous-flow delivery of hyperpolarized xenon gas with a Bruker Avance 300 spectrometer operating at a Larmor Frequency of 83.02 MHz for ^{129}Xe . The xenon and radon adsorption isotherms at 298 K were performed by GCMC.

Photoluminescence studies

Absorption spectra were recorded using a Cary Lambda 900 spectrophotometer at normal incidence with Suprasil quartz cuvettes with a 0.1 cm optical path length and an integrating sphere to eliminate scattering effects. Steady-state photoluminescence spectra were acquired using a Varian Eclipse fluorimeter (bandwidth 1 nm) using quartz cuvettes of 0.1 cm optical path length. Time-resolved photoluminescence spectra of the MOF dispersions were recorded by monitoring the emission decay of the samples at 435 nm. The MOFs were excited with a pulsed light-emitting diode at 340 nm (3.65 eV, pulse width 80 ps; EP-LED340, Edinburgh Instruments). The MOFs were excited with a pulsed laser at 405 nm (3.06 eV, pulse width 90 ps; EPL-405, Edinburgh Instruments) to avoid direct excitation of the host polymer matrix. Photoluminescence decay times were measured at the maximum of the emission spectrum. Relative and absolute photoluminescence quantum yields were measured with different methods as described in the Supplementary Section 7. For experiments at cryogenic temperatures, the samples were excited by a frequency tripled pulsed Nd:YAG laser source at 3.49 eV (355 nm) operated at 10 kHz; the emitted light was collected using a custom apparatus featuring a liquid nitrogen-cooled, back-illuminated, and ultraviolet-enhanced charge-coupled device detector (Jobin-Yvon Symphony II) coupled to a monochromator (Jobin-Yvon Triax 180) equipped with a 100 lines per millimeter grating.

Radioluminescence and scintillation studies

The samples were excited by unfiltered X-ray irradiation using a Philips PW2274 X-ray tube, with tungsten target, equipped with a beryllium window and operated at 20 kV. At this operating voltage, X-rays are

produced by the *Bremsstrahlung* mechanism, superimposed to the L and M transition lines of tungsten due to the impact of electrons generated through anthermionic effect and accelerated onto the tungsten target. Cryogenic radioluminescence measurements are performed in the 10–370 K interval. Radioluminescence has been recorded on powder samples of 1 mm thickness in an aluminium sample holder. For comparison the radioluminescence spectra have been normalized by the mass of the investigated powder.

Scintillation has been recorded under pulsed X-rays with energies up to 25 keV generated with a repetition rate of 1 MHz by a picosecond diode laser at 405 nm (Delta diode from Horiba) focused on an X-ray tube (model N5084 from Hamamatsu). The resulting photons were collected by a Kymer spectrograph (ANDOR) and detected by a hybrid PMT 140-C from Becker and Hickl GmbH. For decay-time measurements, the photons were histogrammed using a PicoHarp 300 time-correlated single-photon counting (32 ps time per bin) and for the time-resolved spectra a MCS6A multiple-channel time analyzer was used (800 ps time per bin). Subnanosecond scintillation emission kinetics of the samples were measured with a time-correlated single-photon counting set-up.

Thermally stimulated luminescence measurements

Wavelength-resolved TSL at cryogenic temperatures is performed by using the same detection system as for radioluminescence measurements. Cryogenic TSL measurements are performed in the 10–320 K interval, with a linear heating rate of 0.1 K s $^{-1}$, after X-ray irradiation up to around 10 Gy. The dose values for X-ray irradiations were calibrated with an ionization chamber in air.

Radioactive gas detection experiments

The experiments are performed using a unique gas bench developed at the CEA, Paris-Saclay, and by allowing the production of radioactive gas atmospheres using high activity standards⁵⁰. Different sampling and dilution steps allow for precise control of the injected activity, and precise knowledge of the volumetric activity of each gas: at best, the relative standard uncertainty on the activity concentration is 0.4%, 0.6% and 0.8% for ^{222}Rn , ^{85}Kr and ^3H , respectively (Supplementary Table 9). For each experiment, the same type of three-step sequence is performed. First, the measurement of the blank, by circulating clean air without additional radioactivity. Second, the measurement of scintillation by circulating the radioactive gas sample into the vial (4 mm diameter and 50 mm height, 0.1086 g for Hf-DPA and 0.3640 g for polystyrene microspheres, activity 10 kBq). Third, circulation of clean air into the device to remove the radioactive gas. The light photons produced by scintillation are measured using a metrological device developed to exploit the triple-to-double coincidence ratio (Supplementary Fig. 41)¹⁸, with a specific connection cap adapted to the radioactive gas flow in the scintillator.

Data availability

The data that support the plots within this paper and other findings of this study are available from the corresponding author upon reasonable request, at the public repository of the project SPARTEFET Open Project (<https://www.sparte-project.eu/>). The Hf-DPA structure's Cambridge Crystallographic Data Centre deposition no. is 2218565. No custom code has been developed for computational modeling and simulations.

References

50. Sabot, B., Rodrigues, M. & Pierre, S. Experimental facility for the production of reference atmosphere of radioactive gases (Rn, Xe, Kr, and H isotopes). *Appl. Radiat. Isot.* **155**, 108934 (2020).

Acknowledgements

We acknowledge support from the European Community through the grant no. 899293, HORIZON 2020—SPARTEFET OPEN. Financial

support from the Italian Ministry of University (MUR) through grant no. PRIN2020—SHERPAno.H45F2100343000, and from Lombardy Region through the 'Enhancing photosynthesis' award, no. H45F21002830007. We thank the ESRF synchrotron facility in Grenoble (France) for access to the ID22 beamline (project no. HC-4781).

Author contributions

M.O., F.C., A.V. and A.M. conceived and performed the photoluminescence, radioluminescence experiments. J.P., C.X.B., S.P., C.Da. and S.B.A.C. designed, synthesized and characterized the MOFs. C.Du. managed the scintillation experiments. B.S., S.P. and P.M. designed, performed and analyzed the gas detection experiments. C.Du., B.S., A.C. and AM. conceived the project and wrote the paper. A.C. and AM. wrote the paper. All of the authors agreed to all of the content of the manuscript, the author list and its order, and the author contribution statements. Any changes to the author list after submission will be subject to approval by all authors.

Competing interests

The authors declare no competing interests.

Additional information

Supplementary information The online version contains supplementary material available at <https://doi.org/10.1038/s41566-023-01211-2>.

Correspondence and requests for materials should be addressed to Anna Vedda, Angiolina Comotti or Angelo Monguzzi.

Peer review information *Nature Photonics* thanks Wei Chen, Wolfgang Heiss and the other, anonymous, reviewer(s) for their contribution to the peer review of this work.

Reprints and permissions information is available at www.nature.com/reprints.

This page was intentionally left blank.

This page was intentionally left blank.

This page was intentionally left blank.

This page was intentionally left blank.